2017

Plasmonic and Near-Field Effects in Graphene Nanostructures

Dan You
Lehigh University

Plasmonic and Near-Field Effects in Graphene Nanostructures

by

Dan You

A Dissertation
Presented to the Graduate Committee
of Lehigh University
in Candidacy for the Degree of
Doctor of Philosophy
in
Physics

Lehigh University
January 22, 2017

Approved and recommended for acceptance as a dissertation in partial fulfillment of the requirements for the degree of Doctor of Philosophy.

Dan You
Plasmonic and Near-Field Effects in Graphene Nanostructures

Date

Slava V. Rotkin, Dissertation Director, Chair

Accepted Date

Committee Members

James D. Gunton

A. Peet Hickman

Michael J. Stavola

Xiaoji G. Xu

ACKNOWLEDGMENTS

I would like to express my deepest gratitude to my supervisor, Dr. Slava V. Rotkin for his guidance, support, and patience. His love and enthusiasm for science inspired me and will be inspiring many more students. Thanks for being a good adviser to me. This work would not be possible without him. I believe that I have learned a lot from him.

I am grateful for my committee members: Dr. James D. Gunton, Dr. Peet A. Hickman, Dr. Michael J. Stavola, Dr. Xiaoji G. Xu, for their knowledgeable insights on my thesis work and kind guidance.

I would lie to give my appreciation to my group members: Dr. Tetyana Ignatova, Dr. Benjamin Sofka, Dr. Massooma Pirbhai, Michael Blades and Wenxin Huang. Thanks for their helpful comments and discussions, and for being such amazing teammates and friends. Especially thank Ben and Michael for proofreading my thesis. I would like to thank all my friends in the US who have been very helpful in numerous ways and always a great boost and fun in my life.

I would like to say a heartfelt thank to my parents and my parents in Law for their constant support and endless love. I extremely appreciate your care and encouragements.

Last, but not the least, I would like to express my endless thanks to my husband for always believing in me and listening to all my complaints and working so hard for us. Thank you.

Contents

List of Tables

List of Figures

Abstract

We theoretically study the heat transfer mechanism between graphene and a polar substrate. We develop a thermodynamic theory of heat transfer between graphene and a SiC substrate based on the master equation method. In the presence of strong coupling between surface plasmon- and phonon-polaritons in graphene and the substrate, a quantum master equation can be used to describe the relaxation dynamics of hybrid modes of our system.

We explore quantization of surface plasmons in a graphene nanodisk structure and derive the response of the graphene nanodisk to an external field. Discrete frequencies and corresponding wavefunctions of localized plasmons in the graphene nanodisk are due to space quantization. The specific case of a dipole excitation is studied to represent the near-field experiments. The approximately spherical tip of a near-field microscope is modeled as a point-dipole with an known orientation (polarization). Due to the finite(non-zero) width of plasmon resonances in the disk, the response function may allow the near-field patterns with combined angular symmetry, obtained as a composition of modes with different angular momentum and radial quantum numbers.

Furthermore, we investigate the surface plasmon hybridization between the quantized modes in a disk and an infinite monolayer of graphene. We also consider new mechanism for mixing of the angular plasmon modes. In the case of mismatched lattice between the disk and the monolayer the angular momentum is not conserved. We introduce a scalar perturbation with a spatial pattern which resembles one of a moire pattern in graphene bilayer. Such a perturbation that varies smoothly within the graphene nanodisk and has 3-fold symmetry modulates the conductivity of graphene. We observe coupling between plasmon modes with different angular quantum number which occurs due to perturbation. The shape of the hybrid wavefunction is analyzed in terms of broken axial symmetry of the system. Response function of the hybrid system is derived and near-field maps were computed.

Chapter 1

Introduction

1.1 Graphene Plasmonics

Graphene, a two dimensional crystal, is made of a single layer of carbon atoms. Graphene has attracted a lot of interest due to its unique properties applicable in electronics, optics and thermal management[8, 9, 10]. Graphene plasmonics studies collective surface charge oscillations in a single or multiple layers of graphene accompanied by strong surface an EM field. Due to the extraodianry properties of graphene materials, such as high mobility and tunabilty of surface impedance [11, 12], plasmonic application were porposed. Indeed, plasmons in graphene at infrared frequencies have a high confinement factor and lower propagation loss [13, 14]. To better understand the fundamental properties of plasmons in graphene, we begin with introducing the electronic structure of graphene.

1.1.1 Graphene Band Structure

Graphene is a two dimensional honeycomb lattice of carbon atoms. However, the honeycomb lattice is not a Bravais lattice because the two neighboring sites are not equivalent. In Fig.1.1, the honeycomb lattice is shown to be formed in a triangular Bravais lattice with a two inequivalent atom basis (A and B). The lattice vectors

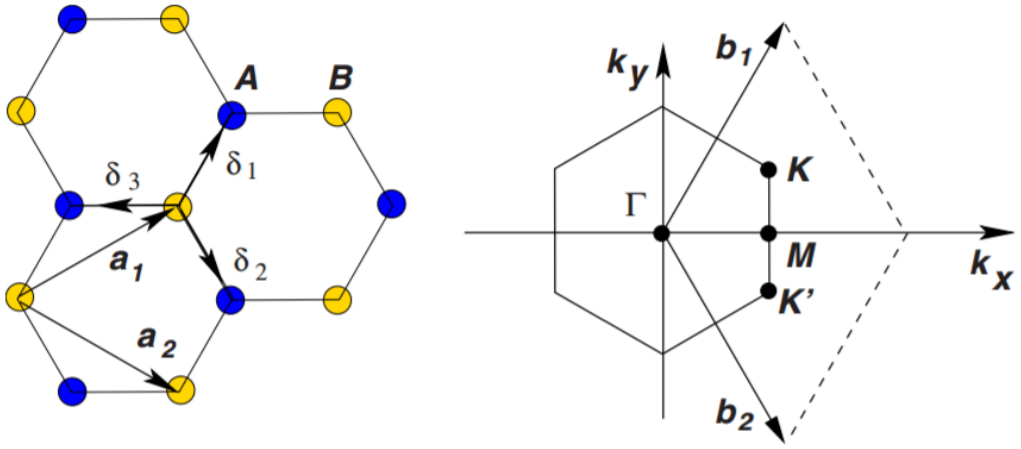

Figure 1.1: Honeycomb lattice (Left) and corresponding Brillouin zone (Right) of graphene. The vector a_1 and a_2 are the basis set vectors of the triangular Bravias lattice and vectors δ_1, δ_2, δ_3 are the nearest-neighbor vectors. Right panel represents the first BZ with its center (Γ) and the two inequivalent corners (K and K'). b_1 and b_2 are reciprocal lattice vectors [3].

are [3]

$$\mathbf{a}_1 = \frac{a_0}{2}(3, \sqrt{3}), \qquad \mathbf{a}_2 = \frac{a_0}{2}(3, -\sqrt{3}). \tag{1.1}$$

The lattice constant $a_0 = 0.142$ nm. The first Brillouin zone (BZ), which represent a set of inequivalent points in the reciprocal space is also shown is Fig.1.1. The reciprocal lattice vectors are

$$\mathbf{b}_1 = \frac{2\pi}{3a_0}(1, \sqrt{3}), \qquad \mathbf{b}_2 = \frac{2\pi}{3a_0}(1, -\sqrt{3}). \tag{1.2}$$

The six corners of the first BZ consist of two inequivalent points K and K', which can be called Dirac points. The other four corner points can be obtained through a translation of the reciprocal lattice vectors. Therefore, we just need to consider Dirac points K and K', that can describe graphene in momentum space.

Graphene presents sp^2 hybridization. Three sp^2 hybridized orbitals are oriented

in the x-y plane and form a triangular structure with an angle of 120° between carbon atoms. Therefore, carbon atoms in graphene are strongly bonded by means of covalent σ bonds. The remaining $2p_z$ orbital is oriented perpendicularly to the x-y plane and forms the π electron subsystem. The tight-binding approach is sufficient to describe the band structure, and the energy bands have the form

$$E_{\pm} = \pm t\sqrt{3 + f(\mathbf{k})}, \tag{1.3}$$

where $t \approx 2.8eV$ is the nearest-neighbor hopping energy.

$$f(\mathbf{k}) = 2\cos(\sqrt{3}k_y a) + 4\cos(\frac{\sqrt{3}}{2}k_y a)\cos(\frac{3}{2}k_x a) \tag{1.4}$$

The energy dispersion Eq.1.3 is plotted in Fig.1.2. We can see that the energy dispersion consists of two bands: the lower energy band, which is the valence bands and is completely filled with electrons, and an upper energy band, which is the conduction band and is completely empty at zero temperature. The two bands are degenerate at the Dirac point. Also, in the enlarged view of Fig.1.2, we can see that the dispersion relation close to the Dirac point can be approximately regarded as a linear at small wave vectors. This linear dispersion can be described as,

$$E_{\pm}(\mathbf{q}) \approx \pm v_f|\mathbf{q}| \tag{1.5}$$

where q is the wavevector and v_f is the Fermi velocity, with a value $v_f \approx 10^6$ m/s. This linear dispersion suggests that electrons and holes in graphene act as massless relativistic Dirac fermions. Also, due to conduction and valence bands intersecting at the Dirac point, there is no energy gap. Graphene is thus a zero band-gap semiconductor [15] with a linear energy dispersion at long-wavelength limit. One can expect that quasiparticles in graphene behave differently from those in conventional metals and semiconductors [16].

1.1.2 Surface Plasmon in Graphene

Graphene is a zero band-gap semiconductor: the gap between valance band and conduction band closes at the Dirac points, which also indicates that the Fermi

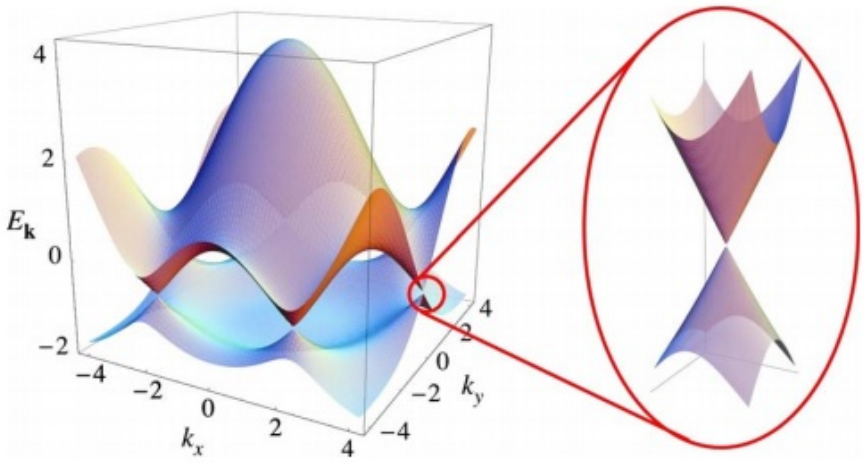

Figure 1.2: Electronic dispersion in the honeycomb lattice obtained with the tight-binding approch, for $t = 2.7eV$,$t' = -0.2t$,[3].

level is at zero ($E_F = 0$) for undoped graphene. Thus for undoped graphene, only interband electron-hole transitions are allowed. When extra electrons or holes are added to graphene through electrical gating or chemical doping (n/p doped graphene)[18, 19, 20], the Fermi energy E_F shift away from the Dirac point, and is given as $E_F = \hbar v_f \sqrt{\pi n}$, where n is the charge density of those extra electrons or holes. Due to the shift of the Fermi level, the intraband electron hole transition is allowed. Therefore, the optical conductivity of graphene should contain two parts in general: due to interband transitions and intraband transitions.

The conducitivity of graphene can be derived from RPA (Random Phase Approxmation)[17],

$$\sigma_{intra}(\omega) = \frac{e^2\omega}{i\pi\hbar}\int_0^\infty d\epsilon \left(\frac{df(\epsilon)}{d\epsilon} - \frac{df(-\epsilon)}{d\epsilon}\right) = \frac{2ie^2k_BT}{\pi\hbar(\omega + i\tau^{-1})} ln[2\cosh(E_F/2T)]), \tag{1.6}$$

$$\sigma_{inter}(\omega) = \frac{ie^2\omega}{\pi\hbar}\int_0^\infty d\epsilon \frac{f(-\epsilon) - f(\epsilon)}{(\omega + i\tau^{-1})^2 - 4(\epsilon/\hbar)^2} \tag{1.7}$$

Where $f(\epsilon) = \frac{1}{e^{(\epsilon - E_F)/k_BT}+1}$ is the Fermi distribution function, and τ^{-1} is the electrons relaxation rate related to the damping of electron in graphene. In the low temperature limit, $k_BT \ll E_F$, the intraband terms of the graphene conductivity

Mode	$Im[\sigma]$	$Contribution$	$Frequency$	$Damping$
TM	> 0	$Intraband$	$THZ, far-infrared$	No
TE	< 0	$Interband$	$Far-, near-infrared$	$Finite$

Table 1.1: TM and TE surface plasmon in graphene [1].

have the Drude-like form,

$$\sigma_{intra}(\omega) = \frac{ie^2\omega E_F}{\pi\hbar(\omega + i\tau^{-1})} \tag{1.8}$$

The interband contribution in the same limit also can be approximated as

$$\sigma_{inter}(\omega) = \frac{e^2}{4\hbar}\left[\theta(\omega - 2E_F) - \frac{i}{\pi}ln|\frac{\omega + 2E_F}{\omega - 2E_F}|\right] \tag{1.9}$$

where θ is the step function. Grahene conductivity is a complex valued function of frequency. The real part of the conductivity shows a step at $\omega = 2E_F$, thus, for $\omega > 2E_F$, the optical loss is dominated by the interband transitions. The imaginary part of the conductivity determines which kind of surface polariton modes can be supported. If the imaginary part is negative, then TE modes are supported in graphene. Otherwise TM modes are supported. The properties of graphene for TM and TE plasmon modes are summarized in Table.1.1 [1]. Fig.1.3 shows that in doped graphene there is a region where surface plasmons are not subject to Landau damping due to energy-momentum conservation. The typical frequency of surface plasmons falls in the THZ and far-infrared region. We consider TM modes in graphene surrounded by a dielectric medium with permittivity ε_1 and ε_2. From Maxwell's equations,

$$\nabla \cdot \mathbf{D}(\mathbf{r}) = \rho(r) \tag{1.10}$$

$$\nabla \times \mathbf{H}(\mathbf{r}) - \frac{\partial \mathbf{D}(r)}{\partial t} = \mathbf{J}(\mathbf{r}) \tag{1.11}$$

$$\nabla \times \mathbf{E}(\mathbf{r}) + \frac{\partial \mathbf{B}(r)}{\partial t} = 0 \tag{1.12}$$

$$\nabla \cdot \mathbf{B} = 0 \tag{1.13}$$

and boundary conditons

$$E_x(z=0^+) - E_x(z=0^-) = 0 \tag{1.14}$$

$$H_y(z=0^+) - H_y(z=0^-) = \sigma E_x(z=0) \tag{1.15}$$

the dispersion relation for graphene plasmons can be analytically derived

$$\frac{\varepsilon_1}{\sqrt{q^2 - \frac{\varepsilon_1\omega^2}{c^2}}} + \frac{\varepsilon_2}{\sqrt{q^2 - \frac{\varepsilon_2\omega^2}{c^2}}} + \frac{i\sigma}{\omega} = 0 \tag{1.16}$$

The dispersion of surface plasmons is shown in Fig.1.3(b). We can see that for $k_{//} < k_f$ and $\omega < 2E_F$, surface plasmons have zero damping. However, outside of this region, surface plasmon dispersion curve enters into an interband excitation region where plasmon can decay into electron-hole pairs. In the non-retarded limit, where we assume $q >> \frac{\omega}{c}$, above equation yields,

$$q \approx i\frac{(\varepsilon_1 + \varepsilon_2)\omega}{\sigma}. \tag{1.17}$$

Assuming graphene is described by the Drude conductivity model, we insert Eq.1.8 into Eq.1.17. In the infinite lifetime approximation, we get,

$$\omega = \sqrt{\frac{e^2 Ef}{(\epsilon_1 + \epsilon_2)\pi\hbar^2}q}. \tag{1.18}$$

Eq.1.18 indicates that the surface plasmon frequency can be controlled by changing the charge concentration through doping or gating, as we mentiond before, due to $E_F = \hbar v_f\sqrt{\pi n}$. The tunabilty of surface plasmon is the one of most important advantages of graphene for plasmonics. It opens up the possibility to create tunable devices of various kinds, for instance tunable optical filters and modulators [21, 22].

1.2 Graphene Stacking

Graphite consists of stacked graphene layers. For bilayer graphene, the most stable stacking of the two layers is **AB** or **AA** stacking. Graphite usually has a variety of

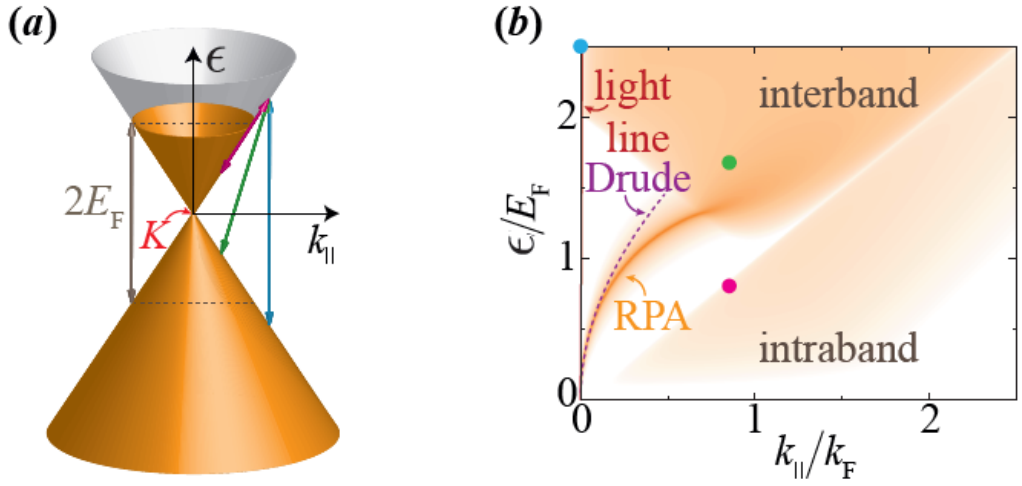

Figure 1.3: The Dispersion relation of plasmons in graphene. **(a)** Two electron-hole transition : Interband transistion (green and blue arrow) and Intraband transition (magenta arrow). **(b)** Density plot of dispersion relation for suspended graphene.[3]

defects which effect stacking order [23]. It has been shown that a graphene bilayer with a relatively small rotation between the layers can result in the formation of superlattices known as moiré superlattices [24], as shown in Fig.1.4. The term moiré superlattice is used to describe the beating of any short range perodic pattern to create a long range quasi-periodic pattern [25].

Suppose that the initial stacking between two layers is **AB** stacking, the moiré pattern can be seen when rotating one layer about a fixed site. The relative angle can be derived [24]

$$cos(\phi_i) = \frac{3i^2 + 3i + 1/2}{3i^2 + 3i + 1} \tag{1.19}$$

where $i = 0, 1, 2 \cdots$ ($i = 0$ corresponds to an **AA** stacked bilayer). The superlattice basis vectors are

$$\begin{aligned} \mathbf{t}_1 &= i\mathbf{a}_1 + (i+1)\mathbf{a}_2 \\ \mathbf{t}_2 &= -(i+1)\mathbf{a}_1 + (2i+1)\mathbf{a}_2 \end{aligned} \tag{1.20}$$

where $\mathbf{a}_1 = (\frac{1}{2}, \frac{\sqrt{3}}{2})a_0$,$\mathbf{a}_2 = (-\frac{1}{2}, \frac{\sqrt{3}}{2})a_0$ are the Bravias lattice basis vectors and

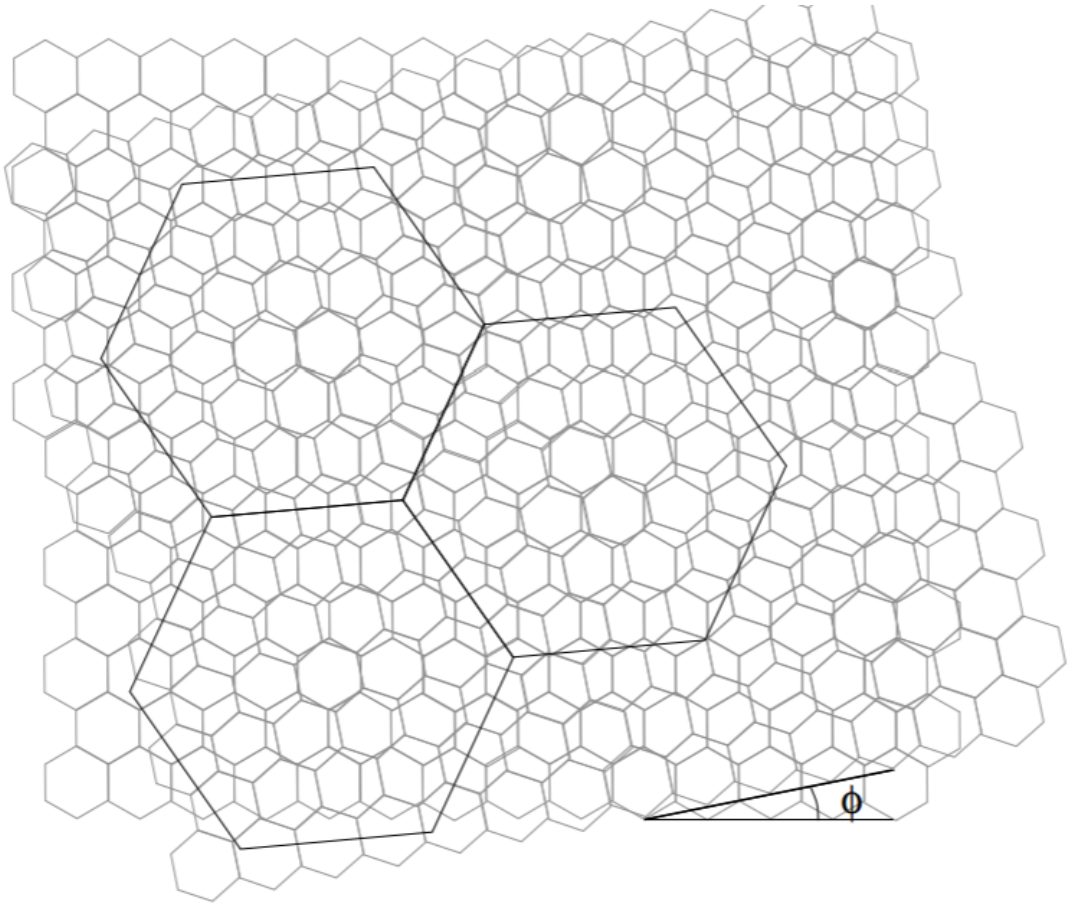

Figure 1.4: Moiré patterns obtained by stacking two honeycomb lattices with a relative angle ϕ. The hexagonal superlattice is produced.

$a_0 \approx 2.46\mathring{A}$ is the lattice constant. The lattice constant of the superlattice is

$$LC = |\mathbf{t}_1| = |\mathbf{t}_2| = \sqrt{3i^2 + 3i + 1}a_0 \tag{1.21}$$

The reciprocal lattice vectors are

$$\mathbf{G}_1 = \frac{4\pi}{3(3i^2 + 3i + 1)}[(3i + 1)\mathbf{a}_1 + \mathbf{a}_2] \tag{1.22}$$

$$\mathbf{G}_2 = \frac{4\pi}{3(3i^2 + 3i + 1)}[-(3i + 2)\mathbf{a}_1 + (3i + 1)\mathbf{a}_2] \tag{1.23}$$

1.3 Basics of Phonon Thermal Conductivity in Graphene

Thermal properties, such as thermal conductivity and interfacial thermal resistance of the electric material, are crucial properties of a material to control heat dissipation in device. The ability of a material to conduct heat is essential in the potential electronic applications. Heat is carried by both phonons and electrons. Since graphene lattice is composed of a light element, where the in-plane bonding is very strong, graphene exhibits a very large sound velocity. Therefore, thermal conductance is dominated by phonons in graphenes unlike a normal metal.

To understand the thermal properties of graphene, we first inspect the phonon modes of graphene. Graphene has three acoustic and three optical phonon modes [26]. In Fig.1.5, we can see longitudinal and transverse acoustic modes (LA and TA) that have a linear dispersion relations near the center of Brillouin zone (Γ point). ZA modes stand for out of plane vibrating acoustic modes (also known as flexural modes) that show q^2 dispersion near the Γ point, which is a characteristic feature of the phonon dispersion in layered crystals also observed experimentally[4]. The acoustic phonons serve as the main heat carriers in graphene [27].

Thermal conductivity describes the ability of a material to conduct heat. Higher thermal conductivity plays a significant role in the cooling of electronic devices. Thermal conductivity is introduced through Fourier's Law [5]:

$$Q = -\kappa \nabla T. \tag{1.24}$$

where Q is the heat flux, ∇T is the temperature gradient, κ is the thermal conductivity, which is a function of temperature. The sign in this relationship is negative, indicating that heat flows from high to low temperature. Graphene has a very high thermal conductivity, which can exceed $2000 W/mK$ at room temperature [28][6].Fig.1.6**b**[5] shows that the thermal conductivity for suspened graphene at room temperature has the highest value among all the materials, about $2000 - 4000 W/mK$. On the other hand, the thermal conductivity across plane direction

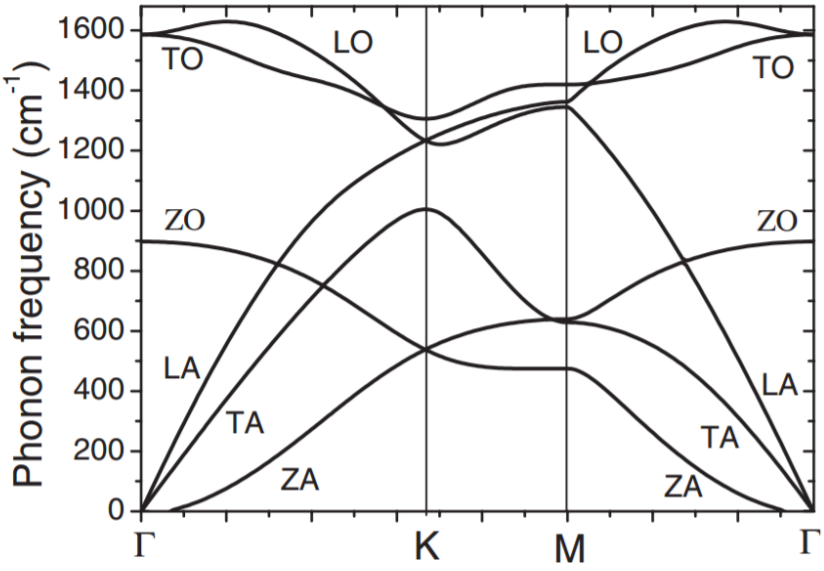

Figure 1.5: Phonon dispersions for monolayer graphene [4].

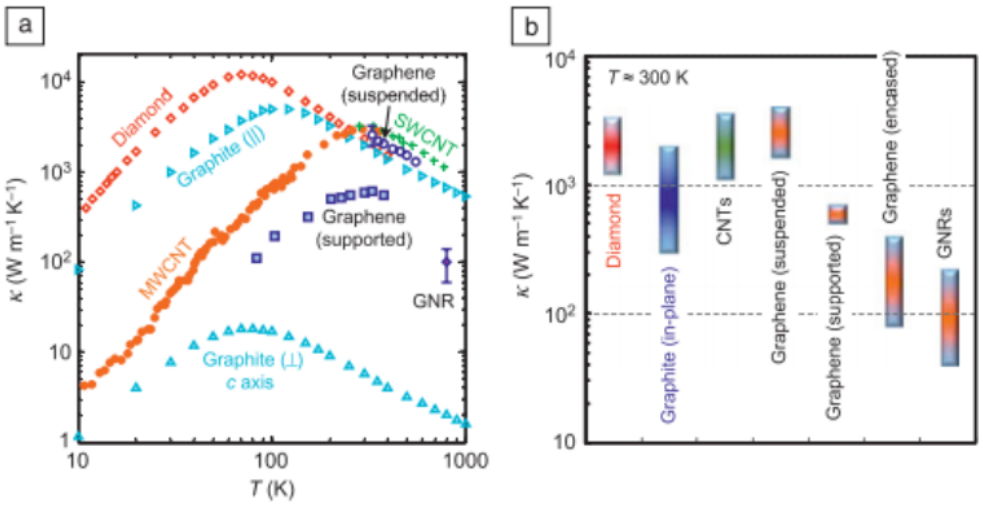

Figure 1.6: **(a)** Thermal conducivity as a function of temperature. **(b)** Room-temperature ranges of thermal conductivity.[5]

(along c axis) of graphene is strongly limited (see Fig.1.6**a**) by weak interlayer interaction (van der waals interaction).

1.4 General Theory of Linear Response to an External Perturbation

In order to understand absorption and reflectance spectrum, we have to evaluate the response of the material to an external perturbation. If this perturbation is weak as usually in spectroscopic experiments, the induced change in the charge density can be described within perturbation theory as linearly dependent on the applied perturbation. In this section, we provide a general background of the linear response to a weak external perturbation.

Follow the derivation of Fetter and Walecka [29], we suppose that we have a system described by a Hamiltonian H. Then the exact state vector in the Schrödinger picture $|\Psi(t)\rangle$ satisfies the Schrödinger equation

$$i\hbar\frac{\partial|\Psi(t)\rangle}{t} = \hat{H}|\Psi(t)\rangle \tag{1.25}$$

the solution of the (unperturbed) time-dependent Schrödinger equation is given as

$$|\Psi(t)\rangle = e^{-i\hat{H}t}|\Psi(0)\rangle \tag{1.26}$$

Introduce the time-dependent perturbation, we transfer the Schrödinger equation to:

$$i\hbar\frac{\partial|\Psi(t)\rangle}{\partial t} = (\hat{H} + \hat{H}^{ext})|\Psi(t)\rangle \tag{1.27}$$

The solution of the new Schrödinger equation within the first order perturbation theory is given by

$$|\Psi(t)\rangle = e^{-i\hat{H}t}|\Psi(0)\rangle - i\hbar^{-1}e^{-i\hat{H}t}\int_{t_0}^{t} dt'\hat{H}^{ext}_{H'}(t')|\Psi(0)\rangle \tag{1.28}$$

Hence the expectation value of $\hat{O}(t)$ is in the form

$$\begin{aligned}\langle\hat{O}\rangle(t) &= \langle\Psi_H(0)|\hat{O}_H(t)|\Psi_H(0)\rangle \\ &+ i\hbar^{-1}\langle\Psi_H(0)|\int_{t_0}^{t} dt'[\hat{H}_H^{ext}(t'),\hat{O}_H(t)]|\Psi_H(0)\rangle \end{aligned} \tag{1.29}$$

we require $\langle\Psi_H(0)|\hat{O}_H(t)|\Psi_H(0)\rangle = 0$, and then the second term measures the fluctuation of the observable away from the expectation value. We use H_{ext} to represent an external source which couples linearly to the observable,

$$H_{ext} = \int d^3r\hat{O}(r,t)f(r,t) \tag{1.30}$$

Therefore, the change in the expectation value of the observable induced by the source $f(r't')$ is

$$\langle\hat{O}\rangle(t) = i\hbar^{-1}\int_{t0}^{t} dt'\langle\Psi_H(0)|\hat{O}(r',t'),\hat{O}(r,t)|\Psi_H(0)\rangle f(r',t') \tag{1.31}$$

Thus we define a generalized response function $\chi(r,r',t,t')$

$$\langle\hat{O}\rangle(t) = \chi\cdot f = \int d^3r\int_{t0}^{t} dt'\chi(r,r',t,t')f(r',t') \tag{1.32}$$

We expand $f(r,t)$ in the Fourier series:

$$f(r,t) = \frac{1}{2\pi}\int d\omega e^{-i\omega t}f(r,\omega) \tag{1.33}$$

where $f(r,\omega) = \frac{1}{2\pi}\int dt e^{i\omega t}f(r,t)$.

Then we can define the Fourier transform of the response function

$$\chi(r,r',\omega) = i\hbar^{-1}\int_{t_0}^{0} e^{i\omega\tau}\langle\Psi_H(0)|[\hat{O}_H(0,r),\hat{O}_H(\tau,r')]|\Psi_H(0)\rangle \tag{1.34}$$

1.5 Master Equation Method

Qunatum Mechanics of open system is required to consider the decay rate of a quantum State. Such a decay rate, for example, arising from the coupling of the quantum system to its reservoir. One general method to study the influence of a

reservoir upon a quantum state is the master equation method. In this section, we will introduce the master equation description of an open system in terms of a density operator based on [30].

In this thesis, $\tilde{\rho}_s$ stands for the reduced density matrix of the system in the interaction picture, and ρ_s stands for the reduced density matrix of the system in the Schrödinger picture. We characterize the quantum system through the density operator,

$$\rho(t) = |\psi(t)\rangle\langle\psi(t)| \tag{1.35}$$

Where $|\psi(t)\rangle$ is a pure state of the open quantum system. Consider the Hamiltonian of the total system given as

$$H = H_0 + H_I \tag{1.36}$$

here H_0 includes both the Hamiltonian of the system and of the reservoir in complete neglecting coupling $H_0 = H_S + H_E$. Meanwhile H_I represents the system and reservoir interaction. In the interaction picture, evolution of the density operator has the form

$$\frac{\partial\tilde{\rho}(t)}{\partial t} = -i[\tilde{H}_I(s), \tilde{\rho}(s)] \tag{1.37}$$

Henceforth $\hbar = 1$ unless explicitly written. This equation has the formal solution

$$\tilde{\rho}(t) = \tilde{\rho}(0) - i\int_0^t ds[\tilde{H}_I(s), \tilde{\rho}(s)] \tag{1.38}$$

Substituting back into Eq.1.37, we get

$$\frac{\partial\tilde{\rho}(t)}{\partial t} = -i[\tilde{H}_I(t), \tilde{\rho}(0)] - \int_0^t ds[\tilde{H}_I(t), [\tilde{H}_I(s), \tilde{\rho}(s)]] \tag{1.39}$$

We move to reduced density operator $\tilde{\rho}_s$ by taking the trace over the environment: $\mathrm{Tr}_{res}\frac{\partial\tilde{\rho}_s(t)}{\partial t}$. Then the dynamics of the reduced density operator $\frac{\partial\tilde{\rho}_s(t)}{\partial t}$ in the interaction picture is given by :

$$\frac{\partial\tilde{\rho}_s(t)}{\partial t} = -i\mathrm{Tr}_E[\tilde{H}_I(t), \tilde{\rho}(0)] - \int_0^t ds\mathrm{Tr}_E[\tilde{H}_I(t), [\tilde{H}_I(s), \tilde{\rho}(s)]] \tag{1.40}$$

As the bath is in the stationary thermal state, and the interaction Hamiltonian contains only one bath creation (or one annihilation operator, $\mathrm{Tr}_E[\tilde{H}_I(t), \tilde{\rho}(0)] = 0$.

If we iterate this equation, the right side has higher order terms, so we make some simplifications. Assumptions are made:
(1) At $t = 0$, there is no interaction between S and E.
(2) We assume H_I is weak, and the bath is large enough and unaffected by the system. Then the total density operator can be factorized:

$$\tilde{\rho}(t) = \tilde{\rho}_s(t)\rho_E \tag{1.41}$$

within the Born approximation, we can neglect higher order terms. Then the master equation has the form

$$\frac{\partial \tilde{\rho}_s(t)}{\partial t} = -\int_0^t ds \mathrm{Tr}_E[\tilde{H}_I(t), [\tilde{H}_I(s), \tilde{\rho}_s(s)\rho_E]] \tag{1.42}$$

(3) Withen the Markov approximation: $\tilde{\rho}_s(t)$ only depends on its present state: $\tilde{\rho}_s(s) \to \tilde{\rho}_s(t)$. Then we have

$$\frac{\partial \tilde{\rho}_s(t)}{\partial t} = -\int_0^t ds \mathrm{Tr}_E[\tilde{H}_I(t), [\tilde{H}_I(s), \tilde{\rho}_s(t)\rho_E]] \tag{1.43}$$

(4) Substituting $s \to t - \tau$ and extending the integration limit to infinity, which is possible since when the time is larger than the bath correlation time it does not contribute to the integral.

Then in the interaction picture, the master equation can be written:

$$\frac{\partial \tilde{\rho}_s(t)}{\partial t} = -\int_0^\infty d\tau \mathrm{Tr}_E[\tilde{H}_I(t), [\tilde{H}_I(t-\tau), \tilde{\rho}_s(t)\rho_E]] \tag{1.44}$$

So far we have been working in the interaction picture. The transformation of an operator, for example A in the Schrödinger to the interaction picture is given by

$$\tilde{A}_I = e^{iH_s(t-t_0)} A e^{-iH_s(t-t_0)} \tag{1.45}$$

here we define $U_0(t, t_0) = e^{-iH_S(t-t_0)}$. The reciprocate relation between the density matrix in the Schrödinger and the interaction picture has the form

$$\tilde{\rho}_s(t) = U_0^+(t, t_0)\rho_s(t)U_0(t, t_0) \tag{1.46}$$

From that we have

$$\begin{aligned}\frac{\partial}{\partial t}\tilde{\rho}_s(t) &= \frac{\partial}{\partial t}(U_0^+(t,t_0)\rho_s(t)U_0(t,t_0)) \\ &= i\left[H_s, U_0^+(t,t_0)\rho_s(t)U_0(t,t_0)\right] + U_0^+(t,t_0)\frac{\partial}{\partial t}\rho_s(t)U_0(t,t_0) \\ &= iU_0^+(t,t_0)[H_s,\rho_s(t)]U_0(t,t_0) + U_0^+(t,t_0)\frac{\partial}{\partial t}\rho_s(t)U_0(t,t_0) \qquad (1.47)\end{aligned}$$

Then we can find the density matrix in the Schrödinger picture

$$\frac{\partial}{\partial t}\rho_s(t) = -i[H_s,\rho_s(t)] + U_0(t,t_0)\dot{\tilde{\rho}}_s(t)U_0^+(t,t_0) \qquad (1.48)$$

The Master equation can be applied straightforwardly to many different problems. It allows to solve for the time-dependent expectation values of the system of observables of interest.

Chapter 2

Nonequilibrium Thermodynamics Approach for QED Heat Conduction between Graphene and a Polar Substrate

The thermal properties of graphene have been studied extensively [31, 32, 26, 7]. Graphene's thermal conductivity can reach extremely high values in suspended devices [6, 33, 28]. Recent studies have shown that the thermal conductivity of graphene is significantly reduced once it is supported on a substrates or embedded into another material [34, 35]. Given that interfacial thermal transport can strongly affect the thermal conductivity of nanocomposites [36], understanding how heat flows across the interface between graphene and a substrate is essential to design and optimize thermal coupling materials[37]. Next we will briefly review recent experimental and theoretical studies of thermal properties of graphene to give a background and motivation for our own work. We will develop a thermodynamic theory of heat transfer between graphene and the substrate based on the quantum master equation. Lastly, we will discuss the interfacial thermal conductance between graphene and the polar substrate such as SiC and SiO_2.

2.1 Review of Experimental work of Thermal Transport in Graphene

We begin with a brief review of experimental work for the thermal conductivity of graphene. In 2008, A. A. Balandin [38] showed for the first time that graphene has extremely high intrinsic thermal conductivity K, which can exceed that of carbon nanotubes, using an optothermal method based on Raman spectroscopy. In the experiment, a graphene layer was suspended across a trench and heated with laser light (Fig.2.1), and a Raman spectrometer acted as a thermometer measuring the local temperature rise in graphene. They found that the intrinsic thermal conductivity of suspended graphene at room temperature is in the range of 2000W/mK to 5000 W/mK[6]. Several independent studies confirmed the high values of thermal conductivity in graphene [39, 40]. In 2010, Cai [39] found thermal conductivity at room temperature in the range of 1500W/mK to 5000 W/mK for suspended high-quality chemical vapor deposited graphene.

The optothermal method have also been applied to measure the thermal conductivity of few-layer graphene [41]. In 2010, Ghosh [41] found that the thermal conductivity of FLG decreases with increasing number of layers and approaches the bulk graphite limit $\sim$ 2000 W/mK due to inelastic scattering between phonons. The thermal conductivity of supported graphene is lower than that in suspended graphene due to coupling to the substrate. Seol [42] found the thermal conductivity $\sim$ 2000 W/mK for graphene on SiO_2/Si near room temperature.

2.2 Theoretical Motivation

The thermal conductivity across the layer direction has been reported, with the total thermal conductance G of the Au/Ti/Graphene/SiO_2 sandwich was found to be 25MWm^{-2}K^{-1} at room temperature [7], which indicates that the thermal conductance of the Graphene/SiO_2 interface (also called the Kapitza thermal conductance [43]) is higher than 25MWm^{-2}K^{-1}. Understanding the physical mechanism of how

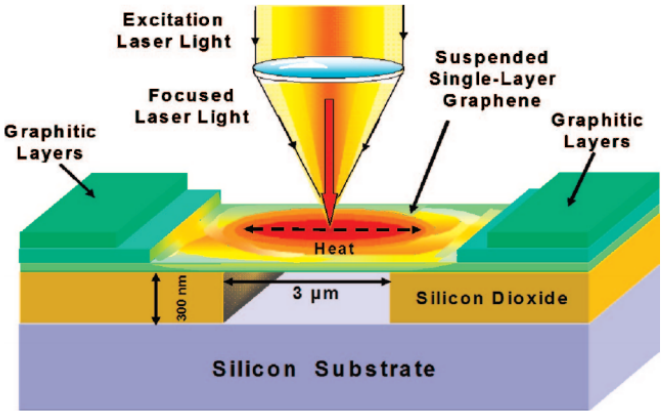

Figure 2.1: Schematic of suspended graphene structure used for measurements of thermal conductivity of graphene.[6]

heat flows across the interface may help us better understand the thermal properties of graphene. It is suggested that thermal transport at graphene/substrate interface could have a contribution from acoustic phonons in graphene and polar optical phonons in the substrate [7]. However, due to the weak van der Waals coupling between materials and the large mismatch between 2D and 3D phonon symmetry and DOS, this energy exchange mechanism has a low efficiency.

On the other hand, the plasmon is found to strongly couple with the mid-IR surface phonon of the SiO_2 substrate [44]. This strong coupling between surface plasmons in graphene and surface optical phonons in the substrate and resulting energy exchange may provide another channel for interfacial thermal transport.

In our work, we consider an open system which consists of surface plasmons and phonon polaritons that are coupled to each other and to the bulk optical phonons in graphene and in the substrate. The latter constitute thermal reservoirs. We assume that the reservoirs are large and have a short relaxation time scale. The surface modes are affected by coupling to the reservoir, and their energy is irreversibly dissipated into the reservoir. We assume the interaction between surface mode and reservoir is weak enough, and the reservoir is large enough not to be affected by the surface modes. We also assume different temperatures for the substrate and

graphene, so the coupled system is out of thermal equilibrium which creates a non-zero net heat flux ,(see Fig.2.2). Such an open system will be studied here by using a quantum master equation method. We will write a time-evolution equation for a reduced density matrix of the system, and then determine the system observables, such as the heat flux across the interface.

2.2.1 Surface Plasmon Damping in Graphene

Surface plasmons excited in graphene have a longer lifetime than in noble metals [45]. In the equation for graphene conductivity, one can phenomenologically introduce an intrinsic decay rate, which causes the plasmon frequency to have an imaginary part corresponding to a finite lifetime. Experiments [46, 47, 48] have studied the damping mechanisms of surface plasmons in graphene. Plasmons can decay into electron-hole pairs via inter- or intraband Landau damping, or decay into photons via a radiative process [46]. In addition, plasmons can interact with optical phonons, and impurities. Finite grain size and edge effects also could cause the damping of surface plasmons in graphene[48].

Within our model the lifetimes of the surface plasmons is finite due to the interaction with the surface optical phonon mode. Such a scattering rate can be calculated from electron self-energy due to interaction with optical phonons (see Appendix A). Plasmon lifetimes of 20 fs or less are observed in CVD graphene nanowires of small width[46] when damping via the emission of graphene optical phonon is allowed. In this work, we introduce a finite lifetime for the plasmons in graphene of $\approx$ 200fs in a phenomenological way.

2.2.2 Damping of surface phonon polaritons in substrate

Surface phonon polaritons (SPP) are lattice vibration modes of polar dielectrics coupled to the electromagnetic field at the surface, typically at far-infrared frequencies [49]. SPP can only propagate at the interface between two different materials, and the amplitude of the field decays exponentially with the distance from the interface [50]. The physics of SPP can is to that of surface plasmons and similar models can

	SiC	SiO_2	hBN
ϵ_0	9.7	3.90	5.09
ϵ_∞	6.5	2.50	4.1
ω_{TO}^1(meV)	97.1	55.6	97.4
ω_{TO}^2(meV)		138.1	187.6
ω_o^1(meV)	116	61.0	101.6
ω_o^2(meV)		149.0	195.7

Table 2.1: Material parameters for SiC, SiO_2, and hBN substrate.[2]

be used for theoretical description. The dispersion of surface phonon polaritons can be derived from Maxwell's equations, similar to surface plasmons in graphene. We consider a polar semiconductor, where the surface phonon polaritons excite at the interface with air/vacuum. The dispersion relation for the wave vector of SPPs is given by [50][51]:

$$k_{spp} = \frac{\omega}{c}\sqrt{\frac{\epsilon_1(\omega)\epsilon_2}{\epsilon_1(\omega)+\epsilon_2}}. \tag{2.1}$$

where k_{spp} is the wave vector along the surface. $\epsilon_1(\omega)$ and $\epsilon_2 = 1$ are dielectric function for a polar material and dielectric constant of the air, respectively. Frequency dependence of $\epsilon_1(\omega)$ can be modeled in vicinity of an optical phonon mode as:

$$\epsilon_1(\omega) = \epsilon_\infty \frac{\omega_L^2 - \omega^2}{\omega_T^2 - \omega^2} \tag{2.2}$$

where ϵ_∞ is the high frequency dielectric constant, ω_T is the transverse optical phonon frequency, and ω_L is the longitudinal optical phonon frequency. From Eq. 2.1, we can see that the peak of density of states for SPPs is given by frequency which satisfies eq: $\epsilon_1(\omega) = -1$. The frequency of the SPP is then close to the frequency of the optical phonon $\omega_{so} = \sqrt{\omega_T \frac{\epsilon_0+1}{\epsilon_\infty+1}}$, where ϵ_0 is the static permittivity. Material parameters for several substrates are given in Table 2.1.

We consider the damping of surface optical phonons based on the coupling of transverse optical bulk phonons with a finite lifetime. On the basis of Nkoma's work

[52], the relative energy loss for a single mode is

$$\gamma(k) = \frac{2\Gamma\langle U_k\rangle}{\langle U\rangle} \tag{2.3}$$

where $\langle U_k\rangle$ is the cycle-averaged density of the atomic oscillator kinetic energy in an electromagnetic field. $\langle U\rangle$ is the cycle-averaged total energy density including the kinetic and potential energies of the oscillator and the electromagnetic field energy. Then the energy loss rate of a surface phonon polariton is [52]:

$$\gamma_{op} = \frac{\frac{1}{2}\omega\frac{\partial\epsilon(\omega)}{\partial\omega}\Gamma_{TO}}{\epsilon(\omega)(1+\epsilon(\omega)+\frac{1}{2}\omega\frac{\partial\epsilon(\omega)}{\partial\omega}} \tag{2.4}$$

where the damping of transverse optical bulk phonons is $\Gamma_{TO} = 4.7cm^{-1}$ in SiO_2 [53] and $\Gamma_{TO} = 1.56cm^{-1}$ in SiC [54].

2.2.3 Coupled Modes between Graphene and Substrate

In this section we evaluate the coupling of SPPs in the polar substrate such as SiC and surface plasmons in the graphene. The surface phonons on the polar substrate produce an electric field coupled to the surface plasmons on the graphene shown in Fig.2.2. The interaction potential is given by

$$H_{int} = -\frac{1}{2}\int d^3r\hat{P}(r)\cdot\hat{E}(r) \tag{2.5}$$

$\hat{P}$ is the polarizaiton wave in the dielectric associated with a surface phonon polarization. This polarization wave can be expressed in the second quantization as [55]

$$\hat{P}(r) = \Sigma_q F\sqrt{q}e^{-qz+iqR}(\hat{z}-i\hat{R})\hat{b}_q^+ \tag{2.6}$$

Where b_q^+ is a creation operator of a surface phonon mode with two dimensional wave vector q. The vector normal to the solid at $(z>0)$ is $\hat{z}$, and unit vector along q is $\hat{R}$. The magnitude of the polarization field is controlled by the Frohlich coupling F.

$$F = \sqrt{\frac{\hbar\omega_{so}}{2\pi S}\left(\frac{1}{\varepsilon_\infty+1}-\frac{1}{\varepsilon_0+1}\right)} \tag{2.7}$$

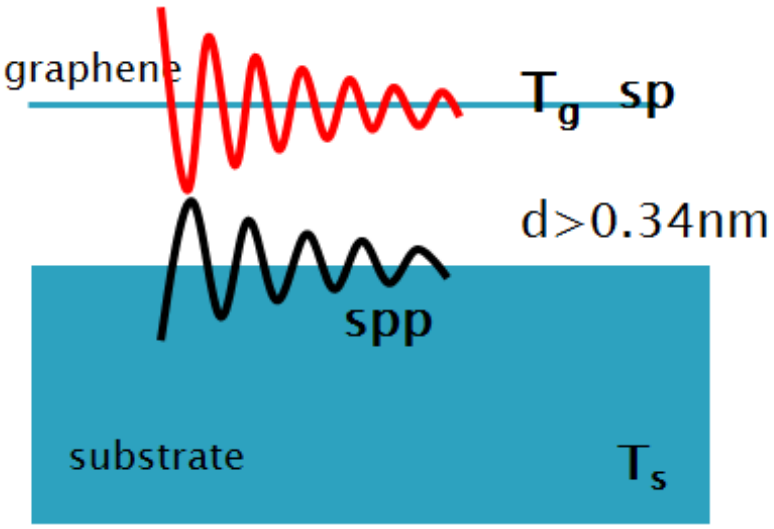

Figure 2.2: Schematic of the coupling of SPPs in the polar substrate and surface plasmons in graphene. The graphene and substrate have temperature T_g and T_s, respectively.

Where ω_{so} is a surface phonon energy and ϵ_0 and ϵ_∞ are static permittivity and high frequency dielectric constant of the polar substrate, given in Table 2.1. S is the contacting surface area. The graphene plasmonic field in the second quantization form is

$$\hat{E} = \sum_q A_q e^{-qz+iqR} \hat{a}_q^+ \tag{2.8}$$

Where $\hat{a}_q^+$ is the surface plasmon creation operator with wave vector q, and frequency ω_{sp}. A_q is the amplitude of the field. This unknown amplitude of the plasmonic mode is determined from the mean energy

$$\frac{1}{8\pi} \int d^3\mathbf{r} |\hat{E}|^2 = \sum_q \hbar\omega_{sp} a_q^+ a_q \tag{2.9}$$

which yields

$$A_q = \sqrt{\frac{2\pi\hbar\omega_{sp} q}{S}} \tag{2.10}$$

Then the interaction matrix has been derived

$$v_q = (2\pi)^2 SFA_q \frac{\sqrt{q}}{q}(e^{-2qd} - 1) \tag{2.11}$$

We write the effective Hamiltonian of the closed system

$$H_{eff} = \begin{pmatrix} \omega_{spp} & v_q \\ v_q & \omega_{sp} \end{pmatrix}$$

This Hamiltonian has two eigenvalues

$$z_{1,2} = \frac{(\omega_{spp} + \omega_{sp}) \pm \sqrt{(\omega_{spp} + \omega_{sp})^2 - 4(\omega_{spp}\omega_{sp} - v_q^2)}}{2} \tag{2.12}$$

Fig. 2.3 shows the dispersion behavior of coupled modes between the surface plasmon in graphene and SPPs in the SiC substrate, with graphene Fermi energy $E_F = 0.2$eV. We can see a crossover occurs at $q_c \approx 0.03\frac{eV}{\hbar V_F}$, which is determined by the Fermi energy of graphene, which is to say by the charge density of graphene. Each of the coupled modes $z_{1,2}$ has a "phonon-like" and a "plasmon-like" part. Those modes are assumed to provide the efficient heat flux channels.

2.3 Quantum Master Equations for Coupled System between Graphene and the Substrate

Our closed system contains SP (surface plasmon polariton in graphene surface) and SPP (surface phonon polariton in SiC substrate), which are strongly coupled via the interaction v_q. Such localized surface modes are, in fact, dissipated into reservoir modes such as optical phonon modes in the substrate and graphene. The interaction between surface modes and their corresponding reservoirs (environmental modes) leads to the loss of quantum coherence and the dissipation of their energy when driven out of equilibrium with their reservoirs. Assuming weak system-reservoir interactions which can be treated as a perturbation, and a short reservoir correlation time, Markovian quantum master equations can be used to describe relaxation dynamics of our system [56]. The open system Hamiltonian reads

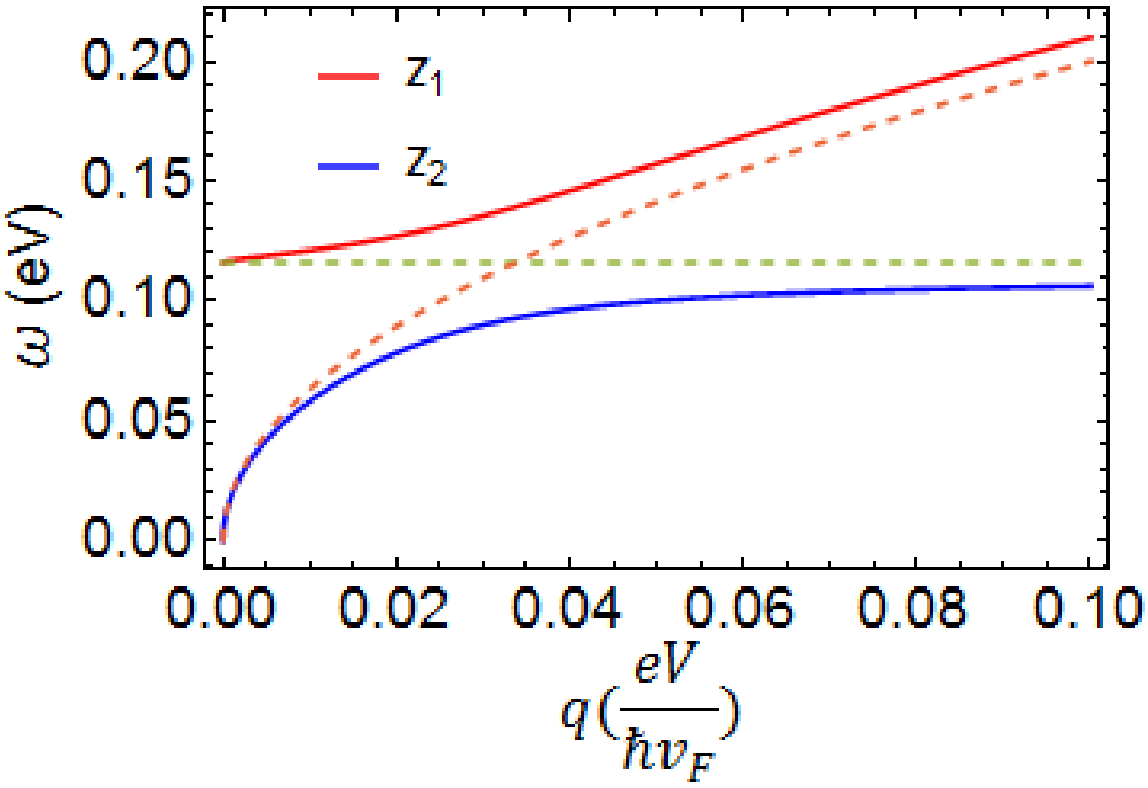

Figure 2.3: Schematic of coupling between plasmon and optical phonon mode of SiC. The Fermi energy of graphene is 0.2eV, the distance between graphene and the substrate is $d = 0.34nm$.

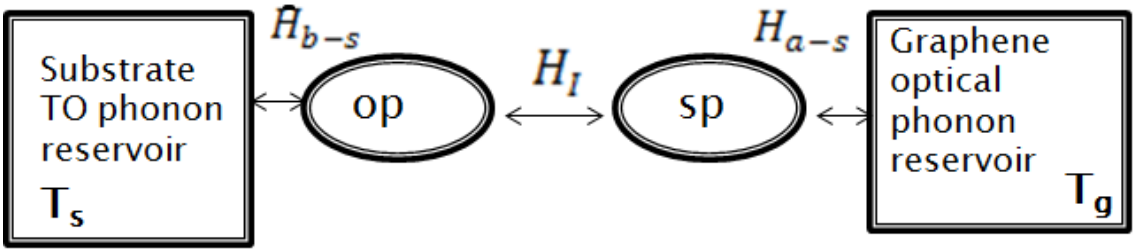

Figure 2.4: Schematic of the open system containing two subsystems, SP, and SPP. H_{a-s} and H_{b-s} are interaction Hamiltonians between the subsystem and its reservoir. H_I is the interaction Hamiltonian between the two subsystems.

Table 2.2: List of Notation

Notation	Meaning
op	surface optical phonon
sp	surface plasmon
ω_q^{sp}	frequency of surface plasmon in graphene
ω_q^{op}	frequency of surface optical phonon in the substrate
Ω_k^g	frequency of optical phonon in graphene
Ω_k^s	frequency of bulk optical phonon in the substrate
v_{kq}^s	coupling matrix element between op and its reservoir
v_{kq}^g	coupling matrix element between sp and its reservoir
$\hat{a}_q$	surface plasmon operator in graphene
$\hat{b}_q$	surface optical phonon operator in the substrate
$\hat{c}_k$	optical phonon operator in graphene
$\hat{d}_k$	optical phonon operator in the substrate
γ^{sp}	Linewidth of surface plasmon
γ^{op}	Linewidth of surface optical phonon

$$
\begin{aligned}
H &= H_{sp} + H_{op} + V + H_{res_1} + H_{res_2} + H_{a-s} + H_{b-s} \\
&= \sum_q \hbar\omega_q^{sp} \hat{a}_q^+ \hat{a}_q + \sum_q \hbar\omega_q^{op} \hat{b}_q^+ \hat{b}_q + \sum_q v_q(\hat{a}_q^+ \hat{b}_q + \hat{b}_q^+ \hat{a}_q) \\
&+ \sum_k \Omega_k^g \hat{c}_k^+ \hat{c}_k + \sum_k \Omega_k^s \hat{d}_k^+ \hat{d}_k \\
&+ \sum_{kq} v_{kq}^s(\hat{d}_k^+ \hat{b}_q + \hat{b}_q^+ \hat{d}_k) + \sum_{kq} v_{kq}^g(\hat{a}_q^+ \hat{c}_k + \hat{c}_k^+ \hat{a}_q)
\end{aligned} \tag{2.13}
$$

Here, we consider a system containing a two subsystem surface optical phonon and surface plasmon with Hamiltonians H_{sp} and H_{op}, which are coupled via the interaction Hamiltonian V. Each of these subsystems is coupled to its respective reservoir via the interaction Hamiltonian H_{a-s} and H_{b-s} respectively. H_{res_1} and H_{res_2} are Hamiltonians for these independent reservoirs. The meaning of notations in the Hamiltonian is given in Table.2.2.

We group the Hamiltonian in Eq.2.13 so that the total Hamiltonian reads [57]:

$H = H_0 + H_I$ where

$$H_0 = \sum_q \hbar\omega_q^{sp}\hat{a}_q^+\hat{a}_q + \sum_q \hbar\omega_q^{op}\hat{b}_q^+\hat{b}_q + \sum_q v_q(\hat{a}_q^+\hat{b}_q + \hat{b}_q^+\hat{a}_q) + \sum_k \Omega_k^g\hat{c}_k^+\hat{c}_k + \sum_k \Omega_k^s\hat{d}_k^+\hat{d}_k \tag{2.14}$$

$$H_I = H_{I1} + H_{I2} = \sum_{kq} v_{kq}^s(\hat{d}_k^+\hat{b}_q + \hat{b}_q^+\hat{d}_k) + \sum_{kq} v_{kq}^g(\hat{a}_q^+\hat{c}_k + \hat{c}_k^+\hat{a}_q) \tag{2.15}$$

where we assume that the interaction Hamiltonian only involves both two subsystems and reservoirs. Then we move into the interaction picture:

$$\begin{aligned}
\tilde{H}_{I1}(t) &= e^{iH_0t}H_{I1}e^{-iH_0t} \\
&= \sum_{Kq} v_{kq}^s e^{iH_{ab}t}(\hat{d}_k^+ e^{i\Omega_k^s t}\hat{b}_q e^{-i\omega_{op}t} + \hat{b}_q^+ e^{i\omega_{op}t}\hat{d}_k e^{-i\Omega_k^s t})e^{-iH_{ab}t} \\
&= \sum_{q\alpha} e^{iVt}(A_\alpha(t)M_\alpha(t))e^{-iVt}
\end{aligned} \tag{2.16}$$

$$\begin{aligned}
\tilde{H}_{I2}(t) &= e^{iH_0t}H_{I2}e^{-iH_0t} \\
&= \sum_{qk} v_{kq}^g e^{iH_{ab}t}(\hat{c}_k^+ e^{i\Omega_k^g t}\hat{a}_q e^{-i\omega_q^{sp}t} + \hat{a}_q^+ e^{i\omega_q^{sp}t}\hat{d}_k e^{-i\Omega_k^s t})e^{-iH_{ab}t} \\
&= \sum_{q\alpha} e^{iVt}(B_\alpha(t)T_\alpha(t))e^{-iVt}
\end{aligned} \tag{2.17}$$

where $H_{ab} = \sum_q v_q(\hat{a}_q^+\hat{b}_q + \hat{b}_q^+\hat{a}_q)$, $V = \sum_q v_q(\hat{a}_q^+\hat{b}_q + \hat{b}_q^+\hat{a}_q)$, $A_1(t) = \hat{b}_q^+ e^{i\omega_{op}t}$, $A_2(t) = \hat{b}_q e^{-i\omega_{op}t}$, $B_1(t) = \hat{a}_q^+ e^{i\omega_q^{sp}t}$, $B_2(t) = \hat{a}_q e^{-i\omega_q^{sp}t}$. And $M_1(t) = \sum_k v_{kq}^s\hat{d}_k e^{-i\omega_k^s t}$, $M_2(t) = \sum_k v_{kq}^s\hat{d}_k^+ e^{-i\omega_k^s t}$, $T_1(t) = \sum_k v_{kq}^g\hat{c}_k e^{-i\omega_k^g t}$, $T_2(t) = \sum_k v_{qk}^g\hat{c}_k^+ e^{i\omega_k^g t}$.

Then we construct the master equation of the reduced density operator $\tilde{\rho}_S(t)$ of the two subsystems in the interaction picture following standard methods as we showed

in Chapter 1 Eq.1.44.

$$
\begin{aligned}
&\frac{\partial\tilde{\rho}_s(t)}{\partial t} = -\int_0^\infty d\tau \\
&\{\mathrm{Tr}_{res_1}[\tilde{H}_{I1}(t),[\tilde{H}_{I1}(t-\tau),\tilde{\rho}_s(t)\rho_{res_1}]] + \mathrm{Tr}_{res_2}[\tilde{H}_{I2}(t),[\tilde{H}_{I2}(t-\tau),\tilde{\rho}_s(t)\rho_{res_2}]]\} \\
= & -\int_0^\infty d\tau \mathrm{Tr}_{res_1}\left(\tilde{H}_{I1}(t)\tilde{H}_{I1}(t-\tau)\tilde{\rho}_s(t)\rho_{res_1} - \tilde{H}_{I1}(t-\tau)\tilde{\rho}_s(t)\rho_{res_1}\tilde{H}_{I1}(t)\right) \\
+ & \int_0^\infty d\tau \mathrm{Tr}_{res_1}\left(\tilde{H}_{I1}(t)\tilde{\rho}_s(t)\rho_{res_1}\tilde{H}_{I1}(t-\tau) - \tilde{\rho}_s(t)\rho_{res_1}\tilde{H}_{I1}(t-\tau)\tilde{H}_{I1}(t)\right) \\
- & \int_0^\infty d\tau \mathrm{Tr}_{res_2}\left(\tilde{H}_{I2}(t)\tilde{H}_{I2}(t-\tau)\tilde{\rho}_s(t)\rho_{res_2} - \tilde{H}_{I2}(t-\tau)\tilde{\rho}_s(t)\rho_{res_2}\tilde{H}_{I2}(t)\right) \\
+ & \int_0^\infty d\tau \mathrm{Tr}_{res_2}\left(\tilde{H}_{I2}(t)\tilde{\rho}_s(t)\rho_{res_2}\tilde{H}_{I2}(t-\tau) - \tilde{\rho}_s(t)\rho_{res_2}\tilde{H}_{I2}(t-\tau)\tilde{H}_{I2}(t)\right) \quad (2.18)
\end{aligned}
$$

Since the reservoirs are assumed to be in thermal equilibrium, we have:

$$\rho_{res_1} = \frac{e^{-H_{res_1}/k_BT_1}}{\mathrm{Tr}(e^{-H_{res_1}/k_BT_1})} \quad (2.19)$$

$$\rho_{res_2} = \frac{e^{-H_{res_2}/k_BT_2}}{\mathrm{Tr}(e^{-H_{res_2}/k_BT_2})}. \quad (2.20)$$

Substitute Eq.2.16 and Eq.2.17 into Eq.2.18, use the cyclic property of trace, for example, the first term in Eq.2.18 become

$$
\begin{aligned}
& \mathrm{Tr}_{res_1}\left(\tilde{H}_{I1}(t)\tilde{H}_{I1}(t-\tau)\tilde{\rho}_s(t)\rho_{res_1}\right) \\
= & \mathrm{Tr}_{res_1}\sum_{q\alpha q'\beta} e^{iVt}A_\alpha(t)M_\alpha(t)e^{-iV\tau}A_\beta(t-\tau)M_\beta(t-\tau)e^{-iV(t-\tau)}\tilde{\rho}_s(t)\rho_{res_1} \\
= & \mathrm{Tr}_{res_1}\sum_{q\alpha q'\beta} A_\alpha(t)e^{-iV\tau}A_\beta(t-\tau)e^{iV\tau}M_\alpha(t)M_\beta(t-\tau)\tilde{\rho}_s(t)\rho_{res_1}
\end{aligned}
\quad (2.21)
$$

Equation for Correlation Function We assume that that environment is in an equilibrium state. It is possible to obtain two-point correlations $C_{\alpha\beta}$ as a environment correlation function

$$C1_{\alpha\beta}(t,s) = \mathrm{Tr}_{res1}(M_\alpha(t)M_\beta(s)\rho_{res1}) \quad (2.22)$$

$$C2_{\alpha\beta}(t,s) = \mathrm{Tr}_{res2}(T_\alpha(t)T_\beta(s)\rho_{res2}) \tag{2.23}$$

where M_α and T_α are the environment operators. The correlation function measures how an excitation of the reservoir at t is correlated with the excitation at s. Since reserivors are in an equilibrium state, then $[H_{res}, \rho_{res}] = 0$. If we use the cyclic property of the trace, we can see some properties of the correlation function $C1$(same for $C2$).

$$\begin{aligned}
C1_{\alpha\beta}(t,s) &= \mathrm{Tr}_{res_1}(M_\alpha(t)M_\beta(s)\rho_{res_1}) \\
&= \mathrm{Tr}_{res_1}(e^{iH_{res}t}M_\alpha e^{-iH_{res_1}t}e^{iH_{res_1}s}M_\beta e^{-iH_{res_1}s}\rho_{res_1}) \\
&= \mathrm{Tr}_{res_1}(e^{iH_{res_1}t}M_\alpha e^{-iH_{res_1}t}e^{iH_{res_1}s}M_\beta\rho_{res_1}e^{-iH_{res_1}s}) \\
&= \mathrm{Tr}_{res_1}(e^{iH_{res_1}(t-s)}M_\alpha e^{-iH_{res_1}(t-s)}M_\beta\rho_{res_1}) \\
&= \mathrm{Tr}_{res_1}(M_\alpha(t-s)M_\beta\rho_{res_1}) \\
&= C_{\alpha\beta}(t-s)
\end{aligned} \tag{2.24}$$

and

$$C1_{\alpha\beta}(\tau) = \mathrm{Tr}_{res_1}(M_\alpha(t)M_\beta(t-\tau)\rho_{res_1}) \tag{2.25}$$

$$C1_{\beta\alpha}(-\tau) = \mathrm{Tr}_{res_1}(M_\beta(t-\tau)M_\alpha(t)\rho_{res1}) \tag{2.26}$$

Those properties show that for a reservoir describing thermal equilibrium the correlations should only depend on the time difference.

For a thermal equilibrium state ρ_{res}, the following averages are found

$$\begin{aligned}
\langle\hat{c}_k\hat{c}_{k'}\rangle &= \mathrm{Tr}_{res_1}(\hat{c}_k\hat{c}_{k'}\rho_{res_1}) = 0 \\
\langle\hat{d}_k\hat{d}_{k'}\rangle &= \mathrm{Tr}_{res_2}(\hat{d}_k\hat{d}_{k'}\rho_{res_2}) = 0 \\
\langle\hat{c}_k\hat{c}^+_{k'}\rangle &= \mathrm{Tr}_{res_1}(\hat{c}_k\hat{c}^+_{k'}\rho_{res_1}) = \delta(k-k')\,(1+N(\Omega^g_k)) \\
\langle\hat{d}_k\hat{d}^+_{k'}\rangle &= \mathrm{Tr}_{res_2}(\hat{d}_k\hat{d}^+_{k'}\rho_{res_2}) = \delta(k-k')\,(1+N(\Omega^s_k))
\end{aligned}$$

where

$$N(\omega) = \frac{1}{e^{\omega/k_BT}-1} \tag{2.27}$$

is the Bose-Einstein occupation number.

Substituting correlation functions into Eq.2.18, we find

$$\begin{aligned}
\frac{\partial\tilde{\rho}_s(t)}{\partial t} &= -\sum_{\alpha\beta qq'}\int_0^\infty d\tau\left([A_\alpha(t),e^{-iV\tau}A_\beta(t-\tau)e^{iV\tau}\tilde{\rho}_s(t)]C1_{\alpha\beta}(\tau)\right.\\
&+ \left.[\tilde{\rho}_s(t)e^{-iV\tau}A_\beta(t-\tau)e^{iV\tau},A_\alpha(t)]C1_{\beta\alpha}(-\tau)\right)\\
&- \sum_{\alpha\beta qq'}\int_0^\infty d\tau\left([B_\alpha(t),e^{-iV\tau}B_\beta(t-\tau)e^{iV\tau}\tilde{\rho}_s(t)]C2_{\alpha\beta}(\tau)\right.\\
&+ \left.[\tilde{\rho}_s(t)e^{-iV\tau}B_\beta(t-\tau)e^{iV\tau},B_\alpha(t)]C2_{\beta\alpha}(-\tau)\right) \qquad (2.28)
\end{aligned}$$

commutation relations for Bosons can be summarized as follows:

$$\begin{aligned}
[a_q,a_k] = \quad [a_q^+,a_k^+] &= [b_q,b_k] = [b_q^+,b_k^+] = 0 \qquad (2.29)\\
[a_q,a_k^+] &= [b_q,b_k^+] = \delta_{qk} \qquad (2.30)\\
[a_q,b_k^+] &= [a_q^+,b_k] = 0 \qquad (2.31)
\end{aligned}$$

Then by using Eq.2.32 and those commutation relations,if $B=\hat{b}_q$, $A=\sum_q v_q(\hat{a}_q^+\hat{b}_q+\hat{b}_q^+\hat{a}_q)$, then $[A,B]=i\tau v_q\hat{a}_q$, since

$$e^ABe^{-A} = B+[A,B]+\frac{1}{2}[A,[A,B]]+\ldots \qquad (2.32)$$

$$\begin{aligned}
e^{-iV\tau}\hat{b}_qe^{iV\tau} &= \hat{b}_q+i\tau v_q\hat{a}_q-\frac{1}{2!}\tau^2v_q^2\hat{b}_q-\frac{i}{3!}\tau^3v_q^3\hat{a}_q+\frac{1}{4!}\tau^4v_q^4\hat{b}_q+\cdots\\
&= \hat{b}_q(1-\frac{1}{2}\tau^2v_q^2+\frac{1}{4!}\tau^4v_q^4-\cdots)+i\hat{a}_q(\tau v_q-\frac{1}{3!}\tau^3v_q^3+\cdots)\\
&= \hat{b}_q\cos(v_q\tau)+i\hat{a}_q\sin(v_q\tau)\\
&= (e^{i\tau v_q}+e^{-i\tau v_q})\hat{b}_q/2+(e^{i\tau v_q}-e^{-i\tau v_q})\hat{a}_q/2 \qquad (2.33)\\
e^{-iV\tau}\hat{b}_q^+e^{iV\tau} &= (e^{i\tau v_q}+e^{-i\tau v_q})\hat{b}_q^+/2+(e^{i\tau v_q}-e^{-i\tau v_q})\hat{a}_q^+/2 \qquad (2.34)\\
C1_{12}(\tau) &= \sum_k|v_{kq}^s|^2e^{-i\Omega_k^s\tau}(1+N(\Omega_k^s)) \qquad (2.35)\\
C1_{21}(\tau) &= \sum_k|v_{kq}^s|^2e^{-i\Omega_k^s\tau}N(\Omega_k^s) \qquad (2.36)\\
C2_{12}(\tau) &= \sum_k|v_{kq}^g|^2e^{-i\Omega_k^g\tau}(1+N(\Omega_k^g)) \qquad (2.37)\\
C2_{21}(\tau) &= \sum_k|v_{kq}^g|^2e^{-i\Omega_k^g\tau}N(\Omega_k^g) \qquad (2.38)
\end{aligned}$$

We define the spectral density as

$$\begin{aligned} J(\omega) &= \sum_k |v_{kq}|^2 \delta(\omega - \omega_k) \\ &= \int D(\omega_k)|v_{kq}|^2 \delta(\omega - \omega_k) d\omega_k \\ &= D(\omega)|v_{kq}|^2 \end{aligned} \tag{2.39}$$

which is a measure of the system-reservoir coupling strength, weighted by the environmental density of states $D(\omega)$. In our model, the spectral density $J(\omega)$ can be identified as the linewidth of the localized surface modes.

$$\gamma_{sp} = \pi J(q)$$

$$\gamma_{op} = \pi J(\omega_q^{op}) \tag{2.40}$$

Now, we consider the integrals over τ on the correlation function, for example

$$\begin{aligned} \int_0^\infty d\tau e^{i\omega\tau} C1_{12}(\tau) &= \sum_{kq} |v_{k_q}|^2 (1 + N(\Omega_k^s)) \int_0^\infty d\tau e^{-i(\Omega_k^s - \omega)\tau} \\ &= \sum_q \int D(\omega)|v_{kq}|^2 (1 + N(\omega)) d\omega \int_0^\infty d\tau e^{-i(\omega - \omega')\tau} \\ &= \int_0^\infty d\tau \int_0^\infty d\omega \left(e^{i(\omega' - \omega)\tau} J(\omega)(1 + N(\omega)) \right) \end{aligned} \tag{2.41}$$

The time integral can be calculated with the help of

$$\int_0^\infty dt e^{-\pm i\omega t} = \pi\delta(\omega) \pm \mathbf{P}\frac{1}{\omega} \tag{2.42}$$

Then

$$\int_0^\infty d\tau e^{i\omega\tau} C1_{12}(\tau) = \gamma(\omega)(1 + N(\omega)) + i\mathbf{P} \int_0^\infty d\omega \frac{J(\omega)(1 + N(\omega))}{\omega' - \omega} \tag{2.43}$$

The imaginary part is the energy shift due to coupling to the reservoir and is ignored in our case. Then we combine all components to solve the master equation, for example

$$
\begin{aligned}
& \sum_{qq'} \int_0^\infty d\tau [\hat{b}_{q'}^+ e^{i\omega_{q'}^{op} t}, e^{i\tau v_q} \hat{b}_q \tilde{\rho}_s(t)] C1_{12}(\tau) \\
= & \sum_q \int_0^\infty d\tau \int d\omega e^{i(v_q + \omega_q^{op} - \omega)\tau} J(\omega)(1 + N(\omega))[\hat{b}_q^+, \hat{b}_q \tilde{\rho}_s(t)] \\
= & \pi J(v_q + \omega_q^{op})(1 + N(\omega))[\hat{b}_q^+, \hat{b}_q \tilde{\rho}_s(t)] \\
= & \gamma(v_q + \omega_q^{op})(1 + N(\omega))[\hat{b}_q^+, \hat{b}_q \tilde{\rho}_s(t)] \qquad (2.44)
\end{aligned}
$$

here

$$
\gamma(v_q + \omega_q^{op}) = \pi J(v_q + \omega_q^{op}) \qquad (2.45)
$$

Then we write the equation of motion for the reduced density matrix in the Schrödinger picture, see Eq.2.46.

$$
\begin{aligned}
\tfrac{\partial \rho_s(t)}{\partial t} &= -i\sum_q [\hbar\omega_q^{sp}\hat{a}_q^+\hat{a}_q + v_q(\hat{a}_q^+\hat{b}_q + \hat{b}_q^+\hat{a}_q) + \hbar\omega_q^{op}\hat{b}_q^+\hat{b}_q, \rho_s] \\
&- [\frac{\gamma(v_q+\omega_q^{op})}{2}(1+N^s(v_q+\omega_q^{op})) - \frac{\gamma(\omega_q^{op}-v_q)}{2}(1+N^s(\omega_q^{op}-v_q))][\hat{b}_q^+, \hat{a}_q\rho_s] \\
&- [\frac{\gamma(v_q+\omega_q^{op})}{2}(1+N^s(v_q+\omega_q^{op})) + \frac{\gamma(\omega_q^{op}-v_q)}{2}(1+N^s(\omega_q^{op}-v_q))][\hat{b}_q^+, \hat{b}_q\rho_s] \\
&- [\frac{\gamma(v_q+\omega_q^{op})}{2}N^s(v_q+\omega_q^{op}) - \frac{\gamma(\omega_q^{op}-v_q)}{2}N^s(\omega_q^{op}-v_q)][\rho_s\hat{a}_q, \hat{b}_q^+] \\
&- [\frac{\gamma(v_q+\omega_q^{op})}{2}N^s(v_q+\omega_q^{op}) + \frac{\gamma(\omega_q^{op}-v_q)}{2}N^s(\omega_q^{op}-v_q)][\rho_s\hat{b}_q, \hat{b}_q^+] \\
&- [\frac{\gamma(v_q+\omega_q^{op})}{2}N^s(v_q+\omega_q^{op}) + \frac{\gamma(\omega_q^{op}-v_q)}{2}N^s(\omega_q^{op}-v_q)][\hat{b}_q, \hat{b}_q^+\rho_s] \\
&- [\frac{\gamma(v_q+\omega_q^{op})}{2}N^s(v_q+\omega_q^{op}) - \frac{\gamma(\omega_q^{op}-v_q)}{2}N^s(\omega_q^{op}-v_q)][\hat{b}_q, \hat{a}_q^+\rho_s] \\
&- [\frac{\gamma(v_q+\omega_q^{op})}{2}(1+N^s(v_q+\omega_q^{op})) + \frac{\gamma(\omega_q^{op}-v_q)}{2}(1+N^s(\omega_q^{op}-v_q))][\rho_s\hat{b}_q^+, \hat{b}_q] \\
&- [\frac{\gamma(v_q+\omega_q^{op})}{2}(1+N^s(v_q+\omega_q^{op})) - \frac{\gamma(\omega_q^{op}-v_q)}{2}(1+N^s(\omega_q^{op}-v_q))][\rho_s\hat{a}_q^+, \hat{b}_q] \\
&- [\frac{\gamma(v_q+\omega_q^{sp})}{2}(1+N^g(v_q+\omega_q^{sp})) - \frac{\gamma(\omega_q^{sp}-v_q)}{2}(1+N^g(\omega_q^{sp}-v_q))][\hat{a}_q^+, \hat{b}_q\rho_s] \\
&- [\frac{\gamma(v_q+\omega_q^{sp})}{2}(1+N^g(v_q+\omega_q^{sp})) + \frac{\gamma(\omega_q^{sp}-v_q)}{2}(1+N^g(\omega_q^{sp}-v_q))][\hat{a}_q^+, \hat{a}\rho_s] \\
&- [\frac{\gamma(v_q+\omega_q^{sp})}{2}N^g(v_q+\omega_q^{sp}) - \frac{\gamma(\omega_q-v_q)}{2}N^g(\omega_q-v_q)][\rho_s\hat{b}_q, \hat{a}_q^+] \\
&- [\frac{\gamma(v_q+\omega_q^{sp})}{2}N^g(v_q+\omega_q^{sp}) + \frac{\gamma(\omega_q-v_q)}{2}N^g(\omega_q-v_q)][\rho_s\hat{a}_q, \hat{a}_q^+] \\
&- [\frac{\gamma(v_q+\omega_q^{sp})}{2}N^g(v_q+\omega_q^{sp}) + \frac{\gamma(\omega_q^{sp}-v_q)}{2}N^g(\omega_q^{sp}-v_q)][\hat{a}_q, \hat{a}_q^+\rho_s] \\
&- [\frac{\gamma(v_q+\omega_q^{sp})}{2}N^g(v_q+\omega_q^{sp}) - \frac{\gamma(\omega_q^{sp}-v_q)}{2}N^g(\omega_q^{sp}-v_q)][\hat{a}_q, \hat{b}_q^+\rho_s] \\
&- [\frac{\gamma(v_q+\omega_q^{sp})}{2}(1+N^g(v_q+\omega_q^{sp})) + \frac{\gamma(\omega_q^{sp}-v_q)}{2}(1+N^g(\omega_q^{sp}-v_q))][\rho_s\hat{a}_q^+, \hat{a}_q] \\
&- [\frac{\gamma(v_q+\omega_q^{sp})}{2}(1+N^g(v_q+\omega_q^{sp})) - \frac{\gamma(\omega_q^{sp}-v_q)}{2}(1+N^g(\omega_q^{sp}-v_q))][\rho_s\hat{b}_q^+, \hat{a}_q]
\end{aligned}
\tag{2.46}
$$

We apply the master equation to determine the equations of the mean values of

$\langle \hat{a}_q^+ \hat{a}_q \rangle$, $\langle \hat{b}_q^+ \hat{b}_q \rangle$, $\langle \hat{a}_q^+ \hat{b}_q \rangle$, and $\langle \hat{b}_q^+ \hat{a}_q \rangle$ by using

$$\begin{aligned}
\frac{\partial \langle \hat{a}_q^+ \hat{a}_q \rangle}{\partial t} &= \frac{\partial}{\partial t} \mathrm{Tr}(\hat{a}_q^+ \hat{a}_q \rho_s(t)) \\
&= \mathrm{Tr}(\frac{\partial \rho_s(t)}{\partial t} \hat{a}_q^+ \hat{a}_q) + \cancel{\mathrm{Tr}(\rho_s(t) \frac{\partial \hat{a}_q^+ \hat{a}_q}{\partial t})} \\
&= \mathrm{Tr}(\frac{\partial \rho_s(t)}{\partial t} \hat{a}_q^+ \hat{a}_q) \qquad (2.47)
\end{aligned}$$

and we use the cyclic property of the trace,

$$\begin{aligned}
\mathrm{Tr}([\hat{a}_q^+ \hat{a}_q, \rho_s] \hat{a}_{q'}^+ \hat{a}_{q'}) &= \mathrm{Tr}(\hat{a}_q^+ \hat{a}_q \rho_s \hat{a}_{q'}^+ \hat{a}_{q'} - \rho_s \hat{a}_q^+ \hat{a}_q \hat{a}_{q'}^+ \hat{a}_{q'} \\
&= \mathrm{Tr}(\rho_s \hat{a}_q^+ \hat{a}_q \hat{a}_{q'}^+ \hat{a}_{q'} - \rho_s \hat{a}_q^+ \hat{a}_q \hat{a}_{q'}^+ \hat{a}_{q'}) \\
&= 0 \qquad (2.48)
\end{aligned}$$

$$\begin{aligned}
\mathrm{Tr}([\hat{a}_q^+ \hat{b}_q, \rho_s] \hat{a}_{q'}^+ \hat{a}_{q'}) &= \mathrm{Tr}(\hat{a}_q^+ \hat{b}_q \rho_s \hat{a}_{q'}^+ \hat{a}_{q'} - \rho_s \hat{a}_q^+ \hat{b}_q \hat{a}_{q'}^+ \hat{a}_{q'}) \\
&= \mathrm{Tr}(\rho_s \hat{a}_{q'}^+ \hat{a}_{q'} \hat{a}_q^+ \hat{b}_q - \rho_s \hat{a}_q^+ \hat{b}_q \hat{a}_{q'}^+ \hat{a}_{q'}) \\
&= \mathrm{Tr}(\rho_s \hat{a}_{q'}^+ \hat{a}_q^+ \hat{a}_{q'} \hat{b}_q + \rho_s \hat{a}_q^+ \hat{b}_q - \rho_s \hat{a}_q^+ \hat{a}_{q'}^+ \hat{b}_q \hat{a}_{q'}) \\
&= \mathrm{Tr}(\rho_s \hat{a}_q^+ \hat{b}_q) = \langle \hat{a}_q^+ \hat{b}_q \rangle. \qquad (2.49)
\end{aligned}$$

and so forth, we can obtain a set of equations

$$\begin{aligned}
\tfrac{\partial \langle \hat{a}_q^+ \hat{a}_q \rangle}{\partial t} &= -iv_q(\langle \hat{a}_q^+ \hat{b}_q \rangle - \langle \hat{b}_q^+ \hat{a}_q \rangle) - 2\left(\frac{\gamma(v_q + \omega_q^{sp})}{2} + \frac{\gamma(\omega_q^{sp} - v_q)}{2}\right) \langle \hat{a}_q^+ \hat{a}_q \rangle \\
- &\quad \left(\frac{\gamma(v_q + \omega_q^{sp})}{2} - \frac{\gamma(\omega_q^{sp} - v_q)}{2}\right) (\langle \hat{a}_q^+ \hat{b}_q \rangle + \langle \hat{b}_q^+ \hat{a}_q \rangle) \\
+ &\quad \gamma(v_q + \omega_q^{sp}) N^g(v_q + \omega_q^{sp}) + \gamma(\omega_q^{sp} - v_q) N^g(\omega_q^{sp} - v_q) \qquad (2.50)
\end{aligned}$$

$$\begin{aligned}
\tfrac{\partial \langle \hat{b}_q^+ \hat{b}_q \rangle}{\partial t} &= -iv_q(\langle \hat{b}_q^+ \hat{a}_q \rangle - \langle \hat{a}_q^+ \hat{b}_q \rangle) - 2\left(\frac{\gamma(v_q + \omega_q^{op})}{2} + \frac{\gamma(\omega_q^{op} - v_q)}{2}\right) \langle \hat{b}_q^+ \hat{b}_q \rangle \\
- &\quad \left(\frac{\gamma(v_q + \omega_q^{op})}{2} - \frac{\gamma(\omega_q^{op} - v_q)}{2}\right) (\langle \hat{a}_q^+ \hat{b}_q \rangle + \langle \hat{b}_q^+ \hat{a}_q \rangle) \\
+ &\quad \gamma(v_q + \omega_q^{op}) N^s(v_q + \omega_q^{op}) + \gamma(\omega_q^{op} - v_q) N^s(\omega_q - v_0) \qquad (2.51)
\end{aligned}$$

$$
\begin{aligned}
\frac{\partial\langle\hat{b}_q^+\hat{a}_q\rangle}{\partial t} &= -\left(\frac{\gamma(v_q+\omega_q^{sp})}{2}-\frac{\gamma(\omega_q^{sp}-v_q)}{2}\right)\langle\hat{b}_q^+\hat{b}_q\rangle \\
- \quad & iv_q(\langle\hat{a}_q^+\hat{a}_q\rangle-\langle\hat{b}_q^+\hat{b}_q\rangle)-\left(\frac{\gamma(v_q+\omega_q^{op})}{2}-\frac{\gamma(\omega_q^{op}-v_q)}{2}\right)\langle\hat{a}_q^+\hat{a}_q\rangle \\
+ \quad & \left(i\omega_q^{sp}-\frac{\gamma(\omega_q^{sp}-v_q)}{2}-\frac{\gamma(v_q+\omega_q^{sp})}{2}\right)\langle\hat{a}_q^+\hat{b}_q\rangle \\
+ \quad & \left(-i\omega_q^{op}-\frac{\gamma(\omega_q^{op}-v_q)}{2}-\frac{\gamma(v_q+\omega_q^{op})}{2}\right)\langle\hat{a}_q^+\hat{b}_q\rangle \\
+ \quad & \frac{\gamma(v_q+\omega_q^{sp})N^g(v_q+\omega_q^{sp})-\gamma(\omega_q-v_q)N^g(\omega_q^{sp}-v_q)}{2} \\
+ \quad & \frac{\gamma(v_q+\omega_q^{op})N^s(v_q+\omega_q^{op})-\gamma(\omega_q^{op}-v_q)N^s(\omega_q^{sp}-v_0)}{2}
\end{aligned} \tag{2.52}
$$

$$
\begin{aligned}
\frac{\partial\langle\hat{a}_q^+\hat{b}_q\rangle}{\partial t} &= -(\frac{\gamma(v_q+\omega_q^{sp})}{2}-\frac{\gamma(\omega_q^{sp}-v_q)}{2})\langle\hat{b}_q^+\hat{b}_q\rangle \\
- \quad & iv_q(\langle\hat{b}_q^+\hat{b}_q\rangle-\langle\hat{a}_q^+\hat{a}_q\rangle)-\left(\frac{\gamma(v_q+\omega_q^{op})}{2}-\frac{\gamma(\omega_q^{op}-v_q)}{2}\right)\langle\hat{a}_q^+\hat{a}_q\rangle \\
+ \quad & \left(-i\omega_q^{sp}-\frac{\gamma(\omega_q^{sp}-v_q)}{2}-\frac{\gamma(v_q+\omega_q^{sp})}{2}\right)\langle\hat{b}_q^+\hat{a}_q\rangle \\
+ \quad & \left(i\omega_q^{op}-\frac{\gamma(\omega_q^{op}-v_q)}{2}-\frac{\gamma(v_q+\omega_q^{op})}{2}\right)\langle\hat{b}_q^+\hat{a}_q\rangle \\
+ \quad & \frac{\gamma(v_q+\omega_q^{sp})N^g(v_q+\omega_q)-\gamma(\omega_q^{sp}-v_q)N^g(\omega_q^{sp}-v_q)}{2} \\
+ \quad & \frac{\gamma(v_q+\omega_q^{op})N^s(v_q+\omega_q^{op})-\gamma(\omega_q^{op}-v_q)N^s(\omega_q^{sp}-v_0)}{2}
\end{aligned} \tag{2.53}
$$

2.3.1 Dynamics of Heat transfer in the Small Coupling Approximation

To study how heat flows across the graphene-substrate interface, we first assume that the coupling between local modes is weak. Therefore coupling between subsystems does not change the energy and wave function of each local mode.

$$\gamma(\omega_q^{sp}\pm v_q)\approx\gamma(sp) \tag{2.54}$$

$$\gamma(\omega_q^{op}\pm v_q)\approx\gamma(op) \tag{2.55}$$

The master equation in the small coupling approximation is:

$$\begin{aligned}\frac{\partial}{\partial t}\rho_S(t) &= -i[\sum_q \left(\hbar\omega_q^{sp}\hat{a}_q^+\hat{a}_q + \hbar\omega_q^{op}\hat{b}_q^+\hat{b}_q + v_q(\hat{a}_q^+\hat{b}_q + \hat{b}_q^+\hat{a}_q)\right), \rho_s] \\ &+ 2\gamma(sp)\hat{a}_q\rho_s\hat{a}_q^+ - \gamma(sp)n(\omega_q^{sp}) \\ &\times \left(\hat{a}_q^+\hat{a}_q\rho_s - 2\hat{a}_q^+\rho_s\hat{a}_q + \hat{a}_q\hat{a}_q^+\rho_s - 2\hat{a}_q\rho_s\hat{a}_q^+ + \rho_s\hat{a}_q^+\hat{a}_q + \rho_s\hat{a}_q\hat{a}_q^+\right) \\ &+ 2\gamma(op)\hat{b}_q\rho_s\hat{b}_q^+ - \gamma(op)n(\omega_q^{op}) \\ &\times (\hat{b}_q^+\hat{b}_q\rho_s - 2\hat{b}_q^+\rho_s\hat{b}_q + \hat{b}_q\hat{b}_q^+\rho_s - 2\hat{b}_q\rho_s\hat{b}_q^+ + \rho_s\hat{b}_q^+\hat{b}_q + \rho_s\hat{b}_q\hat{b}_q^+)\end{aligned} \tag{2.56}$$

Then the master equation can be divided into three parts.

$$\frac{\partial}{\partial t}\rho_s(t) = \frac{1}{i\hbar}[H_s, \rho_s(t)] - \Gamma_g\rho_s(t) - \Gamma_s\rho_s(t) \tag{2.57}$$

here

$$\begin{aligned}\Gamma_g\rho_s(t) &= 2\gamma(sp)\hat{a}_q\rho_s\hat{a}_q^+ - \gamma(sp)n(\omega_q^{sp}) \\ &\times \left(\hat{a}_q^+\hat{a}_q\rho_s - 2\hat{a}_q^+\rho_s\hat{a}_q + \hat{a}_q\hat{a}_q^+\rho_s - 2\hat{a}_q\rho_s\hat{a}_q^+ + \rho_s\hat{a}_q^+\hat{a}_q + \rho_s\hat{a}_q\hat{a}_q^+\right)\end{aligned} \tag{2.58}$$

$$\begin{aligned}\Gamma_s\rho_s(t) &= 2\gamma(op)\hat{b}_q\rho_s\hat{b}_q^+ - \gamma(op)n(\omega_q^{op}) \\ &\times (\hat{b}_q^+\hat{b}_q\rho_s - 2\hat{b}_q^+\rho_s\hat{b}_q + \hat{b}_q\hat{b}_q^+\rho_s - 2\hat{b}_q\rho_s\hat{b}_q^+ + \rho_s\hat{b}_q^+\hat{b}_q + \rho_s\hat{b}_q\hat{b}_q^+)\end{aligned} \tag{2.59}$$

where the first term describes the reversible motion of the system and shows the propagation of the states under the influence of the weak interaction between them; the second and third terms are dissipative terms due to the existence of the reservoirs. To obtain the time evolution of the average occupation, equations of the mean values are simplified as:

$$\frac{\partial}{\partial t}\langle \hat{a_q}^+\hat{a}_q\rangle = -iv_q(\langle\hat{a}_q^+\hat{b}_q\rangle - \langle\hat{b}_q^+\hat{a}\rangle) - 2\gamma(sp)\langle\hat{a}_q^+\hat{a}_q\rangle + 2\gamma(sp)n(\omega_q^{sp}, T_g) \tag{2.60}$$

$$\frac{\partial}{\partial t}\langle\hat{b}^+\hat{b}\rangle = -iv_q(\langle\hat{b}_q^+\hat{a}\rangle - \langle\hat{a}^+\hat{b}_q\rangle) - 2\gamma(op)\langle\hat{b}^+\hat{b}\rangle + 2\gamma(op)n(\omega_q^{op}, T_s) \tag{2.61}$$

$$\frac{\partial}{\partial t}\langle\hat{b}^+\hat{a_q}\rangle = (i\omega_q - i\omega_0 - \gamma(sp) - \gamma(op))\langle\hat{b}^+\hat{a_q}\rangle - iv_q(\langle\hat{a}_q^+\hat{a}_q\rangle - \langle\hat{b}_q^+\hat{b}_q\rangle) \tag{2.62}$$

$$\frac{\partial}{\partial t}\langle \hat{a}_q^+ \hat{b}_q \rangle = (i\omega_q^{op} - i\omega_q^{sp} - \gamma(sp) - \gamma(op))\langle \hat{a_q}^+ \hat{b} \rangle + iv_q(\langle \hat{a}_q^+ \hat{a}_q \rangle - \langle \hat{b}_q^+ \hat{b}_q \rangle) \quad (2.63)$$

where $\langle \hat{a_q}^+ \hat{a_q} \rangle$ and $\langle \hat{b}_q^+ \hat{b}_q \rangle$ stand for number of surface plasmon modes in graphene and surface optical modes in the substrate, respectively. The first term means number of modes exchanged due to the weak interaction between them; the second and third terms in both equations describe that modes decay to the reservoir and gained from the reservoir, respectively.

We can exactly solve the problem at steady state by setting that the derivative of average occupation equals zero, then we have

$$\langle \hat{a_q}^+ \hat{a_q} \rangle = \frac{v_q^2(\gamma_{sp}+\gamma_{op})(\gamma_{op}n_{op}+\gamma_{sp}n_{sp}) + \gamma_{sp}n_{sp}\gamma_{op}[(\omega_q^{sp}-\omega_q^{op})^2 + (\gamma_{sp}+\gamma_{op})^2]}{v_q^2(\gamma_{sp}+\gamma_{op})^2 + \gamma_{sp}\gamma_{op}[(\omega_q^{sp}-\omega_q^{op})^2 + (\gamma_{sp}+\gamma_{op})^2]} \quad (2.64)$$

$$\langle \hat{b}_q^+ \hat{b}_q \rangle = \frac{v_q^2(\gamma_{sp}+\gamma_{op})(\gamma_{op}n_{op}+\gamma_{sp}n_{sp}) + \gamma_{sp}n_{op}\gamma_{op}[(\omega_q^{sp}-\omega_q^{op})^2 + (\gamma_{sp}+\gamma_{op})^2]}{v_q^2(\gamma_{sp}+\gamma_{op})^2 + \gamma_{sp}\gamma_{op}[(\omega_q^{sp}-\omega_q^{op})^2 + (\gamma_{sp}+\gamma_{op})^2]} \quad (2.65)$$

$$\begin{aligned} & -iv_q(\langle \hat{b}_q^+ \hat{a}_q \rangle - \langle \hat{a}_q^+ \hat{b}_q \rangle) \\ = \; & v_q^2 \frac{2\gamma_{sp}\gamma_{op}(\gamma_{sp}+\gamma_{op})}{v_q^2(\gamma_{sp}+\gamma_{op})^2 + \gamma_{sp}\gamma_{op}[(\omega_q-\omega_0)^2 + (\gamma_{sp}+\gamma_{op})^2]}(n_{sp}-n_{op}) \end{aligned} \quad (2.66)$$

$$\begin{aligned} & v_q(\langle \hat{b}_q^+ \hat{a}_q \rangle + \langle \hat{a}_q^+ \hat{b}_q \rangle) \\ = \; & -v_q^2 \frac{2\gamma_{sp}\gamma_{op}(\omega_q^{op}-\omega_q^{sp})}{v_q^2(\gamma_{sp}+\gamma_{op})^2 + \gamma_{sp}\gamma_{op}[(\omega_q-\omega_0)^2 + (\gamma_{sp}+\gamma_{op})^2]} \end{aligned} \quad (2.67)$$

Fig.2.5 shows the occupation number of two modes at steady state as a function of wavevector. From the steady state expressions, if the coupling between two modes is zero ($v_q = 0$), then we find $\langle \hat{a}_q^+ \hat{a}_q \rangle = n_{\omega_q}$ and $\langle \hat{b}_q^+ \hat{b}_q \rangle = n_{\omega_{op}}$, which means that two uncoupled states are in thermal equilibrium with their reservoirs. Since in our system, the lifetime of surface plasmons $\tau_{sp} \approx 200ps$ is 22 times smaller than that of surface optical phonons, then the damping for surface optical phonons is much smaller than for surface plasmons, which means that in this case $\langle \hat{a}_q^+ \hat{a}_q \rangle \approx \langle \hat{b}_q^+ \hat{b}_q \rangle \approx n_{\omega_{sp}}$.Finally, from Eq.2.66, there is no exchange between two modes when $n_{\omega_{sp}} = n_{\omega_{op}}$.

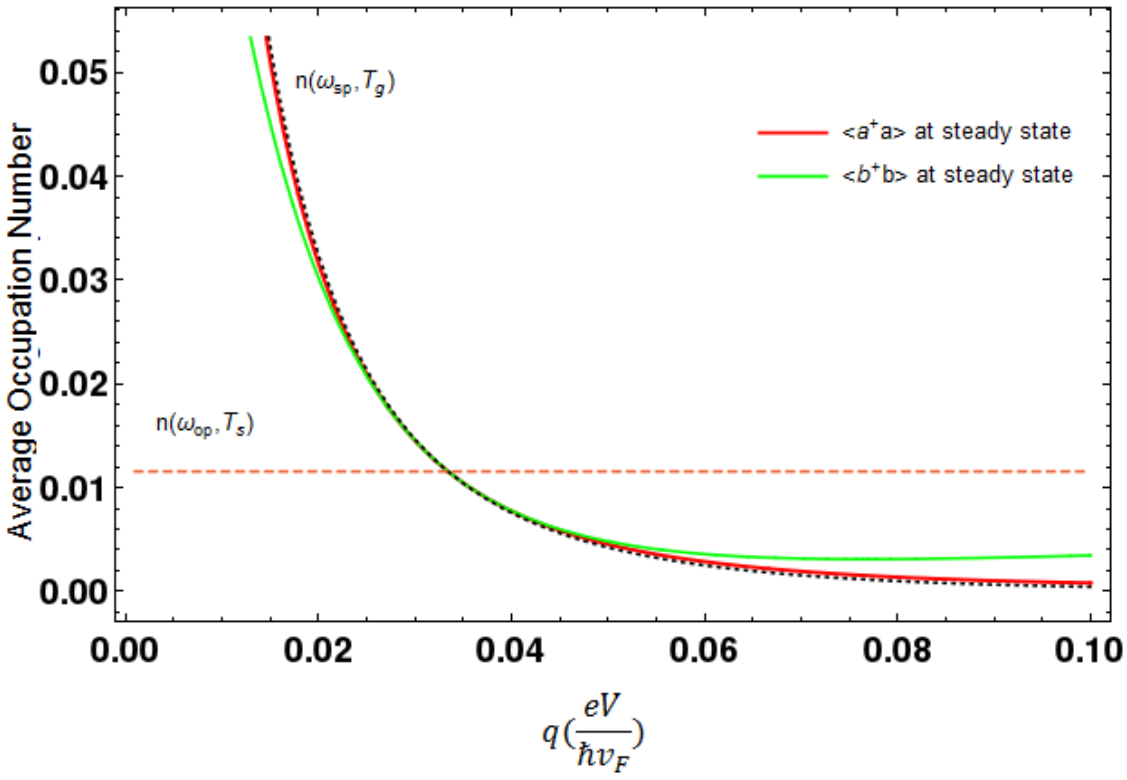

Figure 2.5: Occupation number of surface plasmon modes in graphene and surface optical phonon modes in the substrate at steady state for $T_g = 301K$, $T = 300K$ and $E_F = 0.2eV$. $n(\omega_{sp}, T_g)$ and $n(\omega_o p, T_s)$ are occupation number of surface plasmon modes and surface optical phonon modes which are assumed to be in thermal equilibrium at temperatures T_g and T_s, respectively.

The system Hamiltonian is given by

$$H_s = \sum_q \hbar\omega_q^{sp} \hat{a}_q^+ \hat{a}_q + \sum_q \hbar\omega_{op} \hat{b}_q^+ \hat{b}_q + \sum_q v_q (\hat{a}_q^+ \hat{b}_q + \hat{b}_q^+ \hat{a}_q) \tag{2.68}$$

Then the heat flux can be expressed as

$$\frac{\partial}{\partial t} Tr[H_s \rho_s(t)] = J_s + J_g + J_{sub} \tag{2.69}$$

here $J_s = -i\mathrm{Tr}[H_s[H_s, \rho_s(t)]] = 0$ is the heat flux from the system itself. $J_g = -\mathrm{Tr}[H_s \Gamma_g \rho_s(t)]$ and $J_{sub} = -\mathrm{Tr}[H_s \Gamma_{sub} \rho_s(t)]$ represent the incoming heat flux from

graphene and the substrate, respectively. At steady state, the sum of all heat flux is zero, $J_g + J_{sub} = 0$. The heat flow from graphene to substrate can be expressed in the form

$$\begin{aligned} J_g &= -\mathrm{Tr}[H_s \Gamma_g \rho_s(t)] \\ &= 2\pi \int_0^\infty q dq J_q^g \end{aligned} \tag{2.70}$$

where

$$\begin{aligned} J_q^g &= \omega_q^{sp} \Big(\gamma_{sp}(-2\langle \hat{a}_q^+ \hat{a}_q \rangle + 2n_{\omega_q^{sp}}) + v_q \gamma_{op}(-\langle \hat{b}_q^+ \hat{a}_q \rangle - \langle \hat{a}_q^+ \hat{b}_q \rangle \Big) \\ &= i\omega_q^{sp} v_q (\langle \hat{a}_q^+ \hat{b}_q \rangle - \langle \hat{b}_q^+ \hat{a}_q \rangle) + v_q \gamma_{op}(-\langle \hat{b}_q^+ \hat{a}_q \rangle - \langle \hat{a}_q^+ \hat{b}_q \rangle) \end{aligned} \tag{2.71}$$

here $\langle \hat{b}_q^+ \hat{a}_q \rangle + \langle \hat{a}_q^+ \hat{b}_q \rangle \approx 0$, the heat flux $J_q^g \approx i\omega_q^{sp} v_q (\langle \hat{a}_q^+ \hat{b}_q \rangle - \langle \hat{b}_q^+ \hat{a}_q \rangle)$.

2.4 Results and Discussions

In Fig.2.6 and Fig.2.7 , we plot dynamic behavior for $\langle \hat{a}_q^+ \hat{a}_q \rangle$ and $\langle \hat{b}_q^+ \hat{b}_q \rangle$. The calculating is done wave vector q less than the crossover wave vector q_c, and the temperature of the substrate slightly higher than that of graphene: $T_g = 301$K, $T_s = 300$K. Surface optical phonon frequency in SiC is $\omega_q^{op} = \omega_0 = 0.016eV$. First, we can see damped oscillatory behavior in both mean occupation numbers. The initial time (t=0) corresponds to both modes being in equilibrium with their reservoirs, which gives $\langle \hat{a}_q^+ \hat{a}_q \rangle = \frac{1}{e^{\omega_q / k_B T_g} - 1}$ and $\langle \hat{b}_q^+ \hat{b}_q \rangle = \frac{1}{e^{\omega_0 / k_B T_s} - 1}$. If $\omega_q / T_g < \omega_0 / T_s$, the initial average occupation of surface plasmons is higher than of surface optical phonons. Then surface plasmons in graphene generate a field which will excite surface optical phonons in the substrate. Since surface optical modes are damped, a part of the excitation energy is converted into heat, and surface optical phonons will excite surface plasmons in graphene and so forth until a steady state is reached. Furthermore, for a smaller wave vector $q = 0.01 \frac{eV}{\hbar v_F}$, there is no overlap between two modes decreases which diminishes the coupling; the overlap between two modes is the largest at $q = q_c$. From Fig.2.8, we clearly observe hybrid modes transferring back and forth between surface plasmons and optical phonons until a steady state

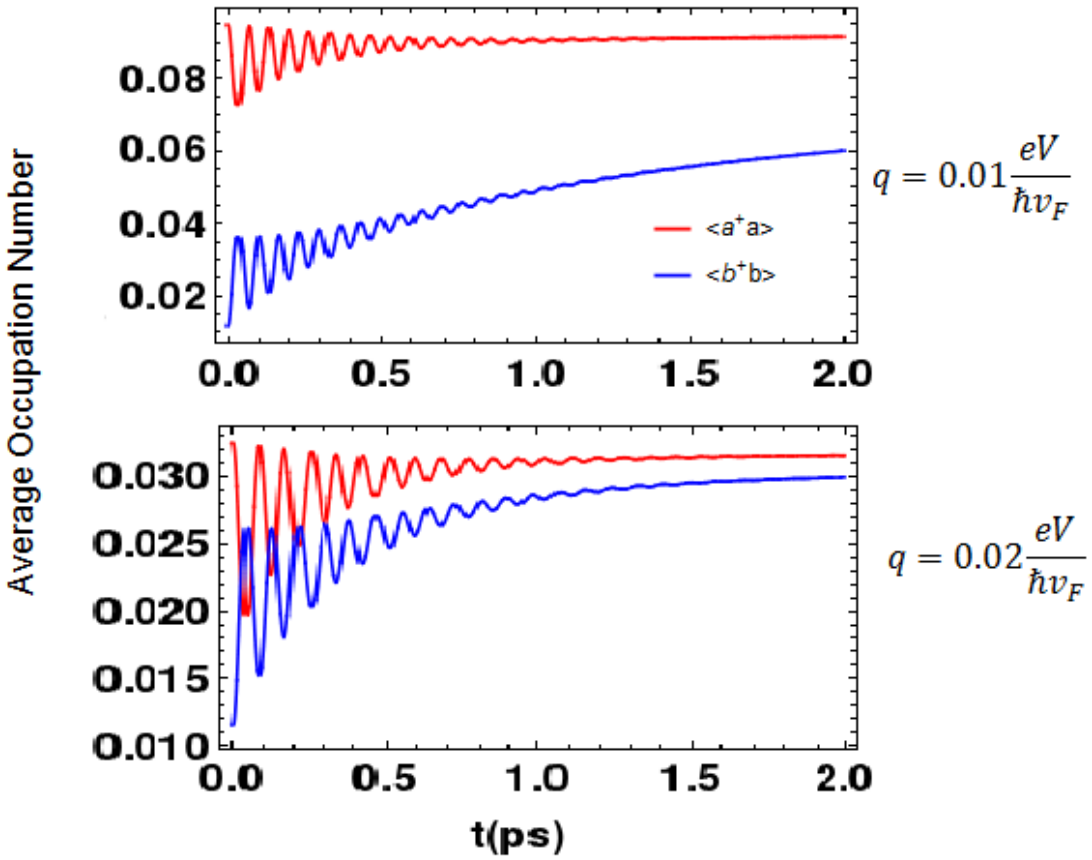

Figure 2.6: Dynamics of the average occupation number at wavevector $q = 0.01\frac{eV}{\hbar v_F}$(top) and $q = 0.02\frac{eV}{\hbar v_F}$(bottom). Temperature of graphene and the substrate are $T_g = 300K$ and $T_s = 301K$, respectively. The Fermi energy of graphene is $E_F = 0.2eV$.

is reached. For $q = q_c = 0.03364eV/\hbar v_F$, due to the strong overlap between two modes, we observe the shortest dynamic time, which we expected. Fig. 2.9 presents heat flux at steady state as a function of q. As the substrate has a higher temperature, the negative part of J_s indicates heat can flow from cold graphene to the hot substrate. The direction of heat flux is determined by $\frac{\omega}{T}$. If $\frac{\omega_g}{T_g} < \frac{\omega_s}{T_s}$, heat will flow from graphene to the substrate. However, the total heat flux has contributions from all modes, which is always positive when heat flows from the hot to the cold system,

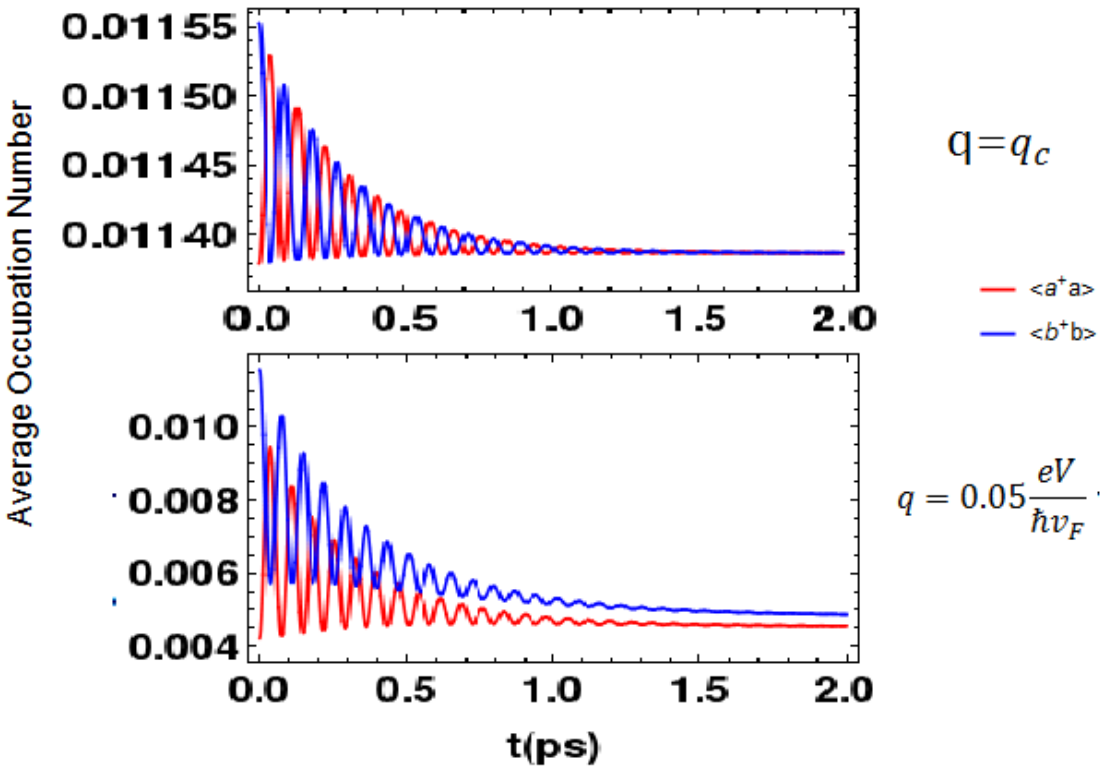

Figure 2.7: Dynamics of the average occupation number at wavevector $q = q_c$(top) and $q = 0.05eV$(bottom). The temperature of graphene and substrate are $T_g = 300K$ and $T_s = 301K$, respectively. The Fermi energy of graphene is $E_F = 0.2eV$, $q_c \approx 0.03364eV/\hbar v_F$ is the crossover wave vector.

to obey the second law of thermodynamics.

We can compare our results with the available experimental data in Fig.2.10 [7]. The interfacial thermal conductance measured at the $1-\mathrm{LG/SiO_2}$ interface is around $G = 2500$ to $7500Wm^{-2}K^{-1}$. Our computed value is about $2700Wm^{-2}K^{-1}$ at $E_F = 0.2eV$, which is in the experimental range. One can see that the interaction between surface plasmon modes in graphene and surface optical modes in the substrate provide the effective heat flux channels.

In conclusion, We have developed a thermodynamic theory of heat transfer between graphene and a substrate based on the master equation method. We show

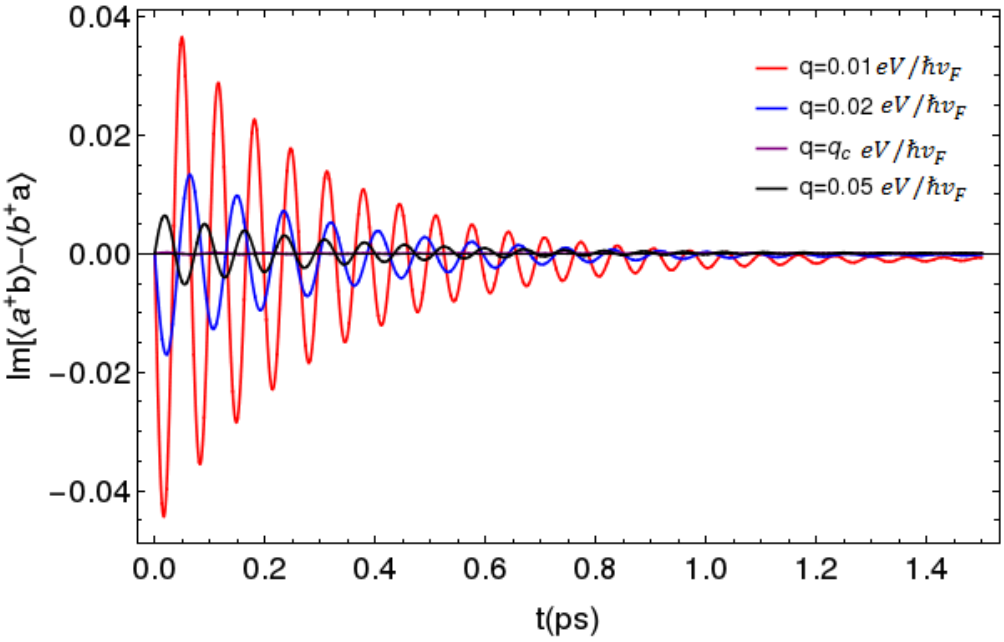

Figure 2.8: Dynamics of $Im[\langle \hat{a}^{+}\hat{b}\rangle - \langle \hat{b}^{+}\hat{a}_{q}\rangle]$ at different q, for $T_s = 301K$,$T_g = 300K$, $E_F = 0.2eV$.

that one of the heat transfer mechanisms between graphene and the substrate is due to coupling between surface plasmon and surface optical phonon modes.

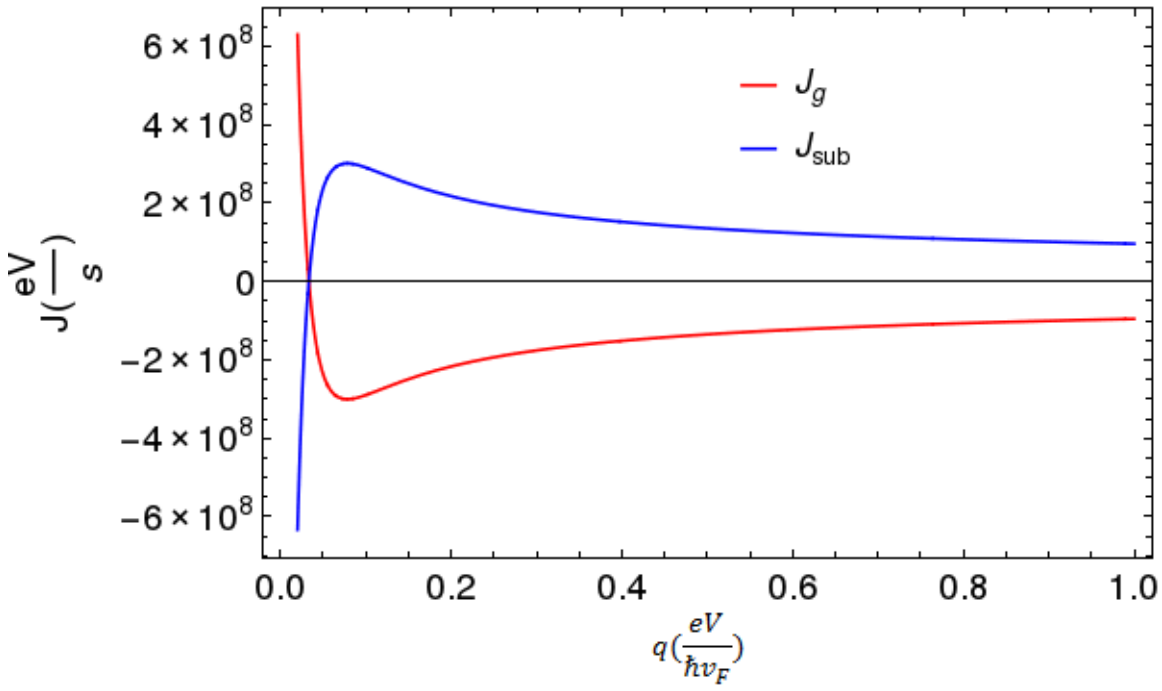

Figure 2.9: Steady state heat flux that is coming from graphene J_g and coming from substrate J_{sub} for $T_s = 301K$,$T_g = 300K$.

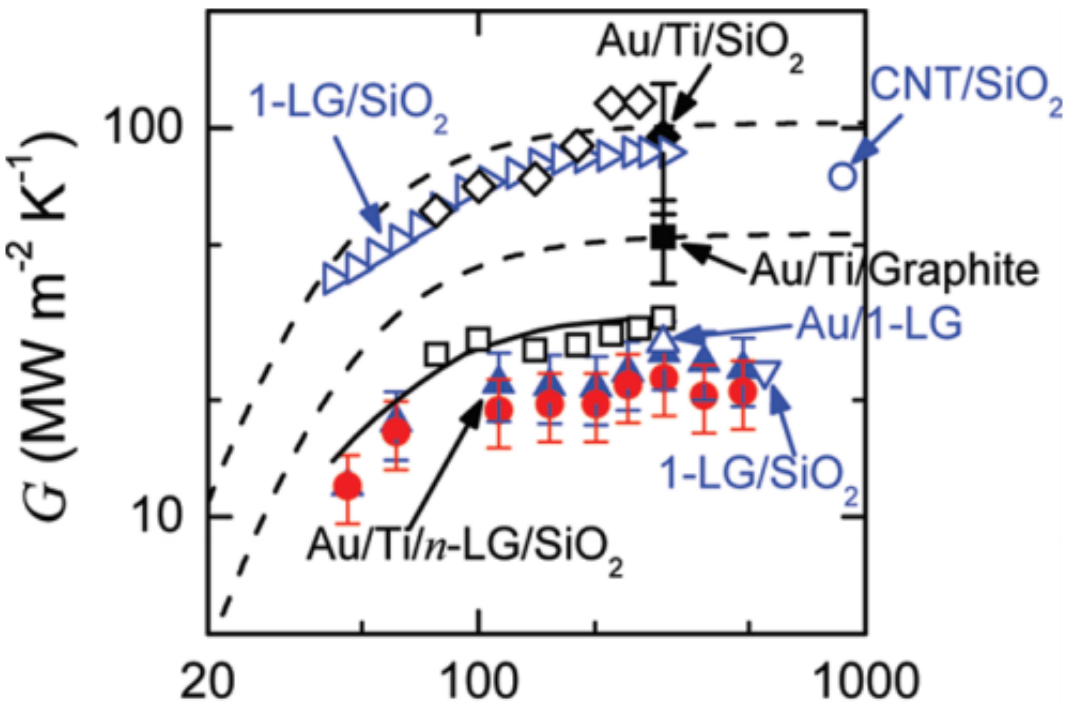

Figure 2.10: Temperature dependence of interfacial thermal conductance[7].

Chapter 3

Plasmons and Response Function of Graphene Nanodisk

3.1 Experimental Motivation for our Work

Plasmons in graphene nanostructures have attracted significant interest recently [58] [59]. Due to the dimensional confinement, plasmons in graphene nanostructures have different properties[60] compared to the bulk graphene. Combining graphene with heterostructures of other materials can produce unusual plasmonic behavior. For instance, graphene/boron nitride (BN) heterostructures exhibit plasmonic hybridization and reduction of plasmon damping; energy transfer between graphene plasmons and surface phonon polaritons was demonstrated in graphene/BN-nanotube heterostructures [61]. Graphene on the Al_2O_3 substrates exhibited edge plasmons [62]. However, the graphene-graphene "heterostructure", that is, graphene nanostructures supported or covered by a monolayer graphene (MLG), have been less explored so far.

Experiments have been done in Professor Xu's group in the Chemistry Department at Lehigh University. They studied monolayer graphene, transferred to a Si/SiO_2 substrate. Some of the samples were found to contain the bilayer structures. One of the structures showed signals with an interesting symmetry pattern.

They utilized s-SNOM (scanning scattering near-field optical microscopy) to investigate both the geometry of the bilayer structure and the plasmonic response. The structure was formed by a nanodisk buried underneath a continuous very large monolayer graphene. Fig. 3.1(a) shows AFM topography of the system. A white dashed circle is drawn to show the location of the disk. Fig. 3.1(b) illustrates the sketch of the graphene-graphene heterostructure and the near-field scattering probe. From the AFM and s-SNOM images, the size was determined to be around 400nm in diameter, which is comparable to the experimentally determined wavelength of surface plasmons in the monolayer graphene. Due to the geometric constriction of the nanodisk, plasmon modes should be quantized in the angular and radial directions. The s-SNOM image taken at the frequency of $1380cm^{-1}$ is shown in figure 3.1(c). It shows a circular pattern with full axial symmetry and a high signal enhancement at the center of the nanodisk. This pattern may correspond to the $L = 0$ (full circular symmetry) plasmon mode, this is an expected result. However, for the higher frequencies, for example at $1580cm^{-1}$ in Fig.3.1(d), a hexagonal symmetry mode with a central peak and a 4-fold symmetry pattern are observed. The most striking fact is that the corresponding reciprocal lattice vector of graphene is too large to attribute this pattern to the graphene lattice itself. Thus, this is a mesoscopic effect that needs to be explained.

3.2 Plasmons in the Single Disk Graphene

To understand the experimentally observed phenomena, we start by introducing a model describing the surface plasmon in a single disk of graphene. We introduce a simple, analytical procedure to describe the plasmon modes in graphene nanodisks using the concept of the plasmon wave function, which we identify with the charge density associated with these modes. Since the plasmon wavelength in a graphene nanodisk is much smaller than the wavelength of light, the general strategy is to solve the Poisson equation for the electrostatic potential $\phi(r)$, with the surface charge boundary condition and the edge current boundary condition due to the finite size of

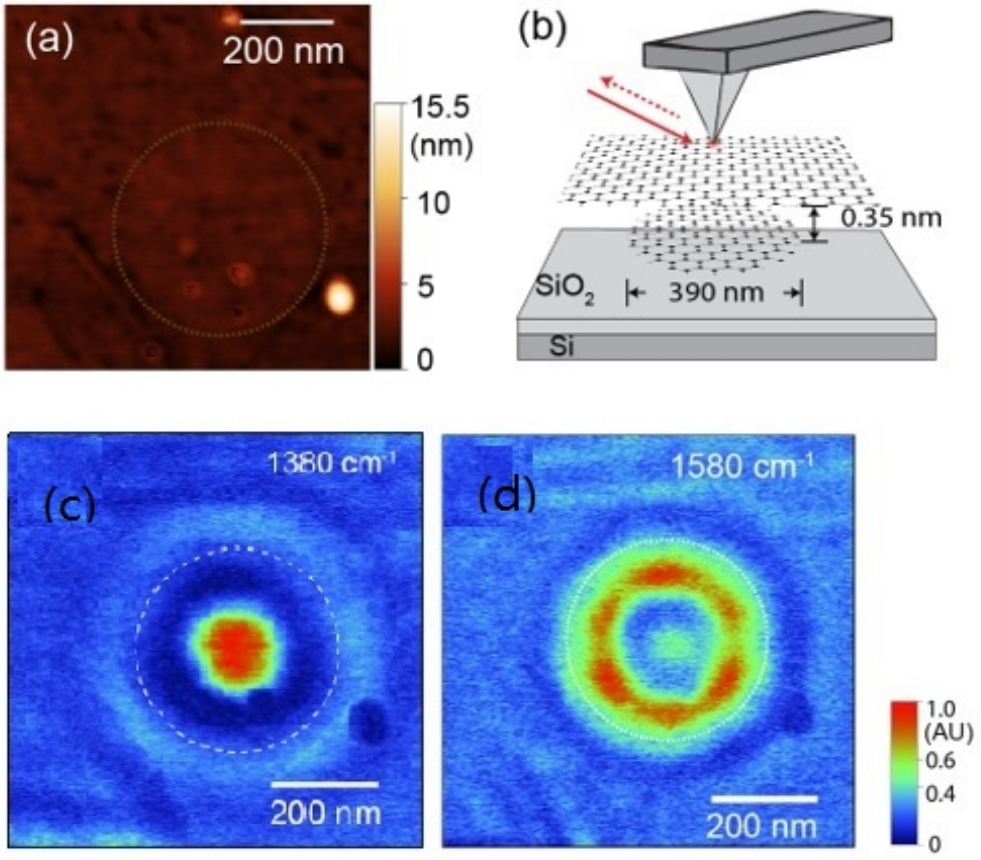

Figure 3.1: The graphene nano-disk heterostructure: (a) the topography of the graphene nanodisk heterostructure. The boundary is marked with a dashed circle. The diameter is about 390 nm. (b) The scheme of the graphene heterostructure, a monolayer graphene disk covered by a continuous graphene layer. (c) The s-SNOM image was taken at frequency of $1380 cm^{-1}$ and (d) at the frequency of 1580 cm^{-1}.

the graphene disk. The complete solution in a two-dimensional conductive disk was developed by Fetter [63], in which the wave function was described using a complete basis set of Legendre Polynomials. Recent papers [64, 65, 66] have numerically solved the model to yield the frequency of plasmons as well as other quantities in a single graphene disk by using Fetter's method.

Here, we used the method introduced by Gersten [67] to describe the surface plasmon modes of a finite disk analytically. For the finite disk, the 2D-continuum wavevector is no longer an appropriate quantum number to describe the surface plasmon modes due to constriction of the geometry. The frequencies of the oscillations assume discrete values and are labeled by two quantum numbers: the angular quantum number and the radial quantum number.

3.2.1 Discrete Eigenmodes of the Surface Plasmons in a Graphene Nanodisk

Assume that graphene sheet surrounds the plane z=0, with dielectric constants ϵ_0 and ϵ_b above and below, respectively. The conductivity of graphene is expressed by the Drude model [17]

$$\sigma(\omega) = \frac{ie^2 E_F}{\pi\hbar^2(\omega + i\tau^{-1})}. \tag{3.1}$$

where the Fermi energy $E_F = 0.3eV$, τ^{-1} is the electron relaxation rate related to the damping of electron in graphene. ω is the frequency of the external field. The plasmons can be obtained from the following two equations: the current density equation reads as,

$$\mathbf{J}(\mathbf{r}_{||}, \omega) = \sigma(\mathbf{r}_{||}, \omega)\mathbf{E}(\mathbf{r}_{||}, z = 0). \tag{3.2}$$

where J is the 2D current along the graphene layer, $\mathbf{E}$ is the external electric field, and σ is the 2D conductivity of graphene. The position of the graphene disk is at $z = 0$, $\mathbf{r}_{||} = (r, \theta)$ is polar coordinate. The second equation is the continuity equation,

$$\nabla_{||} \cdot \mathbf{J}(\mathbf{r}_{||}) = -i\omega\rho(\mathbf{r}_{||}). \tag{3.3}$$

Here $\rho(\mathbf{r}_{||})$ is the surface charge density in graphene, which can be related to the electrostatic potential by combining the continuity equation (3.3) and the surface current density equation (Eq.3.2) as:

$$\rho(\mathbf{r}_{||}) = \frac{\sigma(\omega)}{i\omega}\nabla_{||}^2\phi(\mathbf{r}_{||}, z=0) \tag{3.4}$$

In the absence of external source the electrostatic potential satisfies Laplace's equation for $z \neq 0$ in cylindrical coordinates:

$$\left(\frac{1}{r}\frac{\partial}{\partial r}r\frac{\partial}{\partial r} - \frac{L^2}{r^2} + \frac{\partial^2}{\partial z^2}\right)\phi(\mathbf{r}) = 0 \tag{3.5}$$

and allows separation of variable via $\phi(\mathbf{r}) = \phi(r,z)e^{iL\theta} = \phi(r)\phi(z)e^{iL\theta}$. We can express $\phi(\mathbf{r})$ as a Fourier Bessel integral:

$$\phi(\mathbf{r}) = \sum_L \int_0^\infty kdk\phi_{Lk}(z)J_L(kr)e^{iL\theta} \tag{3.6}$$

here $J_L(kr)$ is the Bessel function of order L. We substitute Eq.3.6 into Eq.3.5, and get

$$\left(k^2 - \frac{\partial^2}{\partial z^2}\right)\phi_{Lk}(z) = 0 \tag{3.7}$$

This Laplace's equation has solutions in the form $\phi_{Lk}(z) = C_{Lk}e^{-kz}$, here C_{Lk} is an amplitude of potential in the 2D Fourier basis. The normal derivative of potential satisfies the following boundary condition: discontinuity of normal component of electric field at $z = 0$:

$$\epsilon_0\frac{\partial\phi}{\partial z}|_{z=0^+} - \epsilon_1\frac{\partial\phi}{\partial z}|_{z=0^-} = -\rho(\mathbf{r}_{//}, z=0) \tag{3.8}$$

We then write $\rho(\mathbf{r}_{||}, z=0)$ in the Fourier Bessel integral, which gives

$$\rho(\mathbf{r}_{||}, z=0) = \sum_L \int_0^\infty kdkN_{Lk}J_L(kr)e^{iL\theta} \tag{3.9}$$

here N_{Lk} is an amplitude of charge density in the Fourier basis. A combination with the Eq.3.8 yields:

$$(\epsilon_0 + \epsilon_1)k\phi_{Lk}(0) = N_{Lk} \tag{3.10}$$

And according to the Eq.3.4, we have

$$N_{Lk} = \frac{\sigma(\omega)}{i\omega} k^2 \phi_{Lk}(0) \tag{3.11}$$

Combining above two equations and substituting RPA conductivity of graphene , we can get the frequency corresponding to eigensolution of surface plasmon in graphene disk as:

$$\omega = \sqrt{\frac{e^2 E_F}{(\epsilon_0 + \epsilon_b)\pi\hbar^2} k} \tag{3.12}$$

Then we can expand plasmon charge density $\rho(\mathbf{r})$ and potential induced by plasmon $\phi(\mathbf{r})$ in the eigenbasis:

$$\rho(\mathbf{r}) = \sum_L \int_0^\infty k dk \rho_{Lk} J_L(kr) e^{iL\theta} \delta(z) \tag{3.13}$$

$$\phi(\mathbf{r}) = \sum_L \int_0^\infty k dk \phi_{Lk} J_L(kr) e^{-kz} e^{iL\theta} \tag{3.14}$$

here ρ_{Lk} has the physical meaning of an amplitude of the plasmon modes and ϕ_{Lk} is the amplitude of the potential at the surface of the disk. In addition, it is necessary to impose a boundary condition at the edge of the disk: we assume there is no net flux of charge across the boundary. Therefore, the radial component of the current density must vanish at the edge of the graphene disk which is,

$$(\hat{e}_r \cdot \mathbf{J}) \mid_{r=R} = -\sigma(\omega) \frac{d}{dr} \phi(\mathbf{r})|_{r=R} = 0 \tag{3.15}$$

where R is the radius of the finite graphene disk. Each plasmon eigenmode should satisfy this boundary condition. Then we get

$$\left. \frac{dJ_L(kr)}{dr} \right|_{r=R} = 0 \tag{3.16}$$

This equation determines a set of discrete k values, $k_{Lm} = \frac{\beta_{Lm}}{R}$. We can see that the wave vector is not continuous and depends on the two quantum numbers: L and m, where β_{Lm} is the root of the derivative of the Bessel function $J_L^{'}(x)$. L is the angular quantum number, which is related to the number of nodes at the wavefunction as

$k_{Lm}(\frac{1}{nm})$	$L=0$	$L=1$	$L=2$	$L=3$
$m=1$	0.01916	0.009206	0.01527	0.02101
$m=2$	0.03508	0.02665	0.03353	0.04007
$m=3$	0.05086	0.04268	0.04984	0.5673
$m=4$	0.06661	0.05853	0.06585	0.07293
$m=5$	0.06661	0.07431	0.08173	0.08894

Table 3.1: Values of $k_{Lm} = \frac{\beta_{lm}}{R}$ of the angular and radial quantum number L and m, respectively.

the polar angle is varied, while m is the radial angular number which is related to the number of radial nodes in the wavefunction. In Table 3.1, we summarize values of β_{Lm} for the different angular and the radial quantum numbers.

Due to the wavevectors are discrete, the integral in Eq.3.13 should be replaced by a sum. We notice that by replacing the argument of the Bessel function in Eq.3.13 $J_L(kr)$ becomes $J_L\left(\frac{\beta_{Lm}}{R}r\right)$. The orthogonality and normalization of the Bessel functions on the interval [0,R] can be written as (see Arfeken'book [68] Page 697)

$$\int_0^R J_L\left(\frac{\beta_{Lm}}{R}r\right) J_L\left(\frac{\beta_{Ln}}{R}r\right) rdr = \frac{R^2}{2}\frac{\beta_{Lm}^2 - L^2}{\beta_{Lm}^2}[J_L(\beta_{Lm})]^2\delta_{mn} \tag{3.17}$$

Supplemented by the angular ket orthogonality:

$$\int_0^{2\pi} d\theta e^{i(L-L')\theta} = 2\pi\delta_{LL'} \tag{3.18}$$

According to the normalization of the Charge density:

$$\int_0^R rdr \int_0^{2\pi} d\theta\rho(\mathbf{r})^+\rho(\mathbf{r}) = 2\pi R^2 \sum_{Lm} \rho_{Lm}^+\rho_{Lm} \tag{3.19}$$

Then the charge density can be expanded in a Bessel series for $r \leqslant R$

$$\rho(\mathbf{r}) = \sum_{Lm} \sqrt{\frac{2\beta_{Lm}^2}{(\beta_{Lm}^2 - L^2)[J_L(\beta_{Lm})]^2}}\rho_{Lm} J_L\left(\frac{\beta_{Lm}}{R}r\right) e^{iL\theta}\delta(z) \tag{3.20}$$

The potential within the same radial interval $r \leqslant R$ has the form:

$$\phi(\mathbf{r}) = \sum_{Lm} \sqrt{\frac{2\beta_{Lm}^2}{(\beta_{Lm}^2 - L^2)[J_L(\beta_{Lm})]^2}} \phi_{Lm} J_L\left(\frac{\beta_{Lm}}{R} r\right) e^{iL\theta} e^{-\frac{\beta_{Lm}}{R} z} \tag{3.21}$$

allowing to derive the relation:

$$\phi_{Lm} = \frac{1}{\epsilon_0 + \epsilon_b} \frac{\rho_{Lm}}{\beta_{Lm}/R} \tag{3.22}$$

Potential Inside and Outside of the Disk The general equation for the potential due to charge density $\rho(\mathbf{r})$ can be expressed as

$$\phi(\mathbf{r}) = \frac{2}{\epsilon_0 + \epsilon_1} \int_0^R r' dr' \int_0^{2\pi} d\theta' \frac{\rho(\mathbf{r}')}{|\mathbf{r} - \mathbf{r}'|}. \tag{3.23}$$

According to Eq.3.15, the boundary condition for the potential is

$$\frac{\partial}{\partial r} \phi_{in}(r, 0)|_{r=R} = 0 \tag{3.24}$$

To find the potential inside and outside the disk, we express the Green's function $G(\mathbf{r}, \mathbf{r}') = \frac{1}{|\mathbf{r}-\mathbf{r}'|}$ in the cylindrical coordinate.

Green's function $G(\mathbf{r}, \mathbf{r}') = \frac{1}{|\mathbf{r}-\mathbf{r}'|}$ satisfies:

$$\nabla^2 G(\mathbf{r}, \mathbf{r}') = -\frac{\delta(r - r')\delta(\theta - \theta')\delta(z - z')}{r} \tag{3.25}$$

We expand the Green's function in the cylindrical coordinates [69]

$$G(r, r') = \frac{1}{2\pi^2} \sum_m \int_0^\infty dk e^{iL(\theta - \theta')} cos[k(z - z')] g_L(k, r, r') \tag{3.26}$$

Substitution into Eq.3.25, one gets the equation for the radial Green's function $g_m(k, r, r')$:

$$\frac{1}{r}\frac{d}{dr}\left(r\frac{dg_L}{dr}\right) - (k^2 + \frac{L^2}{r^2}) g_L = -\frac{1}{r}\delta(r - r') \tag{3.27}$$

For $r \neq r'$, the solution is a modified Bessel function, $I_L(kr)$ and $K_L(kr)$. The symmetry of the Green's function requires

$$g_L(k, r, r') = g_1(kr_<) g_2(kr_>) \tag{3.28}$$

Here $r_<$ and $r_>$ are the smaller and larger of r and r'. The discontinuity at $r = r'$ results in:

$$\left.\frac{dg_L}{dr}\right|_{r=r'-0} - \left.\frac{dg_L}{dr}\right|_{r=r'+0} = -\frac{1}{r'} \tag{3.29}$$

Since the potential $\phi(r)$ is finite at the center of disk, for $0 < r < r' < R$, we have a general solution for the Green's function in the form [69]

$$g_L^<(k, r, r') = AI_L(kr)g_2(kr') \tag{3.30}$$

and for $R_1 > r > r'$, we have

$$g_L^>(k, r, r') = (I_L(kr) + BK_L(kr))g_1(kr') \tag{3.31}$$

Substituting above two equations into Eq.3.29, we get

$$(I_L^{'}(kr') + BK_L^{'}(kr'))g_1(kr') - AI_L^{'}(kr')g_2(kr') = -\frac{1}{kr'} \tag{3.32}$$

Bessel functions have simple Wronskians [69]:

$$W[I_L(kr'), K_L(kr')] = -\frac{1}{kr'} \tag{3.33}$$

Comparison of the two above equations leads one to conclude that

$$Bg_1(kr') = I_L(kr') \tag{3.34}$$

$$Ag_2(kr') - g_1(kr') = K_L(kr') \tag{3.35}$$

We can write

$$g_L^{in}(r, r') = \left(K_L(kr_>) + \frac{I_L(kr_>)}{B}\right) I_L(kr_<) \tag{3.36}$$

Due to the boundary condition for the potential (Eq.3.24), we get

$$\frac{\partial g_L(k, r', r)}{\partial r}|_{r=R} = 0 \tag{3.37}$$

which is satisfied if either $I_L(kr') = 0$ (trivial solution) or the coefficient B equals:

$$B = -\frac{\frac{dI_L(kr)}{dr}}{\frac{dK_L(kr)}{dr}}|_{r=R} \tag{3.38}$$

Then the Green's function is given by

$$g_L(r,r') = \left(K_L(kr_>) - I_L(kr_>)\frac{K_L^{'}(kR)}{I_L^{'}(kR)} \right) I_L(kr_<) \tag{3.39}$$

Then we consider r' inside and r outside of the disk. For $0 < r' < R_1 < r$, the Green's function can be determined as

$$g_L(r' < R_1 < r) = \left(I_L(kr) + DK_L(kr) \right) I_L(kr') \tag{3.40}$$

Due to the boundary condition of the potential (Eq.3.24), the radial Green's function satisfies:

$$\left. \frac{\partial g_L(k,r',r)}{\partial r} \right|_{r=R} = 0 \tag{3.41}$$

We can determine the coefficient D.

$$D = -\frac{\frac{dI_L(k'r)}{dr}}{\frac{dK_L(k'r)}{dr}}|_{r=R} \tag{3.42}$$

The full solutions of the Green's function are expressed as:

$$g_L(r,r') = \begin{cases} \left(K_L(kr_>) - I_L(kr_>)\frac{K_L^{'}(kR)}{I_L^{'}(kR)} \right) I_L(kr_<), & r', r < R, \\ \left(I_L(kr) - \frac{I_L^{'}(kR)}{K_L^{'}(kR)} K_L(kr) \right) I_L(kr'), & r' < R < r \end{cases}$$

Potential inside and outside of the nanodisk can be written as:

$$\begin{aligned} & \phi^{inside}(\mathbf{r}) = \frac{2}{\epsilon_0 + \epsilon_b} \int_0^r \int_0^{2\pi} \rho(r') G^{r>r'}(r,r') r' dr' d\theta' \\ + \quad & \frac{2}{\epsilon_0 + \epsilon_b} \int_r^R \int_0^{2\pi} \rho(r') G^{r<r'}(r,r') r' dr' d\theta' \\ = \quad & \frac{1}{2\pi^2} \frac{2}{\epsilon_0 + \epsilon_b} \sum_{L'Lm} \sqrt{\frac{2\beta_{Lm}^2}{(\beta_{Lm}^2 - L^2)[J_L(\beta_{Lm})]^2}} \int_0^{2\pi} e^{i(L-L')\theta'} d\theta' \int_0^r \rho_{Lm} J_L \left(\beta_{Lm} \frac{r'}{R} \right) \\ \times \quad & \int_0^\infty dk g_L(r' < r < R) e^{iL'\theta} \cos[k(z-z')] r' dr' \\ + \quad & \frac{1}{2\pi^2} \frac{2}{\epsilon_0 + \epsilon_b} \sum_{L'Lm} \sqrt{\frac{2\beta_{Lm}^2}{(\beta_{Lm}^2 - L^2)[J_L(\beta_{Lm})]^2}} \int_0^{2\pi} e^{i(L-L')\theta'} d\theta' \int_r^R \rho_{Lm} J_L \left(\beta_{Lm} \frac{r'}{R} \right) \\ \times \quad & \int_0^\infty dk g_L(k, r < r' < R) e^{iL'\theta} \cos[k(z-z')] r' dr' \end{aligned} \tag{3.43}$$

We use the following equations:

$$\begin{aligned}
&\int_0^r r'dr' I_L(kr') J_L\left(\beta_{Lm}\frac{r'}{R}\right) \\
&= \frac{r\left(kI_{L+1}(kr)J_L\left(\beta_{Lm}\frac{r}{R}\right)+\beta_{Lm}/RI_L(kr)J_{L+1}\left(\beta_{Lm}\frac{r}{R}\right)\right)}{k^2+(\beta_{Lm}/R)^2}
\end{aligned} \tag{3.44}$$

$$\begin{aligned}
&\int_r^R r'dr' K_L(kr') J_L\left(\beta_{Lm}\frac{r'}{R}\right) \\
&= \frac{-\beta_{Lm}/RrJ_{L+1}\left(\beta_{Lm}\frac{r}{R}\right)K_L(kr)+\beta_{Lm}J_{L+1}(\beta_{Lm})K_L(kR)}{k^2+(\beta_{Lm}/R)^2} \\
&+ \frac{krJ_L\left(\beta_{Lm}\frac{r}{R}\right)K_{L+1}(kr)-kRJ_L(\beta_{Lm})K_{L+1}(kR)}{k^2+(\beta_{Lm}/R)^2}
\end{aligned} \tag{3.45}$$

$$\begin{aligned}
&\int_r^R r'dr' I_L(kr') J_L\left(\beta_{Lm}\frac{r'}{R}\right) \\
&= \frac{-\beta_{Lm}/RrJ_{L+1}\left(\beta_{Lm}\frac{r}{R}\right)I_L(kr)+\beta_{Lm}J_{L+1}(\beta_{Lm})I_L(kR)}{k^2+(\beta_{Lm}/R)^2} \\
&+ \frac{-krJ_L\left(\beta_{Lm}\frac{r}{R}\right)I_{L+1}(kr)+kRJ_L(\beta_{Lm})I_{L+1}(kR)}{k^2+(\beta_{Lm}/R)^2}
\end{aligned} \tag{3.46}$$

$$I_{L+1}(kR) = \left.\frac{dI_L(kr)}{kdr}\right|_{r=R} - \frac{L}{kR}I_L(kR) \tag{3.47}$$

$$K_{L+1}(kR) = -\left.\frac{dK_L(kr)}{kdr}\right|_{r=R} + \frac{L}{kR}K_L(kR) \tag{3.48}$$

$$-\beta_{Lm}J_{L+1}(\beta_{Lm})/R + \frac{L}{R}J_L(\beta_{Lm}) = 0 \tag{3.49}$$

The potential inside of the nanodisk ($z' = 0$) is simplified to:

$$\begin{aligned}
\phi^{in}(\mathbf{r}) &= \frac{1}{\pi}\sum_{Lm}\sqrt{\frac{2\beta_{Lm}^2}{(\beta_{Lm}^2-L^2)[J_L(\beta_{Lm})]^2}}\frac{1}{\epsilon_0+\epsilon_b}J_L\left(\frac{\beta_{Lm}}{R}r\right)e^{iL\theta} \\
&\times \int_0^\infty \frac{2\cos[kz]}{k^2+(\beta_{Lm}/R)^2} \\
&= \sum_{Lm}\sqrt{\frac{2\beta_{Lm}^2}{(\beta_{Lm}^2-L^2)[J_L(\beta_{Lm})]^2}}\frac{1}{\epsilon_0+\epsilon_b}\frac{\rho_{Lm}}{\beta_{Lm}/R}J_L\left(\frac{\beta_{Lm}}{R}r\right)e^{iL\theta}e^{-\beta_{Lm}z/R}
\end{aligned} \tag{3.50}$$

And the potential outside of the disk is:

$$
\begin{aligned}
& \phi^{out}(r) = \frac{1}{2\pi^2}\int_0^R\int_0^{2\pi}\rho(r')G(r'<r<R)r'dr'd\theta' \\
= \;& \frac{1}{2\pi^2}\frac{2}{\epsilon_0+\epsilon_b}\sum_{L'Lm}\sqrt{\frac{2\beta_{Lm}^2}{(\beta_{Lm}^2-L^2)[J_L(\beta_{Lm})]^2}}\int_0^{2\pi}e^{i(L-L')\theta'}d\theta'\int_0^R\rho_{Lm}J_L(\beta_{Lm}\frac{r'}{R}) \\
\times \;& \int_0^\infty dk\left(I_L(kr)+DK_L(kr)\right)I_L(kr')e^{iL'\theta}\cos[k(z-z')]r'dr' \\
= \;& \frac{1}{\pi}\frac{2}{\epsilon_0+\epsilon_b}\sum_{Lm}\sqrt{\frac{2\beta_{Lm}^2}{(\beta_{Lm}^2-L^2)[J_L(\beta_{Lm})]^2}}\int_0^\infty dk\left(I_L(kr)-\frac{K_L'(kR)}{I_L'(kR)}K_L(kr)\right) \\
\times \;& \frac{RkI_{L+1}(kR)J_L(\beta_{Lm})+\beta_{Lm}I_L(kR)J_{L+1}(\beta_{Lm})}{k^2+(\beta_{Lm}/R)^2}\cos(kz) \\
= \;& \frac{1}{\pi}\frac{2}{\epsilon_0+\epsilon_b}\sum_{Lm}\sqrt{\frac{2\beta_{Lm}^2}{(\beta_{Lm}^2-L^2)[J_L(\beta_{Lm})]^2}}\int_0^\infty dk\left(I_L(kr)-\frac{K_L'(kR)}{I_L'(kR)}K_L(kr)\right) \\
\times \;& \frac{RJ_L(\beta_{Lm})I_L'(kR)}{k^2+(\beta_{Lm}/R)^2}\cos(kz) \qquad (3.51)
\end{aligned}
$$

We must notice that surface plasmon modes (Eq.3.52) in the graphene nanodisk possess a set of discrete frequencies whose magnitudes depend on the Fermi energy of graphene (as we discussed in the previous chapter via the magnitude of background charge density) as well as the size of the disk and the dielectric properties of the substrate (via the screening, although this factor is minimal in the experimental frequency range).

$$\omega_{Lm} = \sqrt{\frac{e^2E_F}{(\epsilon_0+\epsilon_b)\pi\hbar^2}\frac{\beta_{Lm}}{R}} \qquad (3.52)$$

The result for the eigenfrequencies is shown in Fig.3.2. Here we plot the plasmon frequencies for the angular momentum number L up to 6, and the radial quantum number up to 15. We clearly see that the frequencies of the surface plasmon modes in the finite disk increase with E_F due to the higher density of charge carriers which could induce high oscillation frequencies [70]. Reducing the size of the disk produces a higher carrier density due to the space quantitation. This illustrates strong tunability of plasmonic properties of graphene. The plasmon frequencies in

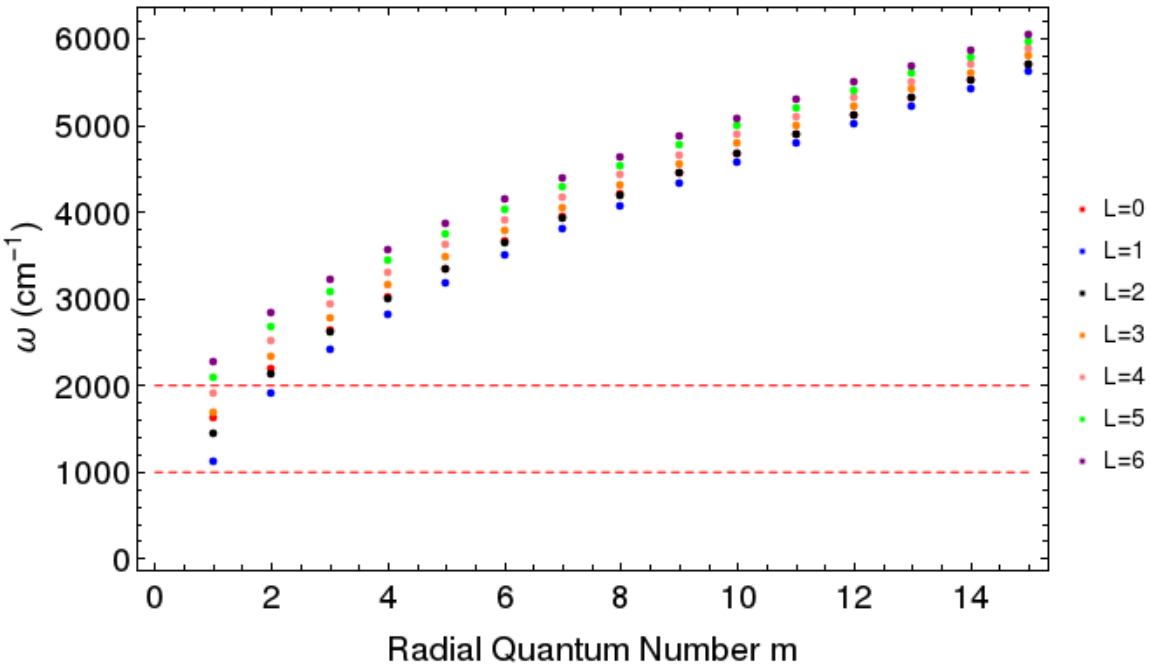

Figure 3.2: Resonant frequency of the modes calculated using the Eq.3.52. For each L, 15 discrete radial eigenmodes are shown. $R = 200nm$, $E_F = 0.3eV$.

the finite disk approaches dispersion relation for infinite graphene: $\beta_{Lm}/R \to q$, which indicates that the wavevector of plasmon modes in the finite disk can be described as β_{Lm}/R.

3.3 Response of Graphene nanodisk to an External Field

The charge density wavefunction has a central node (zero amplitude in the middle of the nanodisk) for $L \neq 0$. On the contrary, the experimental patterns show the central node even for the modes with clear angular dependence. The mechanism that causes this pattern symmetry breaking must be explored. One plausible model is that at a given frequency several plasmon modes can be excited simultaneously. Thus the combined response may include symmetry features of $L = 0$ and $L \neq 0$

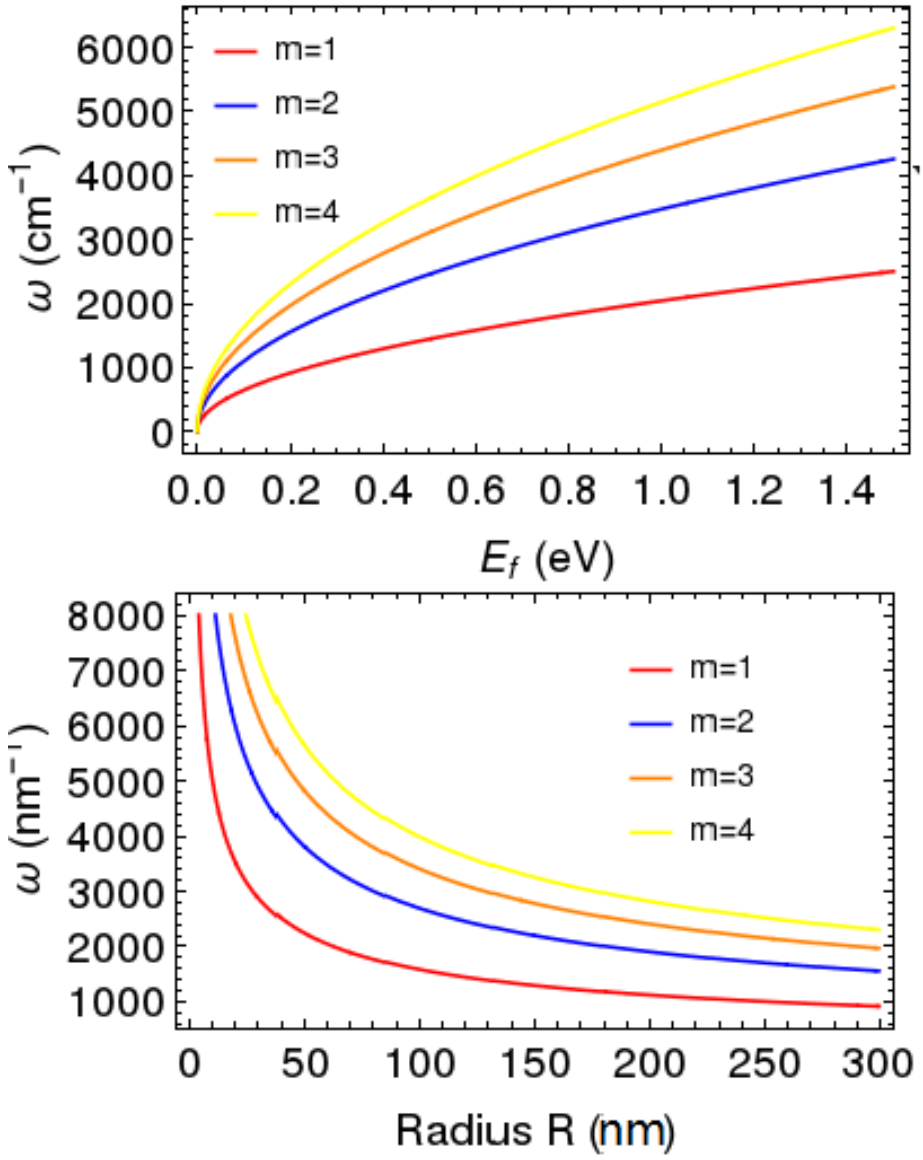

Figure 3.3: The frequency of the surface plasmons for angular momentum number $L = 1$ as a function of the Fermi Energy E_F (Top: $R = 200nm$) and the radius of the graphene disk (Bottom: $E_F = 0.3eV$). The first lowest radial quantum numbers modes are shown.

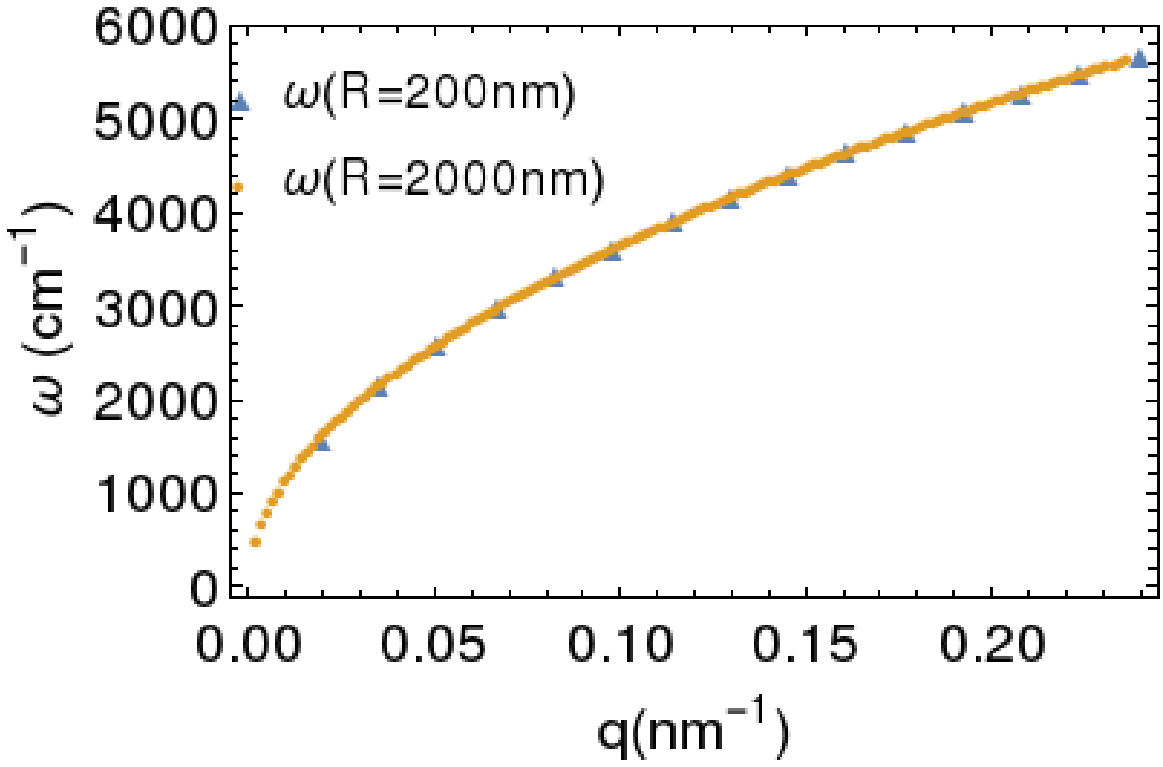

Figure 3.4: Eigenfrequencies of the surface plasmon in the finite disks with different radius are given for wave vector β_{Lm}/R, for $L = 1$, m up to 15.

modes. We use an analytic model to describe the interaction between a probe tip and the graphene nanodisk. The tip can be represented by a point dipole, as shown in Fig.3.6. This model is suitable for calculating the response of the graphene disk when the higher multipole components of the tip potential are negligible. The self-consistent potential due to the external dipole is given by:

$$\phi^{act} = \phi^{ext} + \phi^{ind} \tag{3.53}$$

This expression of Eq.3.53 is the sum of two contributions: the external perturbation ϕ^{ext} and the potential created by the charge in doped graphene under the external perturbation ϕ^{ind}.

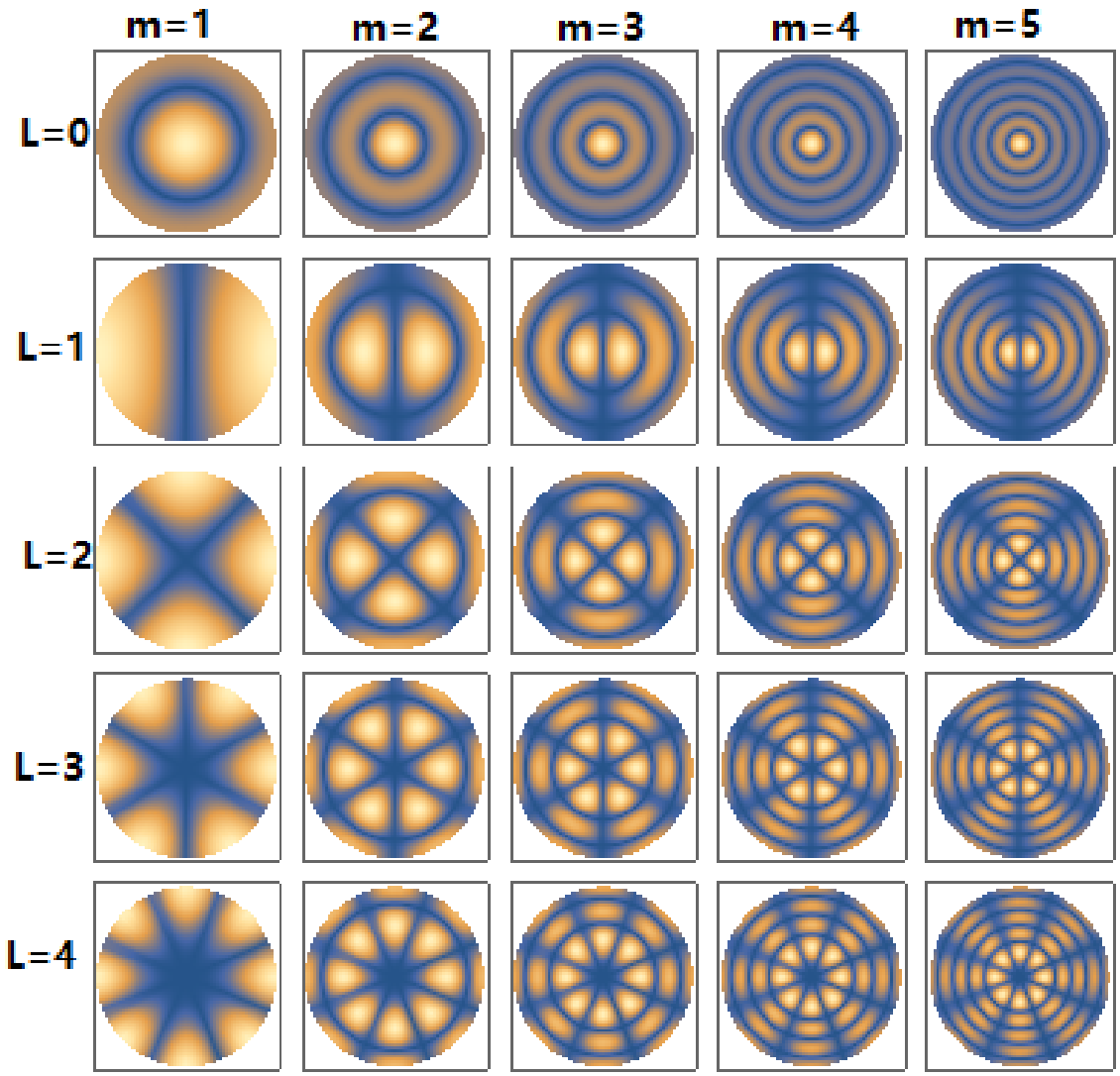

Figure 3.5: Wavefunction of charge density with 6 lowest radial quantum numbers and the angular quantum number up to 4, in the $x-y$ plane for the graphene disk with $R = 200nm$ and $E_F = 0.3eV$.

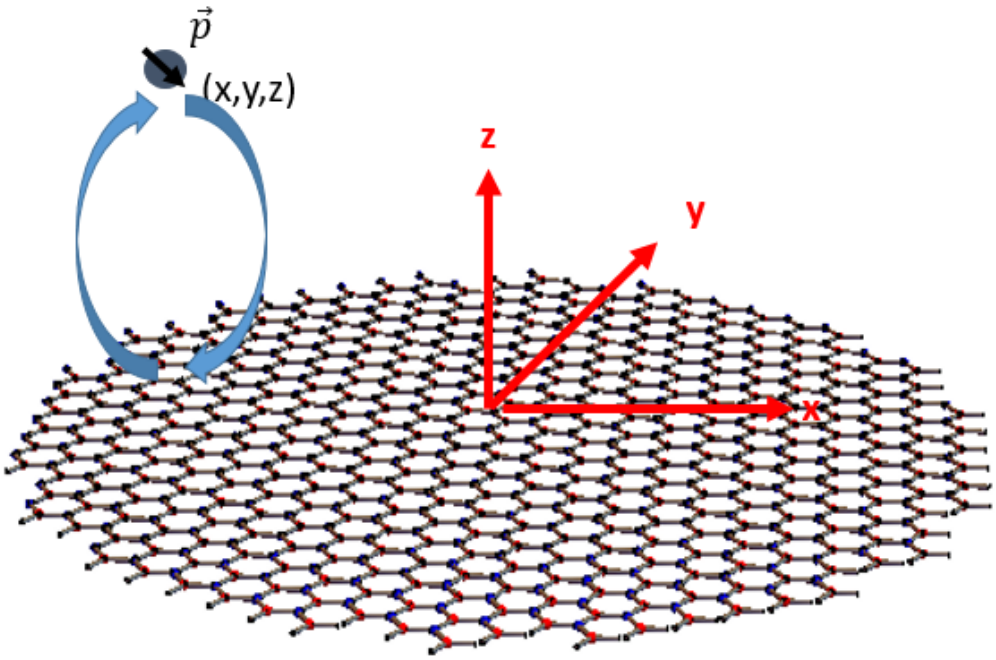

Figure 3.6: Schematic geometry under consideration. A dipole in the presence of the graphene nanodisk, the position of the dipole is (x, y, z).

According to Eq.3.21

$$\phi^{ind}(\mathbf{r}) = \sum_{Lm} \sqrt{\frac{2\beta_{Lm}^2}{(\beta_{Lm}^2 - L^2)[J_L(\beta_{Lm})]^2}} \phi_{Lm}^{ind} J_L\left(\frac{\beta_{Lm}}{R} r\right) e^{iL\theta} e^{-\frac{\beta_{Lm}}{R} z} \tag{3.54}$$

Here we can express $\phi_{act}(\mathbf{r})$ in the Fourier Bessel integral,

$$\phi_{act}(\mathbf{r}) = \sum_{L} \int_0^\infty k dk \phi_L^{act}(k) J_L(kr) e^{iL\theta} e^{-kz} \tag{3.55}$$

According to normalization equation:

$$\int d^2\mathbf{r} \rho^+(\mathbf{r}) \phi^{act}(\mathbf{r}) = 2\pi R^2 \sum_{Lm} \rho_{Lm}^+ \phi_{Lm}^{act} \tag{3.56}$$

We can get:

$$\phi_{Lm}^{act} = \sqrt{\frac{2\beta_{Lm}^2}{(\beta_{Lm}^2 - L^2)[J_L(\beta_{Lm})]^2}} \frac{1}{2\pi R^2} \int_0^R r dr \int_0^{2\pi} e^{-iL\theta} d\theta J_L\left(\frac{\beta_{Lm}}{R} r\right) \phi_{act}(r, 0) \tag{3.57}$$

And according to Eq.3.3, we get

$$\begin{aligned}
\rho_{Lm} &= \frac{\sigma(\omega)}{i\omega}\left(\nabla_{||}^2\phi^{ind}+\nabla_{||}^2\phi^{ext}\right)_{Lm} \\
&= \frac{\sigma(\omega)}{i\omega}\left(\frac{\beta_{Lm}}{R}\right)^2\frac{1}{\epsilon_0+\epsilon_b}\frac{\rho_{Lm}}{\beta_{Lm}/R} \\
&+ \frac{\sigma(\omega)}{i\omega}\sqrt{\frac{2\beta_{Lm}^2}{(\beta_{Lm}^2-L^2)[J_L(\beta_{Lm})]^2}}\frac{1}{2\pi R^2}\int d^2\mathbf{r}_{||}e^{-iL\theta}J_L\left(\frac{\beta_{Lm}}{R}r\right)\nabla_{||}^2\phi^{ext}(\mathbf{r})
\end{aligned} \tag{3.58}$$

The differential operator is given by:

$$\nabla_{||}^2 = \frac{1}{r}\frac{\partial}{\partial r}r\frac{\partial}{\partial r}+\frac{1}{r^2}\frac{\partial^2}{\partial\theta^2} \tag{3.59}$$

Then we have

$$\begin{aligned}
&\int_0^R\int_0^{2\pi} rdrd\theta e^{-iL\theta}J_L\left(\frac{\beta_{Lm}}{R}r\right)\frac{1}{r}\frac{\partial}{\partial r}r\frac{\partial}{\partial r}\phi^{ext}(\mathbf{r}) \\
= &\int_0^{2\pi} e^{-iL\theta}\left\{J_L\left(\frac{\beta_{Lm}}{R}r\right)r\frac{\partial}{\partial r}\phi^{ext}(\mathbf{r})|_0^R-\int_0^R\frac{d}{dr}J_L\left(\frac{\beta_{Lm}}{R}r\right)r\frac{\partial}{\partial r}\phi^{ext}(\mathbf{r})\right\}d\theta \\
= &\int_0^{2\pi} e^{-iL\theta}\left\{J_L\left(\frac{\beta_{Lm}}{R}r\right)r\frac{\partial}{\partial r}\phi^{ext}(\mathbf{r})|_0^R-r\frac{d}{dr}J_L\left(\frac{\beta_{Lm}}{R}r\right)\phi^{ext}(\mathbf{r})|_0^R\right. \\
+ &\left.\int_0^R\frac{1}{r}\frac{d}{dr}r\frac{d}{dr}J_L\left(\frac{\beta_{Lm}}{R}r\right)\phi^{ext}(\mathbf{r})rdr\right\}d\theta \\
= &J_L(\beta_{Lm})R\int_0^{2\pi}e^{-iL\theta}\frac{\partial}{\partial r}\phi^{ext}(\mathbf{r})|_0^R \\
+ &\int_0^{2\pi}e^{-iL\theta}\int_0^R\frac{1}{r}\frac{d}{dr}r\frac{d}{dr}J_L\left(\frac{\beta_{Lm}}{R}r\right)\phi^{ext}(\mathbf{r})rdrd\theta
\end{aligned} \tag{3.60}$$

and

$$\begin{aligned}
&\int_0^R\int_0^{2\pi} rdrd\theta e^{-iL\theta}J_L\left(\frac{\beta_{Lm}}{R}r\right)\frac{1}{r^2}\frac{\partial^2}{\partial\theta^2}\phi^{ext}(\mathbf{r}) \\
= &\int_0^{2\pi}\frac{1}{r^2}\frac{\partial^2}{\partial\theta^2}e^{-iL\theta}\int_0^R J_L\left(\frac{\beta_{Lm}}{R}r\right)\phi^{ext}(\mathbf{r})rdrd\theta
\end{aligned} \tag{3.61}$$

From above equations, we get

$$\begin{aligned}
&\int d^2\mathbf{r}_{||}e^{-iL\theta}J_L\left(\frac{\beta_{Lm}}{R}r\right)\nabla_{||}^2\phi^{ext}(\mathbf{r}) = J_L(\beta_{Lm})R\int_0^{2\pi}e^{-iL\theta}\frac{\partial}{\partial r}\phi^{ext}(\mathbf{r})|_0^R \\
+ &\int d^2\mathbf{r}_{||}e^{-iL\theta}\nabla_{||}^2J_L\left(\frac{\beta_{Lm}}{R}r\right)\phi^{ext}(\mathbf{r})
\end{aligned} \tag{3.62}$$

since

$$\begin{aligned}\nabla^2_{||} J_L(kr) &= k^2 J_L^{''}(kr) + \frac{k}{r} J_L^{'}(kr) - \frac{L^2}{r^2} J_L(kr) \\ &= k^2 \left(J_L^{''}(kr) + \frac{1}{kr} J_L^{'}(kr) - \frac{L^2}{(kr)^2} J_L(kr) \right) \\ &= -k^2 J_L(kr) \end{aligned} \tag{3.63}$$

Then Eq.3.58 becomes:

$$\begin{aligned}\rho_{Lm} &= \frac{\sigma(\omega)}{i\omega} \left(\frac{\beta_{Lm}}{R} \right)^2 \frac{1}{\epsilon_0 + \epsilon_b} \frac{\rho_{Lm}}{\beta_{Lm}/R} \\ &+ \frac{\sigma(\omega)}{i\omega} \sqrt{\frac{2\beta^2_{Lm}}{(\beta^2_{Lm} - L^2)}} \frac{1}{2\pi R} \int_0^{2\pi} e^{-iL\theta} \frac{\partial}{\partial R} \phi^{ext}(\mathbf{R}) \\ &+ \frac{\sigma(\omega)}{i\omega} \sqrt{\frac{2\beta^2_{Lm}}{(\beta^2_{Lm} - L^2)[J_L(\beta_{Lm})]^2}} \frac{1}{2\pi R^2} \int d^2\mathbf{r}_{||} e^{-iL\theta} J_L \left(\frac{\beta_{Lm}}{R} r \right) \phi^{ext}(\mathbf{r}) \end{aligned} \tag{3.64}$$

The potential created by a dipole source positioned at $\mathbf{r}' = (r', y', z')$ with a dipole moment $\mathbf{p}$ is given by

$$\phi^{ext}(\mathbf{r}) = \mathbf{p}\delta(\mathbf{r}') \cdot \nabla_{\mathbf{r}'} \frac{1}{|\mathbf{r}' - \mathbf{r}|} \tag{3.65}$$

The monopole Green's function can be expressed as a Fourier-Bessel integral [69]

$$G(\mathbf{r}, \mathbf{r}') = \frac{1}{|\mathbf{r}' - \mathbf{r}|} = \sum_L \int_0^\infty dk e^{iL(\theta - \theta')} J_L(kr) J_L(kr') e^{-k(z'-z)} \tag{3.66}$$

here

$$\int_0^\infty dk J_L(kr) J_L(kr') e^{-kz'} = \frac{1}{\pi\sqrt{rr'}} Q_{L-\frac{1}{2}}(\frac{z'^2 + r^2 + (r')^2}{2rr'}) \tag{3.67}$$

where $Q_L(x)$ is the Legendre function of the second kind, we define $\nabla G_{\mathbf{rr}'} = \nabla \frac{1}{|\mathbf{r}' - \mathbf{r}|}$, and ∇G_{Lm} is its form in the Fourier space,

$$\nabla G_{Lm} = \frac{1}{2\pi R^2} \sqrt{\frac{2\beta^2_{Lm}}{(\beta^2_{Lm} - L^2)[J_L(\beta_{Lm})]^2}} \int_0^R r dr \int_0^{2\pi} d\theta \nabla \frac{1}{|\mathbf{r}' - \mathbf{r}|} e^{-iL\theta} J_L \left(\frac{\beta_{Lm}}{R} r \right) \tag{3.68}$$

Combining all the former elements, we rearrange the Eq.3.58:

$$\rho_{Lm} = \frac{\omega_{Lm}^2}{\omega^2 - \omega_{Lm}^2} \frac{(\epsilon_0 + \epsilon_b)R}{\beta_{Lm}} (\nabla G_{Lm} + \nabla g_L) \cdot \mathbf{p} \tag{3.69}$$

here we define $\nabla g_L = R\sqrt{\frac{2\beta_{Lm}^2}{(\beta_{Lm}^2 - L^2)}} \nabla_{\mathbf{r}'} \int_0^{2\pi} e^{-iL\theta} \frac{\partial}{\partial r} \frac{1}{|\mathbf{r}-\mathbf{r}'|} \Big|_{r=R}$.

If we assume the dipole has an amplitude p_0 and consider the case for which the dipole is along the x and z axis. The electric field of graphene at the position of $\mathbf{r}$ has the form

$$\begin{aligned} \mathbf{E}(\mathbf{r}) &= -\nabla \int_0^R \int_0^{2\pi} \frac{\rho(r')}{|\mathbf{r} - \mathbf{r}'|} r' dr' d\theta \\ &= \sum_{Lm} \sqrt{\frac{2\beta_{Lm}^2}{(\beta_{Lm}^2 - L^2)[J_L(\beta_{Lm})]^2}} \rho_{Lm} \nabla \int_0^R \int_0^{2\pi} \frac{J_L(\frac{\beta_{Lm}}{R} r') e^{iL\theta'}}{|\mathbf{r} - \mathbf{r}'|} r' dr' d\theta \\ &= \hat{\alpha}\mathbf{p} \end{aligned} \tag{3.70}$$

Here α is the graphene response function tensor to the external dipole:

$$\hat{\alpha} = 2\pi R^2 \sum_{Lm} \frac{\omega_{Lm}^2}{\omega^2 - \omega_{Lm}^2} \frac{(\epsilon_0 + \epsilon_b)R}{\beta_{Lm}} (\nabla G_{Lm} + \nabla g_L) \bigotimes \nabla G_{Lm}^* \tag{3.71}$$

3.4 Results and Discussions

In experiments the excitation source allowed to probe the surface plasmons in the frequency range of $1000cm^{-1}$ to $2000cm^{-1}$. If we choose $E_F = 0.3$eV and other parameters $R = 200nm$, $\epsilon_b = 1.6$, then from Fig.3.2, 6 plasmon modes exist within this frequency range, which are $Lm = 01, 11, 12, 21, 31, 41$ modes. A constant linewidth of plasmon modes is assumed henceforth in the calculation: $\gamma_{sp} = 20cm^{-1}$.

3.4.1 Response Function to the external Dipole

To make better connection to experimental results, we calculate the response function of the disk plasmon to the field of the external dipole. We begin with considering that the dipole is placed at the middle or at the edge of the graphene nanodisk, and investigate the frequency dependence of the real and imaginary part of the response

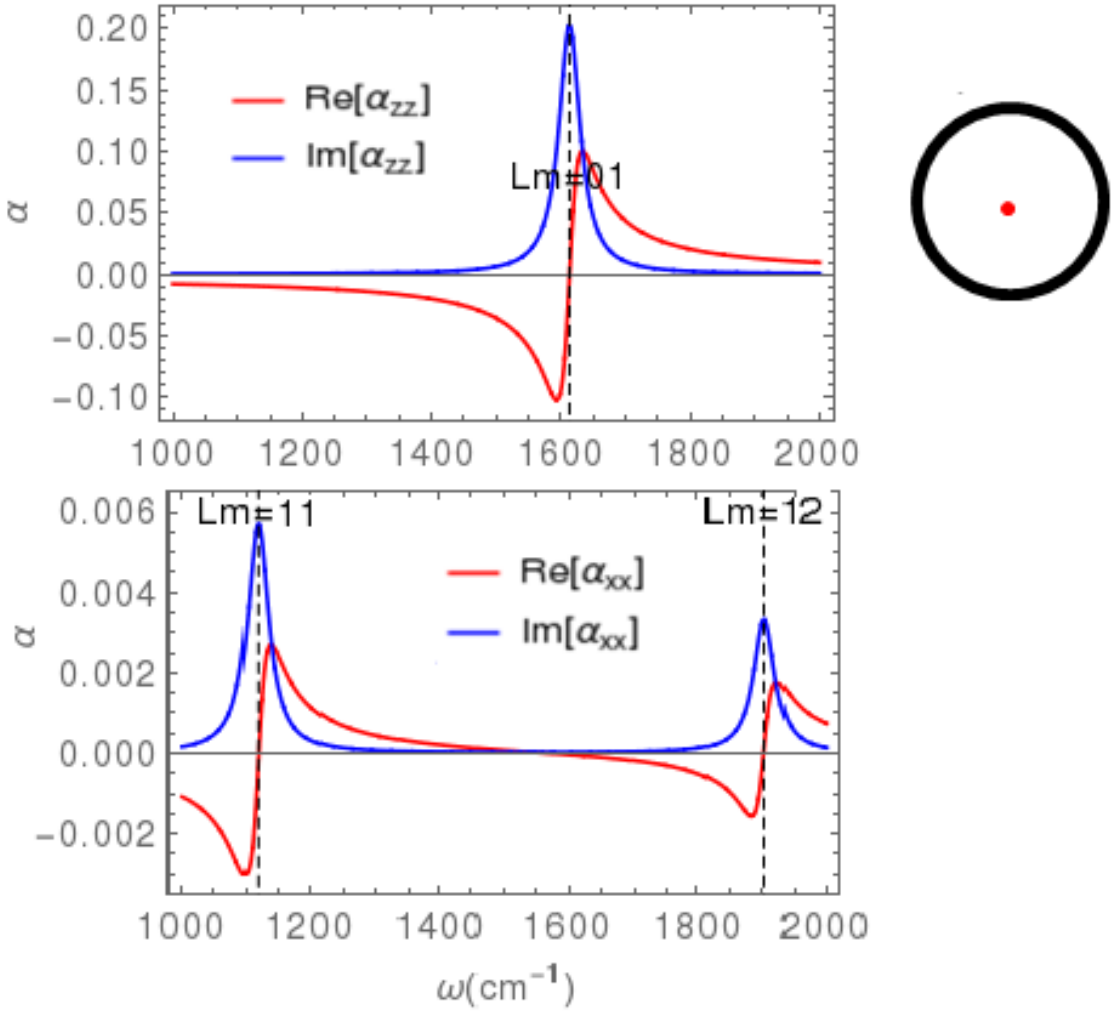

Figure 3.7: Frequency dependence of the real part and the imaginary part of the response function for the graphene nanodisk to a z-oriented(top) and a x-oriented (bottom) dipole located at $\mathbf{r} = (0, 0, 30nm)$.

function components. If the laser beam has a incidence angle, the polarization of the tip is largest in the vertical (z) direction. In some other experimental geometry this condition may not hold, thus we also consider the x-polarization model. In general case, the dipole of the tip may have all 3 components, depending on the full geometry to the setup.

We consider two different dipole orientations: x and z. Resonance frequencies in the Fig.3.7 depend on polarization: $zz(xx)$ component of the response function corresponds to the case when the dipole moment and the electric field component of graphene are both along the z(x) axis. In Fig.3.7, when the dipole is in the z direction and placed in the center of the disk, the response function contains the single $L = 0, m = 1$ resonance peak, corresponding to the full symmetric $L = 0$ plasmon mode. When the dipole is in the x direction, the plasmon modes with the $L = 1$ contribute to the response function. One can visualize this by plotting the field of the dipole placed at the center of the disk: the **z**-oriented dipole induces a full axial symmetric field on the graphene plane while the **x**-oriented one induces a asymmetric field along **x** axis on the plane as shown in Fig.3.8 of the field created by the **z**-oriented and **x**-oriented dipole. Furthermore, as seen from Fig3.7, the excitation of the surface plasmons is more efficient if the external dipole is normal to the graphene nanodisk. If the dipole is placed off the center of the disk, such as at $\mathbf{r} = (200nm, 0nm, 30nm)$ in Fig.3.9, the zz component (Top) and xx component (Bottom) of the response function both show the multiple L resonances due to the external potential does not have the rotational symmetry is broken. When the dipole frequency is close to the lowest (fully symmetric) plasmon: $\omega = \omega_{01} + 20eV$, several plasmon modes with the angular momentum $L = 0, 2, 3$ can be excited non-resonantly due to the finite spectral overlap of the peaks of the modes with excitation frequency.

Fig.3.10 and Fig.3.11 present the density plot of the imaginary part of the zz component response function, when the dipole is placed at a fixed z position ($z = 30nm$) and scans over the xy plane. Strong plasmonic response of the graphene disk is achieved when the frequencies of the field have been chosen (from Fig.3.9) around the peak resonance values, such as $\omega = \omega_{Lm} + 20eV$. Fig.3.10(Top) alos shows the case of frequency below $L = 0$, $m = 1$ mode, at $\omega = \omega_{01} - 20cm^{-1}$. We observe a 6-fold symmetry, a central peak and also a 2-fold symmetry, which is similar to the experimental pattern. The pattern can be clearly seen from 3D-plot. At this frequency, obviously several plasmon modes with the angular momentum $L = 0, 2, 3$

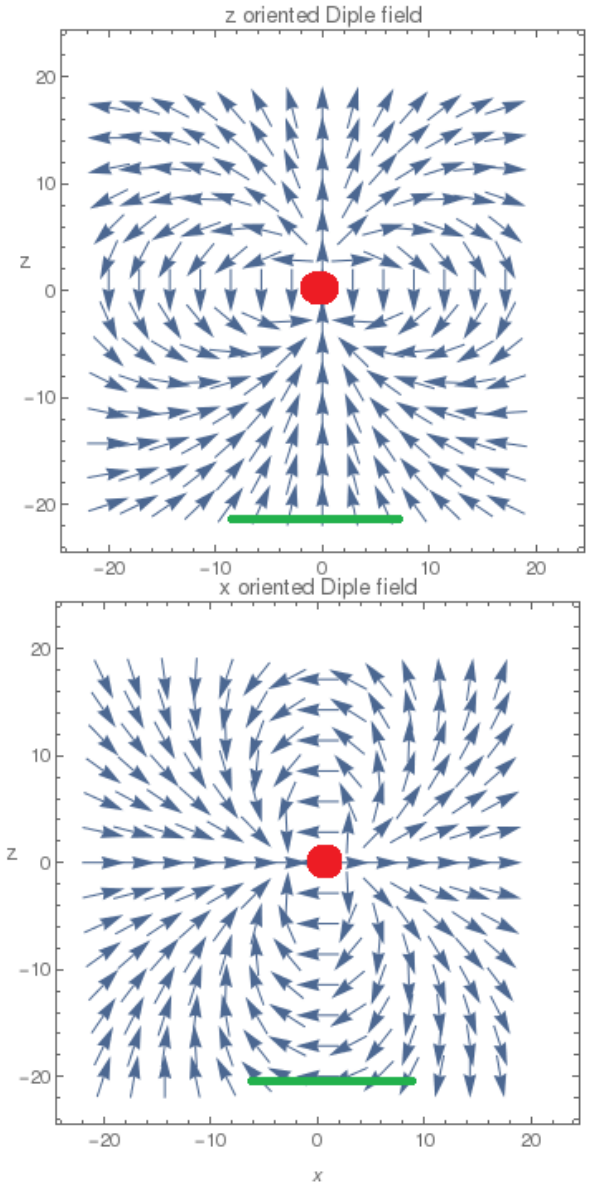

Figure 3.8: Field of the z-oriented and x-oriented dipole. The red dot represents the dipole position, the blue line represents the graphene nanodisk plane

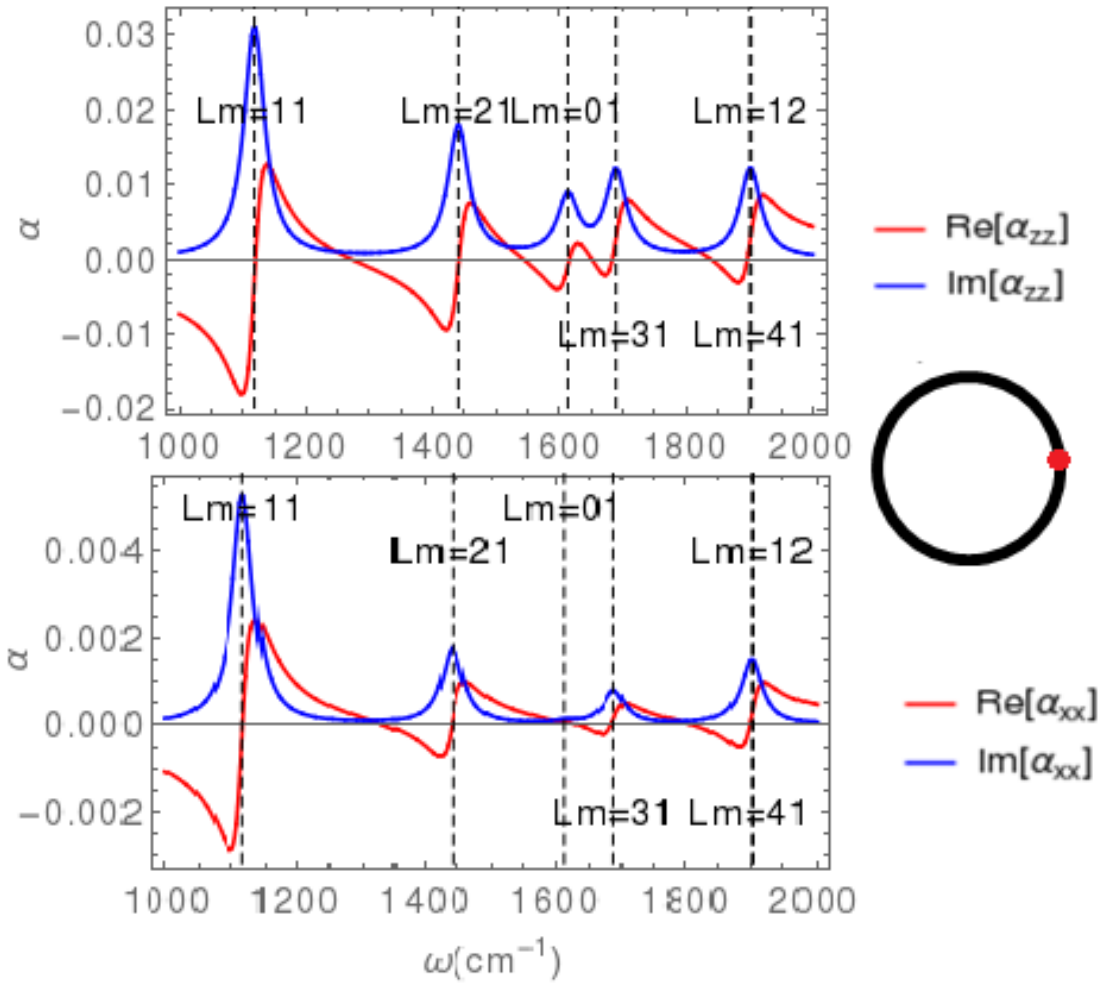

Figure 3.9: Frequency dependence of the real part and the imaginary part of response function for the graphene nanodisk to a z-oriented (top) and a x-oriented (bottom) dipole located at the fixed position $\mathbf{r} = (200nm, 0, 30nm)$.

can be excited. The strong central peak in Fig.3.9 is due to the plasmon mode with $L = 0$. When the frequency is above 01-mode at $\omega = \omega_{01} + 20cm^{-1}$ (Fig.3.10 Bottom), the 2-fold symmetry disappears, we only observe $L = 3, 0$ patterns. When the frequency is at $\omega = \omega_{11} + 20cm^{-1}$ (Fig.3.11 Top), we see a 2-fold symmetry

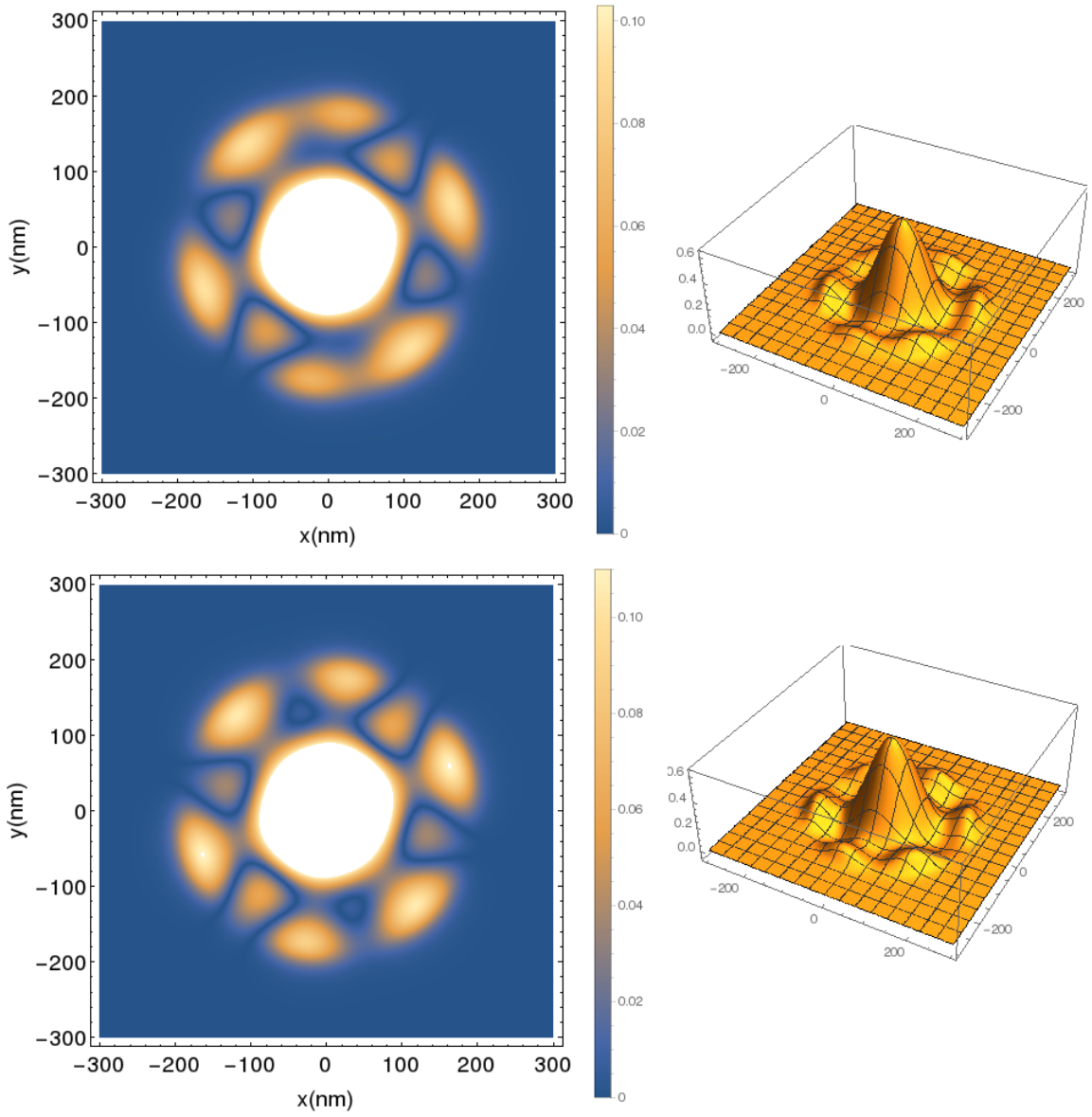

Figure 3.10: Absolute value (Left) and 3D map (Right) of the imaginary part of zz component response functions $|Im\alpha_z z|$ at frequency of $\omega = \omega_{01} - 20cm^{-1}$ (Top row) and $\omega = \omega_{01} + 20cm^{-1}$(Bottom row). Dipole is fixed at $z = 23nm$ position and scans in xy plane.

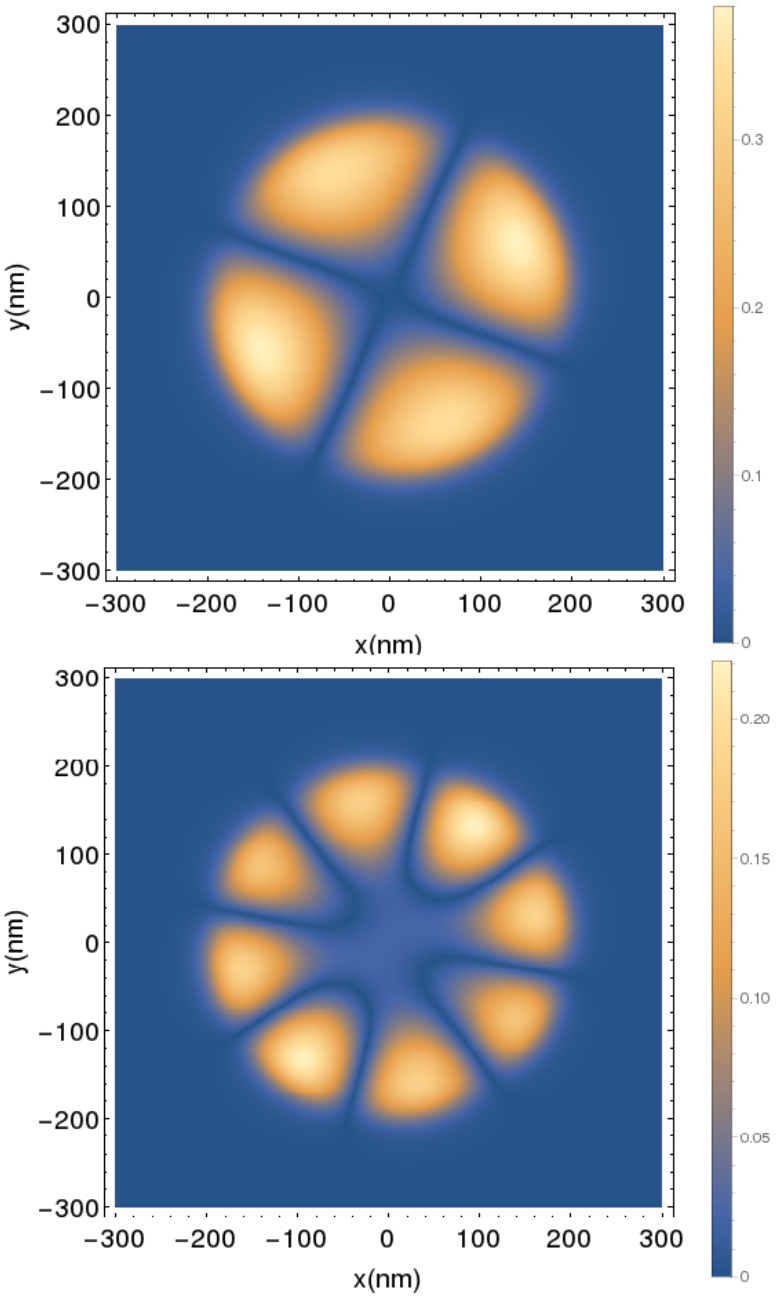

Figure 3.11: Absolute value of the imaginary part of zz component response functions at frequency of $\omega = \omega_{Lm} + 20cm^{-1}$ for (a)$Lm = 11$,(b)$Lm = 21$. Dipole is fixed at the z position and scans in the xy plane.

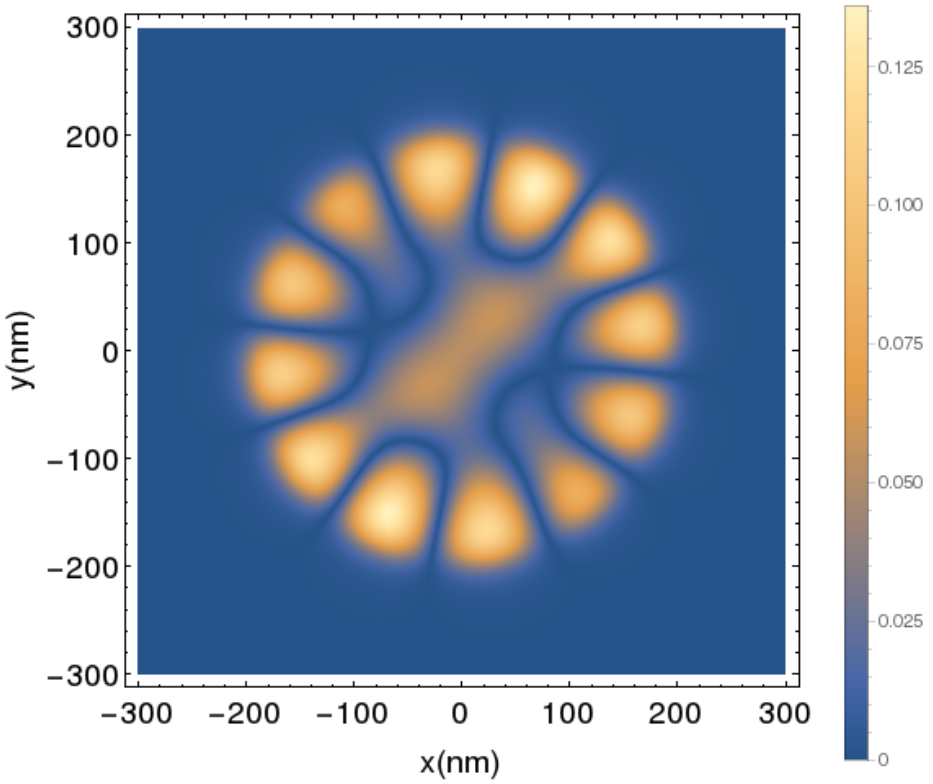

Figure 3.12: Absolute value of the imaginary part of zz component response functions at frequency of $\omega = \omega_{31} + 20cm^{-1}$. Dipole is fixed at z position and scans in xy plane.

pattern due to $L = 1$ and $L = 2$ plasmon modes in the graphene nanodisk that are excited at this frequency. When the frequency is at $\omega = \omega_{21} + 20cm^{-1}$ (Fig.3.11 Bottom), we observe a 4-fold symmetry. A weak $L = 0$ pattern is observed when the dipole frequency is at $\omega = \omega_{31} + 20cm^{-1}$. In Fig.3.12, we can see a 6-fold symmetry, $L = 0, 1$ patterns. High order symmetry is due to upper radial modes that may be excited.

3.4.2 Plasmon Wavefunctions Excited by the field of an External Dipole

Although calculation of a map of the tip response function provides more information about near-field plasmonic pattern, such a calculation is also more computationally expensive. Here we will analyze the wavefunction of plasmons Vs position of the excitation (dipole) source and its frequency. Such a calculation allows one to analyze spatial and spectral overlap of the sourse with plasmonic modes of the system. We plot the plasmon wavefunction (Eq.3.20) at the two fixed dipole positions $\mathbf{r} = (0, 0, 30)nm$(center) and $\mathbf{r} = (200, 0, 30)nm$(edge). When the dipole is along $\mathbf{x}$ in the center of the disk (Fig.3.13), only the $L = 1$ pattern (2 nodes in the angular direction) exists in the studied frequency range. While the dipole is along the $\mathbf{z}$ direction (Fig.3.14), we observe only $L = 0$ pattern (full circular), as the coupling to any other modes is forbidden by symmetry.

If the dipole is placed at the edge of the disk $\mathbf{r} = (200, 0, 30)nm$, external potential does not have rotational symmetry. In Fig.3.15 and Fig.3.16, the dipole is oriented along the $\mathbf{x}$ and $\mathbf{z}$ axis, respectively. For both orientations, we observe different patterns in the plasmon wavefunctions Vs the function of the frequency. At frequency $\omega = \omega_{01} + 20cm^{-1}$ in Fig.3.15(a) and Fig.3.16(a), we can see a hexagonal pattern with a central peak. This is because the multiple modes can be excited by the dipole at frequency $\omega = \omega_{01} + 20cm^{-1}$ when the rotational symmetry of the external field is broken by placing the dipole off the center. The plasmon mode with $L = 0$ has a strong contribution the total wave function shown in Fig.3.15(a) and Fig.3.16(a) due to the external dipole is in the strongest resonance with the eigenfrequency ω_{01} of the graphene plasmon mode $L = 0$. While for the external frequency $\omega = \omega_{31} + 20cm^{-1}$ in Fig.3.16(d), we can see a hexagonal symmetry with a weak central peak. The plasmon mode with $L = 3$ dominates the total wave function in this case.

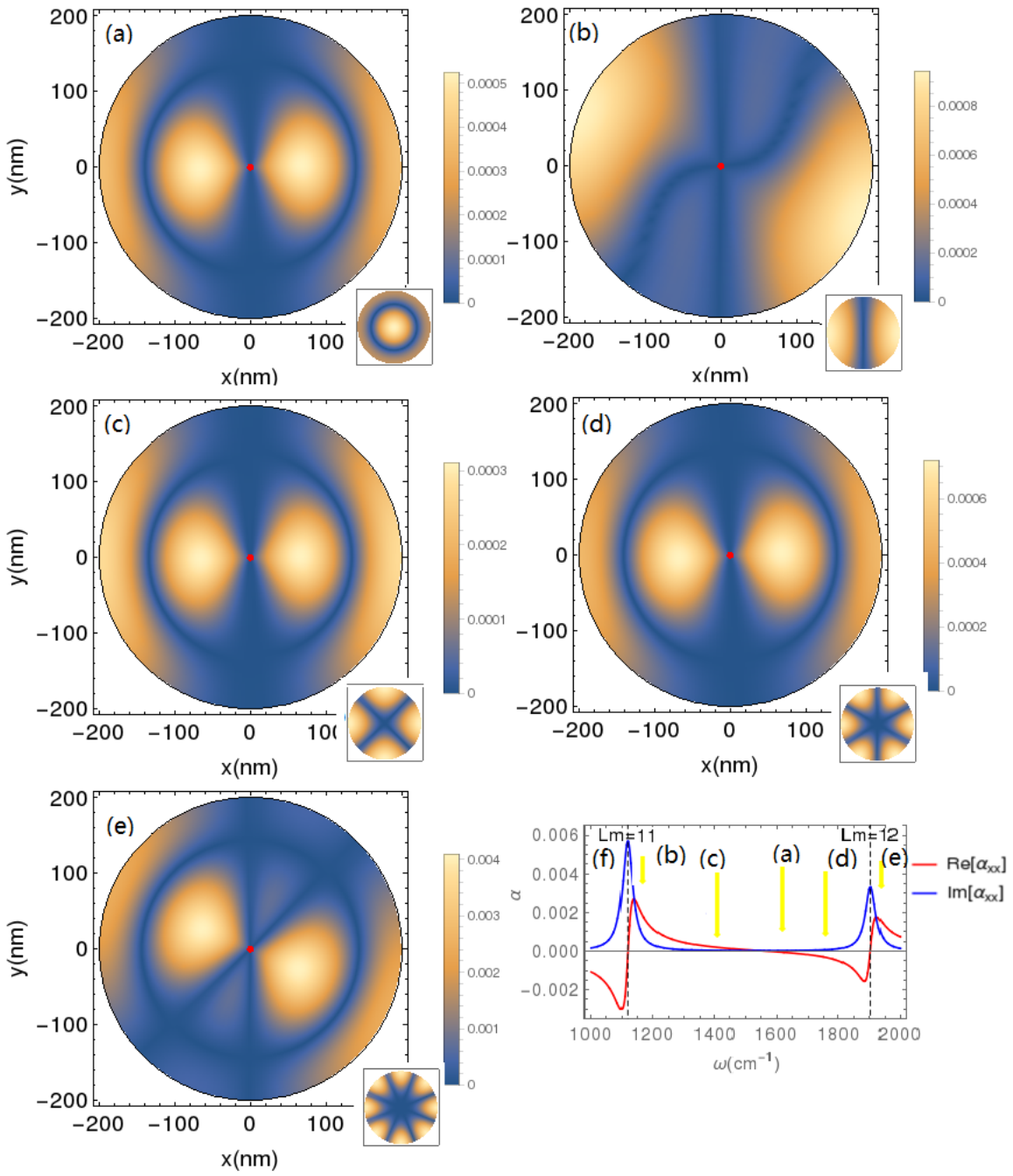

Figure 3.13: Density plot of the plasmon wavefunction of the graphene nanodisk in the presence of a **x**-oriented dipole positioned at $\mathbf{r} = (0, 0, 30)nm$ (red dot) with dipole frequency of $\omega = \omega_{Lm} + 20cm^{-1}$, for (a)$Lm = 01$,(b)$Lm = 11$,(c)$Lm = 21$,(d)$Lm = 31$,(e)$Lm = 41$. The lower right corner in each figure shows the eigenmodes of the graphene nanodisk.

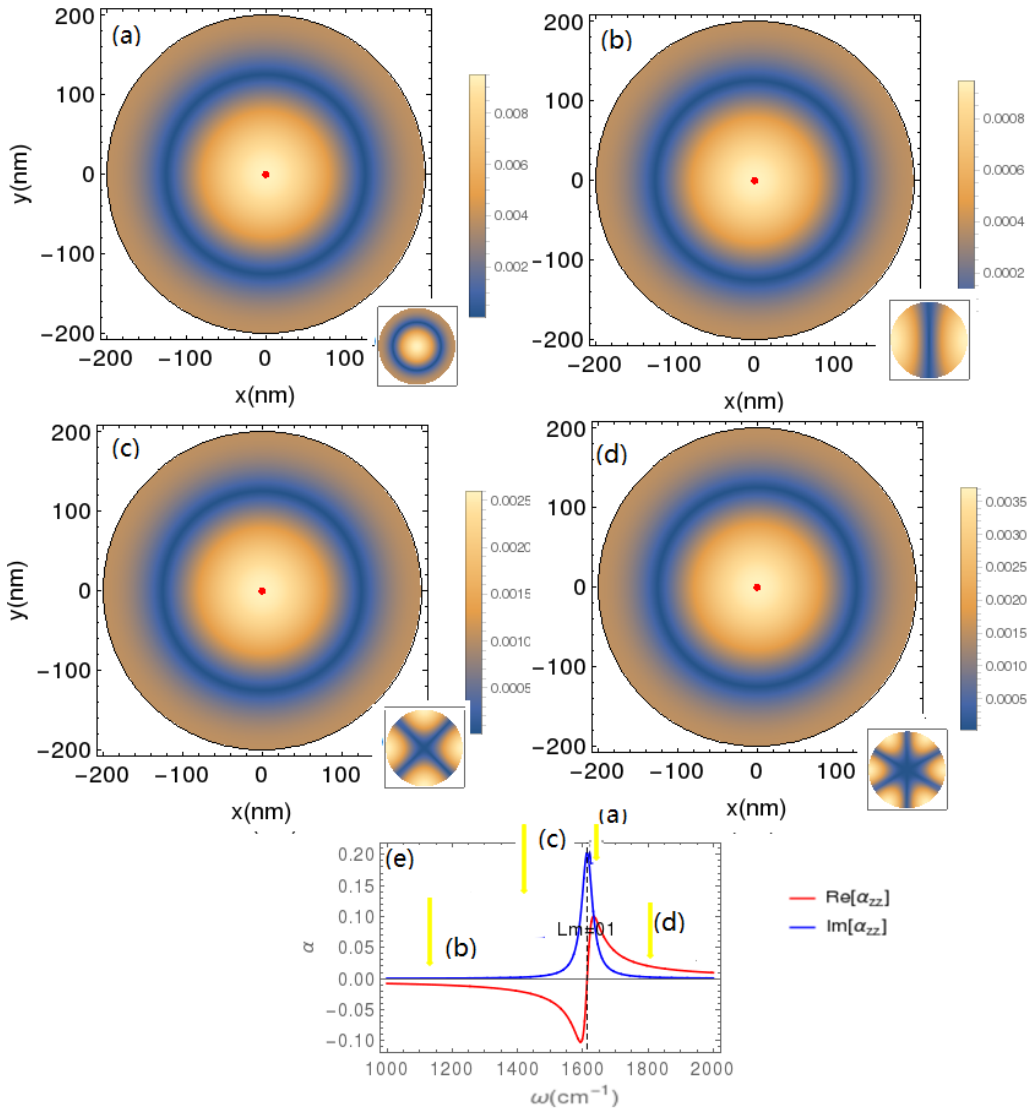

Figure 3.14: Density plot of the plasmon wavefunction of graphene nanodisk in the presence of z-oriented dipole positioned at the edge of disk $\mathbf{r} = (0, 0, 30)nm$ (gray dot) with dipole frequency $\omega = \omega_{Lm} + 20cm^{-1}$, for (a)$Lm = 01$,(b)$Lm = 11$,(c)$Lm = 21$,(d)$Lm = 31$. (f) Response function for the dipole placed at the center and along the z direction, yellow arrows indicate the position of external excitation frequency. The lower right corner in each figure shows the eigenmodes of the graphene nanodisk.

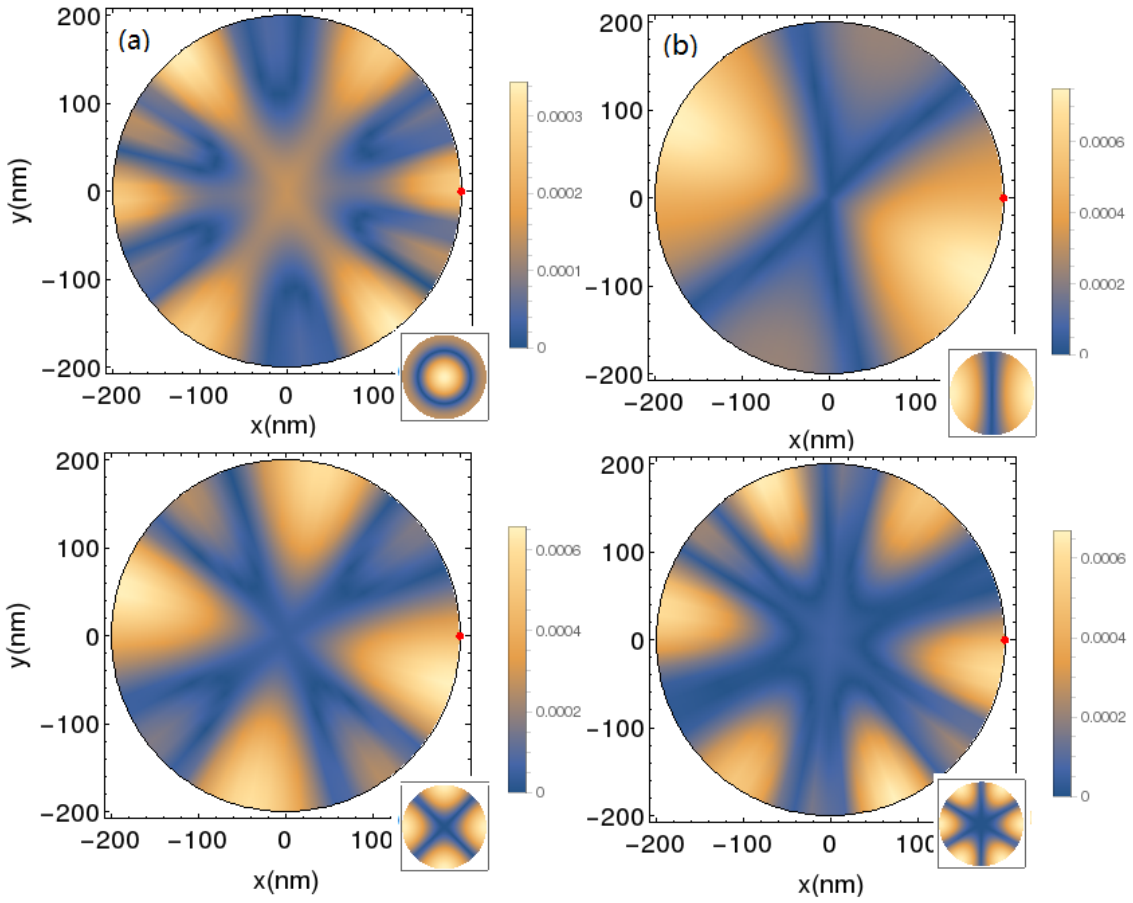

Figure 3.15: Density plot of the plasmon wavefunction of the graphene nanodisk in the presence of a x-oriented dipole positioned at the edge of disk $\mathbf{r} = (200, 0, 30)nm$ (gray dot) with dipole frequency $\omega = \omega_{Lm} + 20cm^{-1}$, for (a)$Lm = 01$,(b)$Lm = 11$,(c)$Lm = 21$,(d)$Lm = 31$. (f) Response function for the dipole placed at the center and along the x direction, yellow arrows indicate the position of external excitation frequency. The lower right corner in each figure shows the eigenmodes of the graphene nanodisk.

3.5 Summary

In this section, we explore the surface plasmons in a graphene nanodisk structure and obtain the discrete eigenfrequencies of the surface plasmons due to the geometrical restriction. We then investigate the response function of the nanodisk to an external

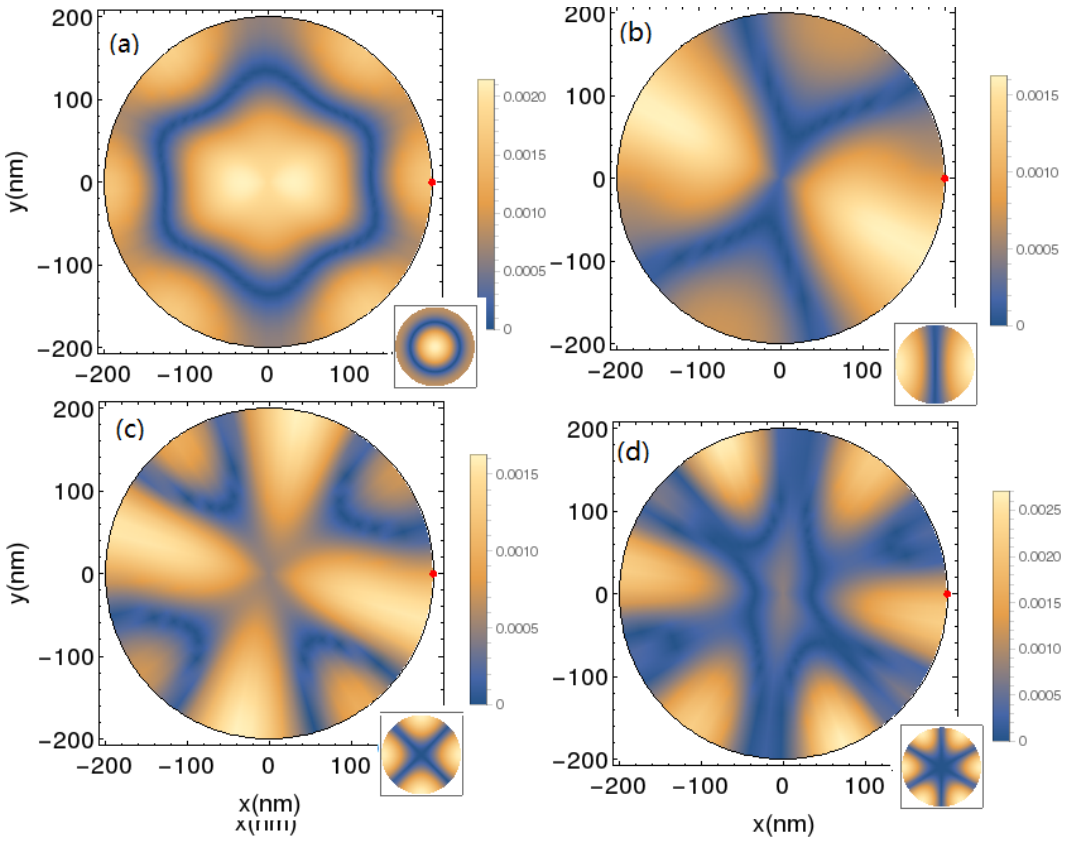

Figure 3.16: Density plot of the plasmon wavefunction of the graphene nanodisk in the presence of a z oriented dipole positioned at the edge of disk $\mathbf{r} = (200, 0, 30)nm$ (gray dot) with the dipole frequency $\omega = \omega_{Lm} + 20cm^{-1}$, for (a)$Lm = 01$,(b)$Lm = 11$,(c)$Lm = 21$,(d)$Lm = 31$.The lower right corner in each figure shows the eigenmodes of the graphene nanodisk.

dipole field and find that multiple angular modes may be excited at a single dipole frequency due to the spectral overlap of the modes with non-zero linewidth. That may explain the experimental results. However since in the experiment the graphene nanodisk is covered by an infinite large of graphene, we will consider the effect of coupling of disk plasmonic modes to the infinite graphene in Chapter 4.

Chapter 4

Plasmons in Graphene-Graphene Heterostructure

In the experiments we discussed earlier, the graphene nanodisk was buried under an infinite monolayer graphene. Such a system gives the simplest example of a heterostructure where the plasmonic modes of the graphene layer are confined due to another layer. In the previous section, we developed a model for the plasmons confined in a disk itself, neglecting the influence of the infinite monolayer graphene. Here, we investigate how the surface plasmon resonance frequency may change due to the hybridization between the monolayer and the graphene nanodisk. We also study how the rotational mismatch between the layers may results in symmetry broken plasmon patterns. In our calculations, we replace the infinite single layer graphene with a large graphene disk with $R_2 = 2000\text{nm} \gg R_1 \simeq 200\text{nm}$. We consider the Coulomb coupling between the 2D electrons which results in the hybridization of the plasmons in the different layers. Although this mechanism should be the most important for plasmon hybridization, the model can not capture the registry between the lattice of two layers. This is because our plasmon equations of motion are based on continuum approximation, neglecting lattice details. In order to capture the lattice misorientation, we introduce a phenomenological model with modulation of the Fermi level. The rotationally mismatched lattice is shown in Fig.4.1. It is

known[71] that the moiré pattern may induce a periodic modulation in the charge density and therefore modulate the conductivity. For modeling this structure, we introduce a scalar perturbation with the same symmetry as the moiré pattern of the superlattice formed in bilayer graphene. Such a potential varies smoothly within the graphene nanodisk and has a 3-fold symmetry. Other coupling, like electron transfer/tunneling between the layers, is neglected. we use the Lagrangian approach to calculating the coupled plasmon frequencies. Our model could qualitatively reproduce the hybrid plasmons with broken angular symmetry.

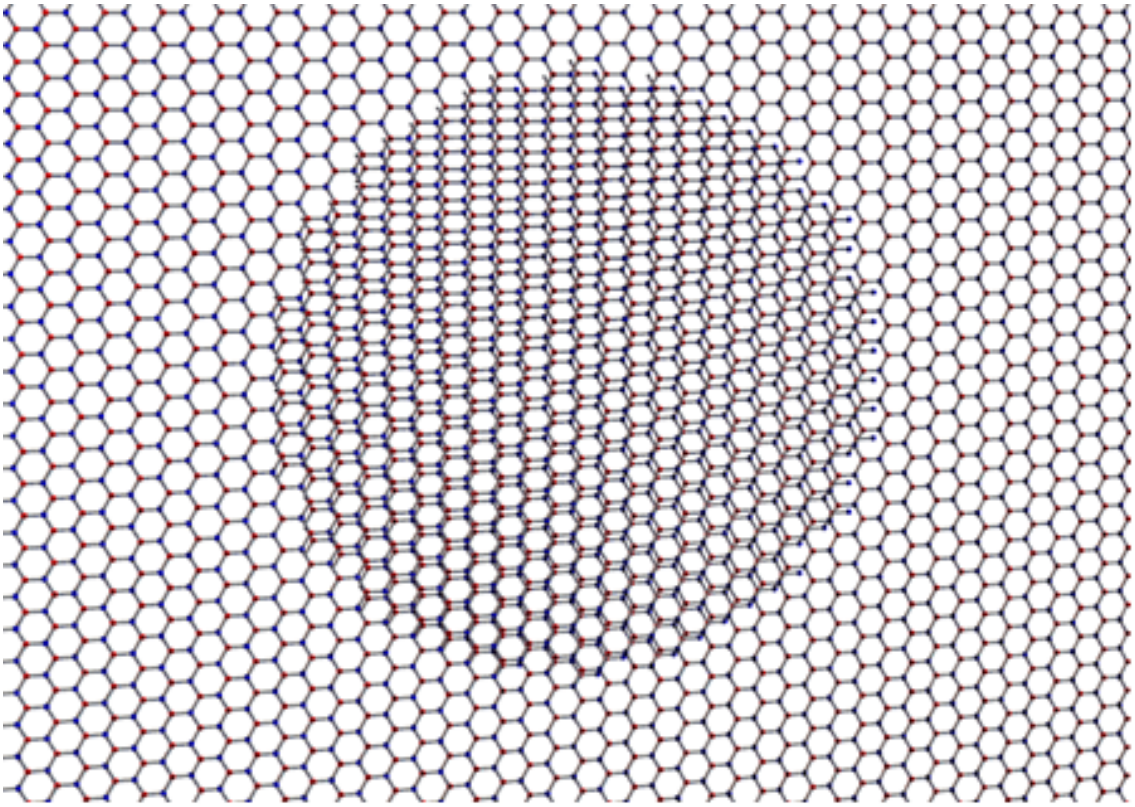

Figure 4.1: Schematic of the bilayer structure.

4.0.1 Lagrangian of the System

It is known that the frequency of the plasmons can be obtained by resolving the second quantizied Lagrangian equation for the interacting electrons (and the electric field). The classic Lagrangian function for the electron system reads:

$$\int d^2\mathbf{r}\left(\frac{mv^2}{2}-\frac{\rho\phi}{2}\right) \tag{4.1}$$

The quantum operator of the uncoupled Lagrangian of the graphene nanodisk is given by

$$\begin{aligned}\mathcal{L} &= \sum_{Lm} 2\pi R_1^2\left(\frac{i\omega R_1^2}{\sigma(\omega)\beta_{Lm}^2}-\frac{R_1}{(\epsilon_0+\epsilon_b)\beta_{Lm}}\right)\rho_{Lm}^{b+}\rho_{Lm}^{b} \\ &= \sum_{Lm} 2\pi R_1^2\frac{R_1}{(\epsilon_0+\epsilon_b)\beta_{Lm}}\left(\frac{\omega^2}{\omega_{Lm}^2}-1\right)\rho_{Lm}^{b+}\rho_{Lm}^{b}\end{aligned} \tag{4.2}$$

here ρ_{Lm}^{b+} and ρ_{Lm}^{b} are the plasmon creation and annihilation operators in the disk. L and m are the angular and radial quantum number, respectively. The plasmons in the two identical layers separated by a distance $d = 0.35nm$ are coupled via Coulomb interaction that result in splitting of the frequencies of the coupled modes. The Coulomb interaction between the two layers has the form

$$\begin{aligned}&\int d^3\mathbf{r}_1\int d^3\mathbf{r}_2\frac{\rho_b^+(\mathbf{r}_1)\rho_t(\mathbf{r}_2)}{|\mathbf{r}_1-\mathbf{r}_2|}=\int d^3\mathbf{r}_1\rho_b^+(\mathbf{r}_1)\int d^3\mathbf{r}_2\frac{\rho_t(\mathbf{r}_2)}{|\mathbf{r}_1-\mathbf{r}_2|} \\ &=\int_0^{R_1}\int_0^{2\pi} r_1dr_1d\theta_1\rho_b(r_1,\theta_1)\phi_t(r_1,\theta_1,z_1=0) \\ &=\sum_{Lmm'} A_{Lmm'}\rho_{Lm}^{b+}\rho_{Lm'}^{t}\end{aligned} \tag{4.3}$$

where ρ_b and ϕ_t are the bottom layer plasmon charge density and the potential from the top layer plasmon charge density, respectively, have the form:

$$\rho^b(\mathbf{r})=\sum_{Lm}\sqrt{\frac{2\beta_{Lm}^2}{(\beta_{Lm}^2-L^2)[J_L(\beta_{Lm})]^2}}\rho_{Lm}^{b}J_L\left(\frac{\beta_{Lm}}{R}r\right)e^{iL\theta}\delta(z) \tag{4.4}$$

$$\phi^t(\mathbf{r})=\sum_{Lm'}\sqrt{\frac{2\beta_{Lm'}^2}{(\beta_{Lm'}^2-L^2)[J_L(\beta_{Lm'})]^2}}\frac{1}{\epsilon_0+\epsilon_b}\frac{\rho_{Lm'}^{t}}{\beta_{Lm'}/R_2}J_L\left(\frac{\beta_{Lm'}}{R}r\right)e^{iL\theta}e^{-\frac{\beta_{Lm'}}{R}(d-z)} \tag{4.5}$$

And according to integral equation ([68]):

$$\int_0^{R_1} rdrJ_L\left(\frac{\beta_{Lm}}{R_1}r\right)J_L\left(\frac{\beta_{Lm'}}{R_2}r\right)=\frac{\beta_{Lm'}\frac{R_1}{R_2}J_L\left(\beta_{Lm}\right)J_L'\left(\beta_{Lm'}\frac{R_1}{R_2}\right)}{(\frac{\beta_{Lm}}{R_1})^2-(\frac{\beta_{Lm'}}{R_2})^2} \tag{4.6}$$

here $J_L'\left(\frac{\beta_{Lm'}}{R_2}R_1\right)=\frac{d}{d(\frac{\beta_{Lm'}}{R_2}r)}J_L(\frac{\beta_{Lm'}}{R_2}r)|_{r=R_1}$. Finally, we can determine Coulomb interaction matrix:

$$\begin{aligned}A_{Lmm'} &= \frac{2\pi R_1}{\epsilon_0+\epsilon_b}\sqrt{\frac{2\beta_{Lm}^2}{(\beta_{Lm}^2-L^2)[J_L(\beta_{Lm})]^2}}\sqrt{\frac{2\beta_{Lm'}^2}{(\beta_{Lm'}^2-L^2)[J_L(\beta_{Lm'})]^2}}\\ &\times J_L'\left(\beta_{Lm}\frac{R_1}{R_2}\right)\frac{J_L\left(\beta_{Lm}\right)}{(\frac{\beta_{Lm}}{R_1})^2-(\frac{\beta_{Lm'}}{R_2})^2}e^{-\frac{\beta_{Lm'}}{R}d}\end{aligned} \tag{4.7}$$

The generalization of the Lagrangian for the case of the two layers graphene is

$$\begin{aligned}\mathcal{L} &= \sum_{Lm}2\pi R_1^2\frac{R_1}{(\epsilon_0+\epsilon_b)\beta_{Lm}}\left(\frac{\omega^2}{\omega_{Lm}^2}-1\right)\rho_{Lm}^{b+}\rho_{Lm}^{b}\\ &+ \sum_{Lm'}2\pi R_2^2\frac{R_2}{(\epsilon_0+\epsilon_b)\beta_{Lm'}}\left(\frac{\omega^2}{\omega_{Lm'}^2}-1\right)\rho_{Lm}^{t+}\rho_{Lm}^{t}\\ &- \sum_{Lm'm}\rho_{Lm'}^{t+}\rho_{Lm}^{b}A_{Lm'm}-\sum_{Lmm'}\rho_{Lm}^{b+}\rho_{Lm'}^{t}A_{Lmm'}\end{aligned} \tag{4.8}$$

here we assume the layers have the same conductivity. The first term and second term in Eq.4.8 stand for the uncoupled Lagrangian of the bottom disk with radius R_1 and the top disk with radius R_2 respectively. The last two terms express Coulomb interaction between the two layers. The Lagrangian can be written in the matrix form which reads as

$$\mathcal{L}=\begin{pmatrix}2\pi R_1^2\left\{\frac{R_1}{(\epsilon_0+\epsilon_b)\beta_{Lm}}\left(\frac{\omega^2}{\omega_{Lm}^2}-1\right)\right\}\delta_{mm'} & -A_{Lmm'}\\ -A_{Lm'm} & 2\pi R_2^2\left\{\frac{R_2}{(\epsilon_0+\epsilon_b)\beta_{Lm'}}\left(\frac{\omega^2}{\omega_{Lm'}^2}-1\right)\right\}\delta_{mm'}\end{pmatrix} \tag{4.9}$$

The angular quantum number L is preserved in this Lagrangian. Solution of Eq.4.9 exists when the determinant of the system is equal to zero: $\det|\mathcal{L}|=0$. We can obtain hybridized frequency of surface plasmon due to the Coulomb coupling between the monolayer and the graphene disk.

4.0.2 Scalar Perturbation for Describing the Rotationally Mismatched Heterostructure

Rotationally mismatched lattices of the disk and the monolayer produce a moiré pattern. At a small angle of rotation such a moiré pattern could have a large superlattice constant. The pattern with a hexagonal symmetry and a central peak was observed in the experiments as shown in Fig.3.1. The size scale of this pattern is too large to attribute this to the graphene lattice with the lattice constant $\sim 2.54\mathring{A}$. Fig.4.2 shows the moiré pattern with a superlattice constant $L = 106.7nm$ at relative rotation angle $\chi = 0.98°$, which could produces a hexagonal perturbation. Calculation of the electronic structure of rotationally mismatched graphene bilayer is a complicated task. Instead, we propose a phenomenological model which can capture the main physics of the effect for the hybrid plasmon modes.

We construct a triangular perturbation to mimic the shape of a moiré superlattice generated by the two mismatched layers. This scalar perturbation varies in the real space as shown in Fig.4.3. Assuming the perturbation due to the moiré pattern varies smoothly, we write the perturbation function as a Fourier series:

$$\begin{aligned} V(r) &= \sum_G V_G e^{i\vec{G}\cdot\vec{r}} \\ &= V_0 + V_1\left(e^{iGy} + e^{-iGy}\right) + e^{iGy/2}e^{iG\frac{\sqrt{3}}{2}x} + V_1 e^{iGy/2}e^{iG\frac{-\sqrt{3}}{2}x} \\ &+ V_1 e^{-iGy/2}e^{iG\frac{\sqrt{3}}{2}x} + V_1 e^{-iGy/2}e^{-iG\frac{-\sqrt{3}}{2}x} \\ &= V_0 + V_1\left(2\cos(Gy) + 4\cos(Gy/2)\cos(G\frac{\sqrt{3}}{2}x)\right) \\ &= V_0\left(1 + \frac{V_1}{V_0}\left(2\cos(Gy) + 4\cos(Gy/2)\cos(G\frac{\sqrt{3}}{2}x)\right)\right) \end{aligned} \tag{4.10}$$

where G is the moiré pattern reciprocal lattice vector $G = \frac{4\pi}{3L}$, V_G is the Fourier expansion constant and we keep the two lead terms in the series. This function may describe the periodic modulation in the charge density of misoriented bilayer and therefore modulation in the Fermi energy.

$$E_F = E_F^0\left(1 + \xi F(r)\right) \tag{4.11}$$

where $F(r) = 2\cos(Gy) + \cos(Gy/2)\cos(G\frac{\sqrt{3}}{2}x)$ is the model function to describe phenomenologically moiré pattern, ξ is the unitless strength of the perturbation. Then the kinetic energy term becomes

$$\begin{aligned}
K &= \int_0^{R_1}\int_0^{2\pi} \rho(r,\theta)(\frac{i\omega R_1^2}{\sigma(\omega)\beta_{Lm}^2})\rho(r,\theta) r dr d\theta \\
&= \frac{\pi\hbar^2\omega^2 R_1^2}{e^2\beta_{Lm}^2}\int_0^{R_1}\int_0^{2\pi} \rho(r,\theta)\frac{1}{E_F^0\left(1+\xi F(r)\right)}\rho(r,\theta) r dr d\theta \\
&\approx \frac{\pi\hbar^2\omega^2 R_1^2}{e^2\beta_{Lm}^2}\int_0^{R_1}\int_0^{2\pi} \rho(r,\theta)\frac{1}{E_F^0}\left(1-\frac{\xi F(r)}{1+\xi F(r)}\right)\rho(r,\theta) r dr d\theta \\
&= K_0 - \frac{\pi\hbar^2\omega^2 R_1^2\xi}{e^2 E_F^0\beta_{Lm}^2}\int_0^{R_1}\int_0^{2\pi} \rho(r,\theta)F(r)\rho(r,\theta) r dr d\theta \\
&= K_0 - \frac{\pi\hbar^2\omega^2 R_1^2\xi}{e^2 E_F^0\beta_{Lm}^2} B_{LmL'm'} \qquad (4.12)
\end{aligned}$$

where $K_0 = 2\pi R_1^2 \frac{R_1}{(\epsilon_0+\epsilon_b)\beta_{Lm}}\frac{\omega^2}{\omega_{Lm}^2}$, $B = \int_0^{R_1}\int_0^{2\pi}\rho(r,\theta)F(r)\rho(r,\theta) r dr d\theta$. We add this perturbation to the Lagrangian:

$$\begin{aligned}
\mathcal{L} &= \sum_{LL'mm'} 2\pi R_1^2 \frac{R_1}{(\epsilon_0+\epsilon_b)\beta_1}\left\{\frac{\omega^2}{\omega_1^2}\left(\delta_{LL'}\delta_{mm'} - \frac{\xi B_{LmL'm'}}{2\pi R_1^2}\right) - \delta_{LL'}\delta_{mm'}\right\}\rho_1^{b+}\rho_1^b \\
&+ \sum_{LL'nn'} 2\pi R_2^2 \frac{R_2}{(\epsilon_0+\epsilon_b)\beta_2}\left\{\frac{\omega^2}{\omega_2^2}\left(\delta_{LL'}\delta_{nn'} - \frac{\xi B_{LnL'n'}}{2\pi R_2^2}\right) - \delta_{LL'}\delta_{nn'}\right\}\rho_2^{t+}\rho_2^t \\
&- \sum_{Lnm}\rho_2^{t+}\rho_1^b A_{Lnm}\delta_{LL'} - \sum_{Lmn}\rho_1^{b+}\rho_2^t A_{Lmn}\delta_{LL'} \qquad (4.13)
\end{aligned}$$

here, $\rho_1 = \rho_{Lm}$, $\rho_2 = \rho_{Ln}$, $\beta_1 = \beta_{Lm}$, $\beta_2 = \beta_{Ln}$.

The Lagrangian can be written in the matrix form which reads as

$$\mathcal{L} = \begin{pmatrix} L_{11} & L_{12} \\ L_{21} & L_{22} \end{pmatrix} \qquad (4.14)$$

here L_{11},L_{22} are the Lagrangian of the bottom disk and the top graphene layer, respectively. L_{12} and L_{21} are the Coulomb interaction between the two layers. In our case, both angular quantum numbers L_1 and L_2 are up to 6 (0$\rightarrow$ 6), but the radial quantum number m_1 is up to 5 (1$\rightarrow$ 5) for the bottom disk and m_2 is up to 50 (1$\rightarrow$ 50) for the large top disk. Therefore, matrix $\mathcal{L}$ is 385$\times$385 and α is 1 $\rightarrow$

385. The model perturbation due to the mismatched lattice results in the modified plasmon dispersion such that the modes with different angular quantum numbers can mix. We can obtain the modified plasmon dispersion due to mismatched lattice from the determinant of the Lagrangian: $\det|\mathcal{L}| = 0$.

4.0.3 Discussion

The problem was soloved numerically. In Fig.4.4, we plot the plasmon wavefunction at the frequency of $\omega = 1323cm^{-1}$, which contains the pattern resembling of $L = 0$ and $L = 6$ modes. We also plot the angular components of the wavefunctions in Fig.4.4 (bottom). It shows that $L = 0$ and $L = 6$ harmonics have the largest and approximately equal contribution. From the radial dependence of the angular components of the wavefunction we can identify which radial modes are involved in the mixed mode. Fig.4.5 and Fig.4.6 show the wavefunctions at frequency of $\omega = 1389cm^{-1}$ and $\omega = 1669cm^{-1}$, respectively. Both patterns indicate the plasmons with strong coupling between $L = 0$ and $L = 6$ modes. Most of the hybrid modes are non-bound plasmons, for example in Fig.4.7, the pattern shows the $L = 2$ mode. While some of the modes are strongly confined inside the disk, fig.4.8 shows that the amplitude of a wavefunction is larger inside than outside the disk at the frequency of $\omega = 1322cm^{-1}$, and $\omega = 1621cm^{-1}$. While at the frequency of $\omega = 1389cm^{-1}$ and $\omega = 1669cm^{-1}$, we observe leaky modes. We stress that the confinement is due to the step in the conductivity at the border of the bilayer graphene which has twice layer charge density than that the monolayer, thus creating a "refraction index" step for the plasmon propagation.

4.1 Response function to a field of an External Dipole

The total Hamiltonian of the system is

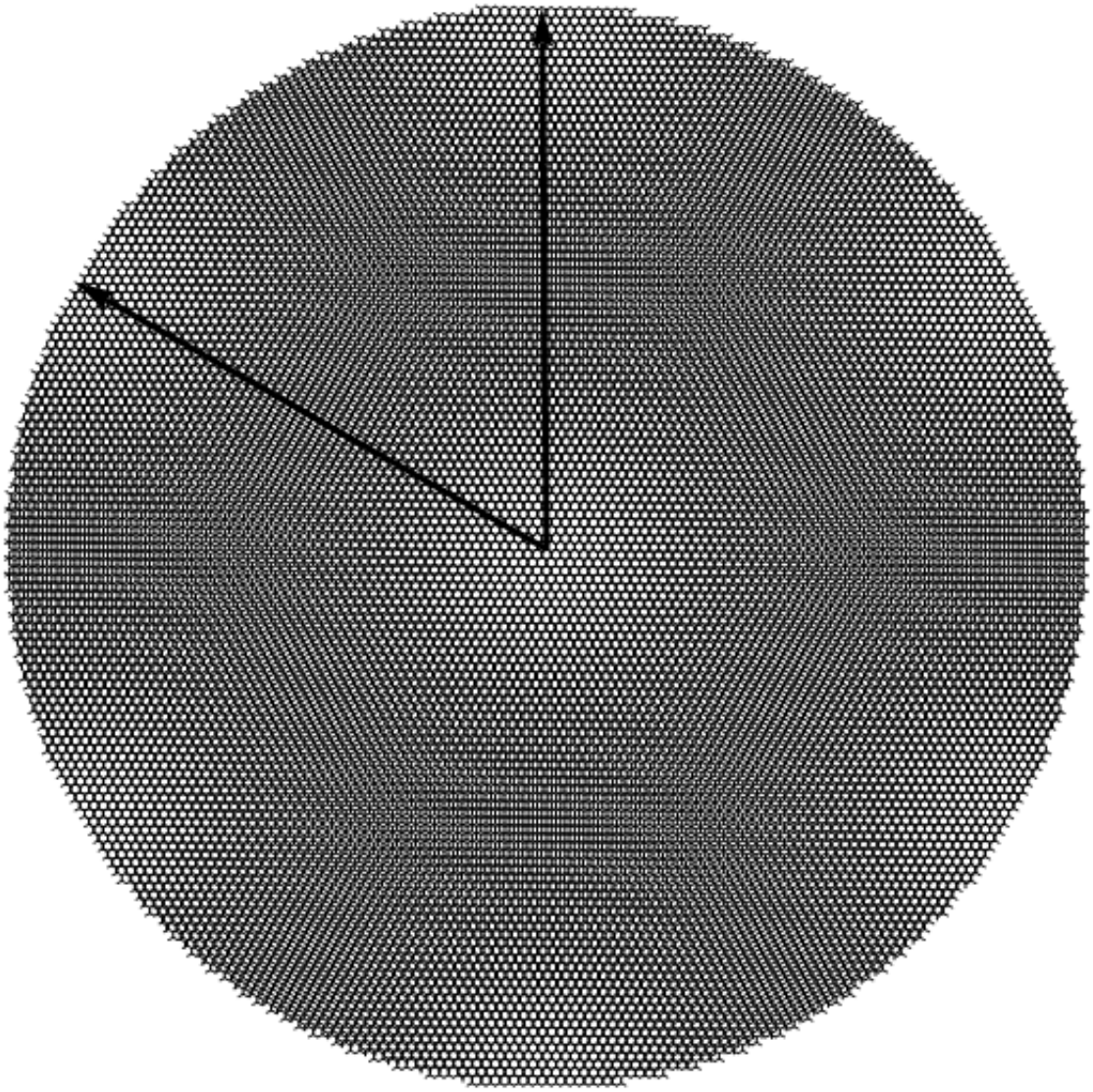

Figure 4.2: Moiré pattern when $i = 33$ for rotation angle $\chi = 0.98°$.

$$H = \sum_{\alpha} \hbar\omega_{\alpha}\rho_{\alpha}^{+}\rho_{\alpha} \tag{4.15}$$

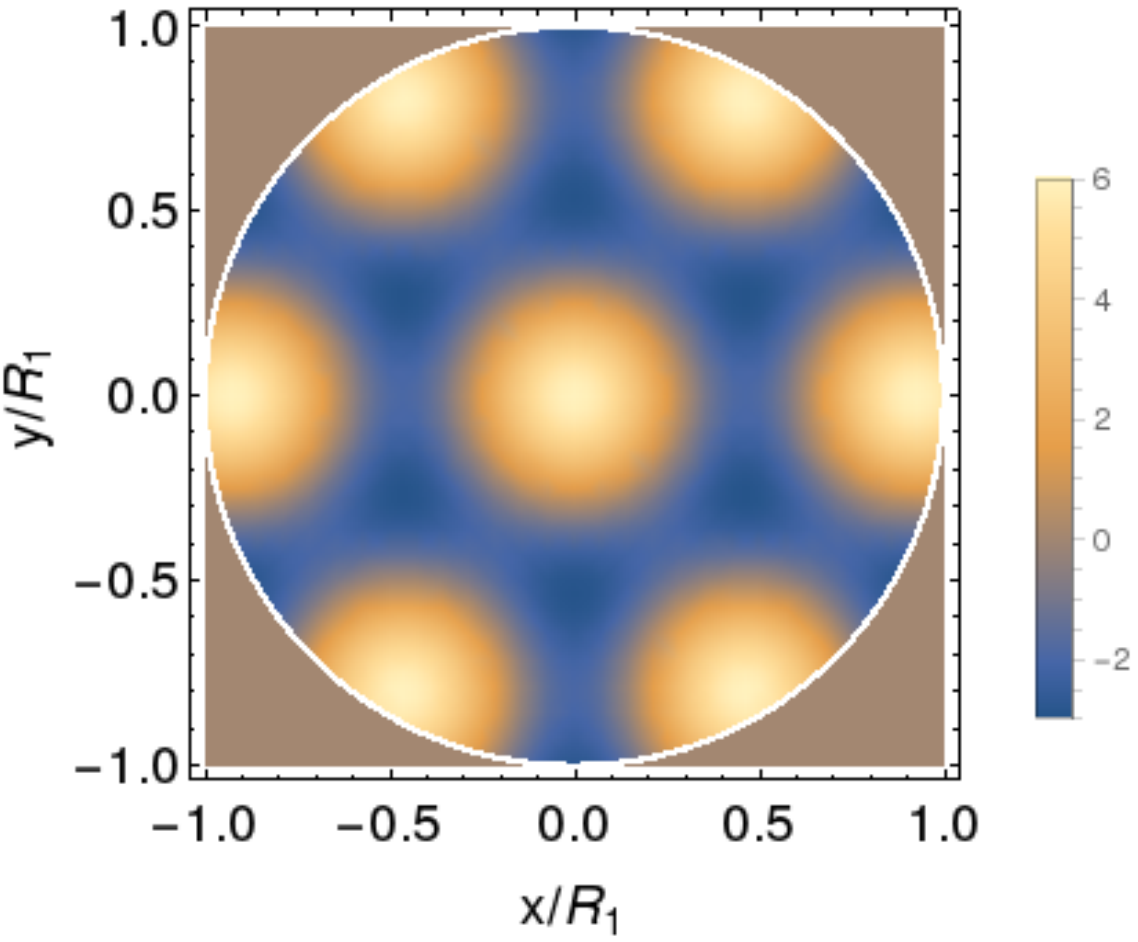

Figure 4.3: Schematic of scalar perturbation function describing the moiré pattern effect.

Here α is the eigenfrequency of the surface plasmons in the bilayer. ρ_α is the plasmon operator. The wavefunction of the surface plasmons in the bilayer has the form (note that in this section we use $\psi(\mathbf{r})$ to express the wavefunction of the surface plasmons, and use $\rho(\mathbf{r})$ to express the plasmon annihilation operator).

$$\psi_\alpha(\mathbf{r}) = \left\{ \sum_{L_1 m_1} \rho^\alpha_{L_1 m_1} J_{L_1}\left(\frac{\beta_{L_1 m_1}}{R_1} r\right) e^{iL_1\theta_1} \delta(z - z_1), \sum_{L_2 m_2} \rho^\alpha_{L_2 m_2} J_{L_2}\left(\frac{\beta_{L_2 m_2}}{R_2} r\right) e^{iL_2\theta_2} \delta(z - z_2) \right\} \tag{4.16}$$

here ρ^{α}_{Lm} is the amplitudes of $|\alpha\rangle$ of the mixed plasmons in terms of non-hybridized basis $|Lm\rangle$. The plasmon annihilation operator in the real space is expressed as,

$$\rho(\mathbf{r}) = \sum_{\alpha} \rho_{\alpha} \psi_{\alpha}(\mathbf{r}) \tag{4.17}$$

The Hamiltonian due to the external potential can be expressed as:

$$\begin{aligned} H^{ext} &= \int d^2\mathbf{r}\phi^{ext}(\mathbf{r})\rho^{+}(\mathbf{r}) \\ &= \sum_{\alpha}\sum_{L_1m_1}\int d^2\mathbf{r}\phi^{ext}(r,z_1)J_{L_1}\left(\frac{\beta_{L_1m_1}}{R_1}r\right)e^{-iL_1\theta_1}(\rho^{\alpha}_{L_1m_1})^{*}\rho^{+}_{\alpha} \\ &+ \sum_{\alpha}\sum_{L_2m_2}\int d^2\mathbf{r}\phi^{ext}(r,z_2)J_{L_2}\left(\frac{\beta_{L_2m_2}}{R_2}r\right)e^{-iL_2\theta_2}(\rho^{\alpha}_{L_2m_2})^{*}\rho^{+}_{\alpha} \\ &= \sum_{\alpha} V^{\alpha}\rho^{+}_{\alpha} \end{aligned}$$

and V_{α} is the spinor representation of the coupling operator in $|\alpha\rangle$ space,

$$\begin{aligned} \mathbf{V}^{\alpha} &= \begin{pmatrix} \sum_{L_1m_1}\int d^2\mathbf{r}\phi^{ext}(r,z_1)J_L\left(\frac{\beta_{L_1m_1}}{R_1}r\right)e^{-iL_1\theta_1}(\rho^{\alpha}_{L_1m_1})^{*} \\ \sum_{L_2m_2}\int d^2\mathbf{r}\phi^{ext}(r,z_2)J_L\left(\frac{\beta_{L_2m_2}}{R_2}r\right)e^{-iL_2\theta_2}(\rho^{\alpha}_{L_2m_2})^{*} \end{pmatrix} \\ &= \begin{pmatrix} \mathbf{g}_1\cdot\mathbf{p} \\ \mathbf{g}_2\cdot\mathbf{p} \end{pmatrix} \end{aligned} \tag{4.18}$$

here $\mathbf{g}_1 = \sum_{L_1m_1}\int d^2\mathbf{r}\nabla\frac{1}{|\mathbf{r}'-\mathbf{r}|}|_{z=z_1}J_{L_1}\left(\frac{\beta_{L_1m_1}}{R_1}r\right)e^{-iL_1\theta_1}(\rho^{\alpha}_{L_1m_1})^{*}$,
and $\mathbf{g}_2 = \sum_{L_2m_2}\int d^2\mathbf{r}\nabla\frac{1}{|\mathbf{r}'-\mathbf{r}|}|_{z=z_2}J_{L_2}\left(\frac{\beta_{L_2m_2}}{R_2}r\right)e^{-iL_2\theta_2}(\rho^{\alpha}_{L_2m_2})^{*}$. We assume the perturbation is switched on "adiabatically". We therefore write

$$\mathbf{V}(\omega) = \mathbf{V}e^{-i(\omega+i\eta)t} \tag{4.19}$$

where $\eta \to 0^{+}$. In terms of an exact unperturbed, time-independent ket basis set $|\beta\rangle$, the perturbed ground state $|g(t)\rangle$ can be written, according to the time-dependent perturbation theory

$$|g(t)\rangle = |0\rangle + \sum_{\beta} c_{\beta}(t)e^{-i\omega_{\beta}t}|\beta\rangle \tag{4.20}$$

Here $|0\rangle$ is the ground state wavefunction with the ground state energy equal 0. According to the Schrödinger equation:

$$i\frac{\partial|g(t)\rangle}{\partial t} = (H + H^{ext})|g(t)\rangle \tag{4.21}$$

Then the time-dependent coefficient is found from:

$$i\dot{c}_\beta(t) = \langle 0|H^{ext}|\beta\rangle e^{i(\omega-\omega_\beta+i\eta)t} \tag{4.22}$$

Integrating the equation above from $t = -\infty$ to ∞ gives

$$\begin{aligned} c_\beta(t) &= -\frac{\langle 0|H^{ext}|\beta\rangle}{\omega-\omega_\beta+i\eta}e^{-i(\omega+i\eta)t} && (4.23)\\ &= -\sum_\alpha \frac{\mathbf{V}_\alpha\langle 0|\rho_\alpha|\beta\rangle}{\omega-\omega_\beta+i\eta}e^{-i(\omega+i\eta)t} && (4.24)\end{aligned}$$

We note that the charge density is given by the expectation value of $\rho_{\mathbf{r}}$, thus we assume that the charge density is zero in the vacuum state. Then we write

$$\langle\rho_\alpha^+\rangle = -\sum_\beta \frac{\mathbf{V}_\alpha\langle\beta|\rho_\alpha^+|0\rangle\langle 0|\rho_\alpha|\beta\rangle}{\omega-\omega_\beta+i\eta} \tag{4.25}$$

This allows us to find the average of the charge density operator in Eq.4.17:

$$\begin{aligned}\rho(\mathbf{r}) &= \sum_{\alpha\beta}\psi_\alpha(\mathbf{r})\frac{\mathbf{V}_\alpha\langle\beta|\rho_\alpha^+|0\rangle\langle 0|\rho_\alpha|\beta\rangle}{\omega-\omega_\beta+i\eta}\\ &= \sum_\alpha \psi_\alpha(\mathbf{r})\frac{\mathbf{V}_\alpha}{\omega-\omega_\alpha+i\eta} && (4.26)\end{aligned}$$

where we use that $\langle\beta|\rho_\alpha^+|0\rangle = \delta_{\alpha\beta}$. The electric field of graphene at the position of

$\mathbf{r}$ has the form

$$\begin{aligned}
\mathbf{E}(\mathbf{r}) &= -\nabla \int_0^R \int_0^{2\pi} \frac{\rho(\mathbf{r}')}{|\mathbf{r}-\mathbf{r}'|} r' dr' d\theta \\
&= -\sum_\alpha \int_0^R \int_0^{2\pi} \nabla \frac{\psi_\alpha(\mathbf{r}')}{|\mathbf{r}-\mathbf{r}'|} r' dr' d\theta \frac{\mathbf{V}_\alpha}{\omega - \omega_\alpha + i\eta} \\
&= -\sum_\alpha \int_0^R \int_0^{2\pi} \sum_{L_1 m_1} \nabla \frac{1}{|\mathbf{r}-\mathbf{r}'|}_{z'=z_1} J_{L_1}\left(\frac{\beta_{L_1 m_1}}{R_1} r'\right) e^{iL_1\theta_1} \rho^\alpha_{L_1 m_1} r' dr' d\theta_1 \frac{\mathbf{g}_1 \cdot \mathbf{p}}{\omega - \omega_\alpha + i\eta} \\
&- \sum_\alpha \int_0^R \int_0^{2\pi} \sum_{L_2 m_2} \nabla \frac{1}{|\mathbf{r}-\mathbf{r}'|}_{z'=z_2} J_{L_2}\left(\frac{\beta_{L_2 m_2}}{R_2} r'\right) e^{iL_2\theta_2} \rho^\alpha_{L_2 m_2} r' dr' d\theta_2 \frac{\mathbf{g}_2 \cdot \mathbf{p}}{\omega - \omega_\alpha + i\eta} \\
&= -\sum_\alpha \frac{\mathbf{g}_1^* \mathbf{g}_1 + \mathbf{g}_2^* \mathbf{g}_2}{\omega - \omega_\alpha + i\eta} \cdot \mathbf{p} \qquad (4.27)
\end{aligned}$$

where the response function tensor has the form:

$$\hat{\alpha} = -\sum_\alpha \frac{\mathbf{g}_1^* \mathbf{g}_1 + \mathbf{g}_2^* \mathbf{g}_2}{\omega - \omega_\alpha + i\eta} \qquad (4.28)$$

4.1.1 Discussion

In Fig.4.9 we plot the frequency dependence of the zz component of the response function to the external dipole placed in the middle or at the edge of the disk. We can see multiple resonance peaks, and due to the Coulomb interaction between the two layers the resonance peaks are shifted compared with the resonance frequencies of the plasmons in the single disk. When the dipole is along the z axis and placed at the center of the disk, the plasmon modes with $L = 0$ contribute to the response function of a single disk. However with moiré perturbation, mixing of states with a higher angular momentum is allowed. The wavefunciton of the plasmon modes at the resonance peaks in Fig.4.9 contains large $L = 0$ component. In Fig.4.10, the plasmon wavefunctions at the fixed dipole position $\mathbf{r} = (0, 0, 30nm)$ with different dipole frequencies are plotted. At the frequency of $\omega = 1633cm^{-1}$, the plasmon wavefunction in Fig.4.10(a) shows the $L = 0, 3$ pattern. And the plasmon wavefunctions in Fig.4.10(b) and (c) show the $L = 0$ pattern. We also notice that the plasmon wavefunctions are strongly confined within the nanodisk at those frequencies due to the larger conductivity of the bilayer structure. If the external dipole

is off the center of the disk, for example, $\mathbf{r} = (100nm, 100nm, 30nm)$ in Fig.4.11 and $\mathbf{r} = (200nm, 0, 30nm)$, the patterns have complex shape, which indicates that multiple plasmon modes are excited. At the position under the dipole, a stronger excitation amplitude is observed which is due to the fact that the perturbation lowers the symmetry of plasmonic system so much that many multipoles are excited simultaneously. In contrast to the case of a simple disk with axial symmetry, here the tip (dipole) can produce a plasmonic localized image.

4.2 Conclusion

In this section, we considered the hybridization of the surface plasmons between the monolayer and the graphene nanodisk. We demonstrated the shift of the hybrid plasmon modes compare to the uncoupled plasmon modes in the nanodisk and the monolayer graphene. Plasmon coupling between modes with different angular quantum numbers occurs due to the rotationally mismatched lattice between the disk and monolayer, which may induce a scalar perturbation within the graphene disk. We also observe that the plasmon modes are strongly confined within the disk due to the step in the conductivity at the edge of the disk. Different patterns of the hybrid surface plasmons are observed.

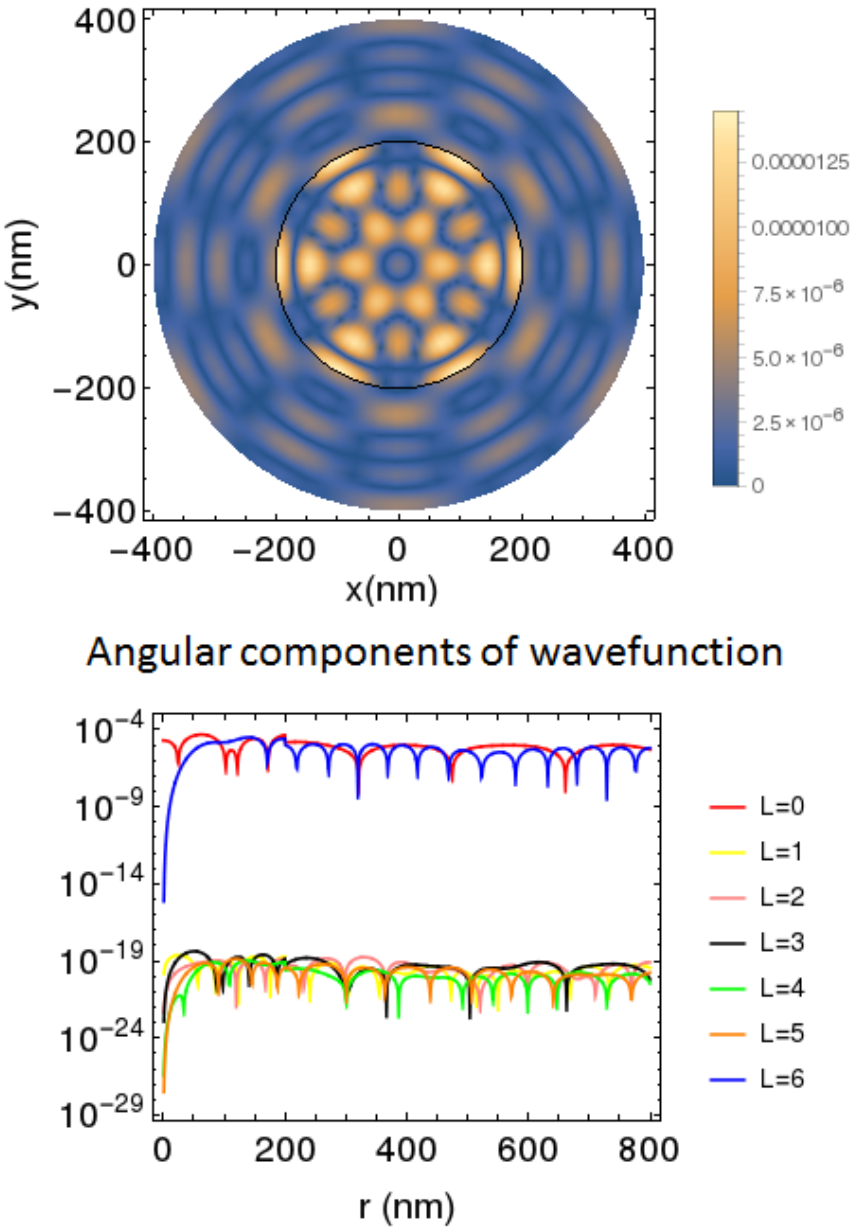

Figure 4.4: Top: Density plot of the plasmon wavefuction at the frequency of $\omega = 1323 cm^{-1}$. Bottom: Angular components of the wavefunctions as a function of the radial distance.

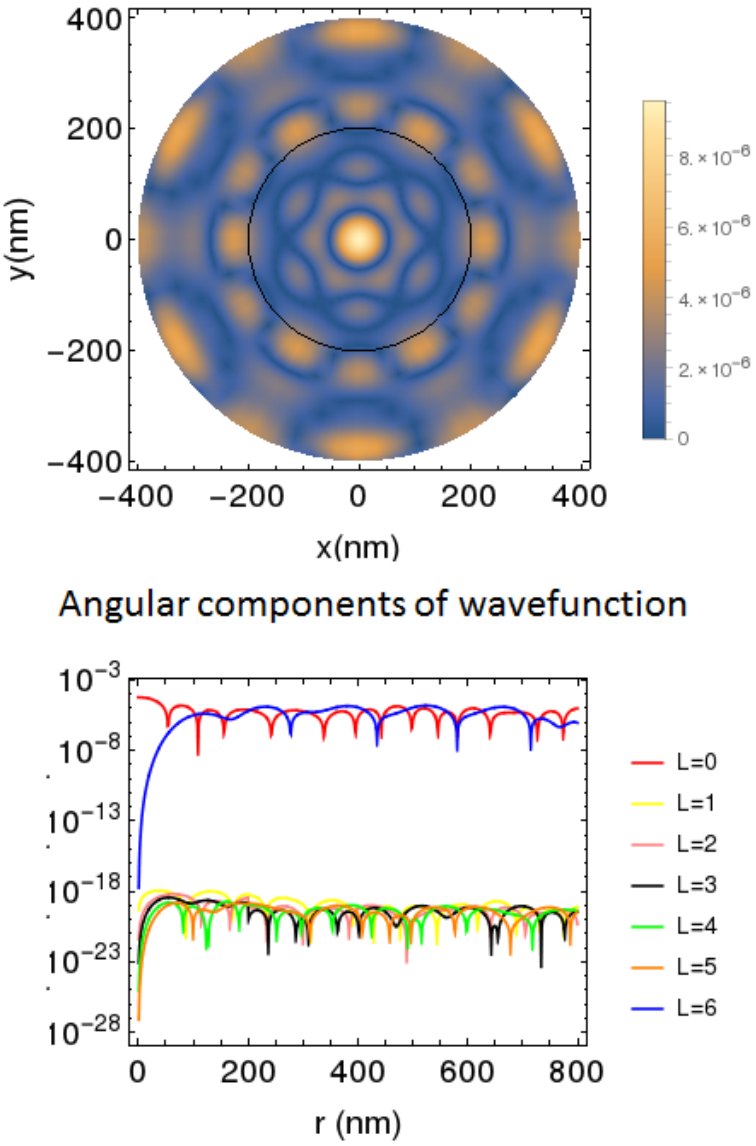

Figure 4.5: Top: Density plot of the plasmon wavefuction at the frequency of $\omega = 1389cm^{-1}$. Bottom: Angular components of the wavefunctions as a function of the radial distance.

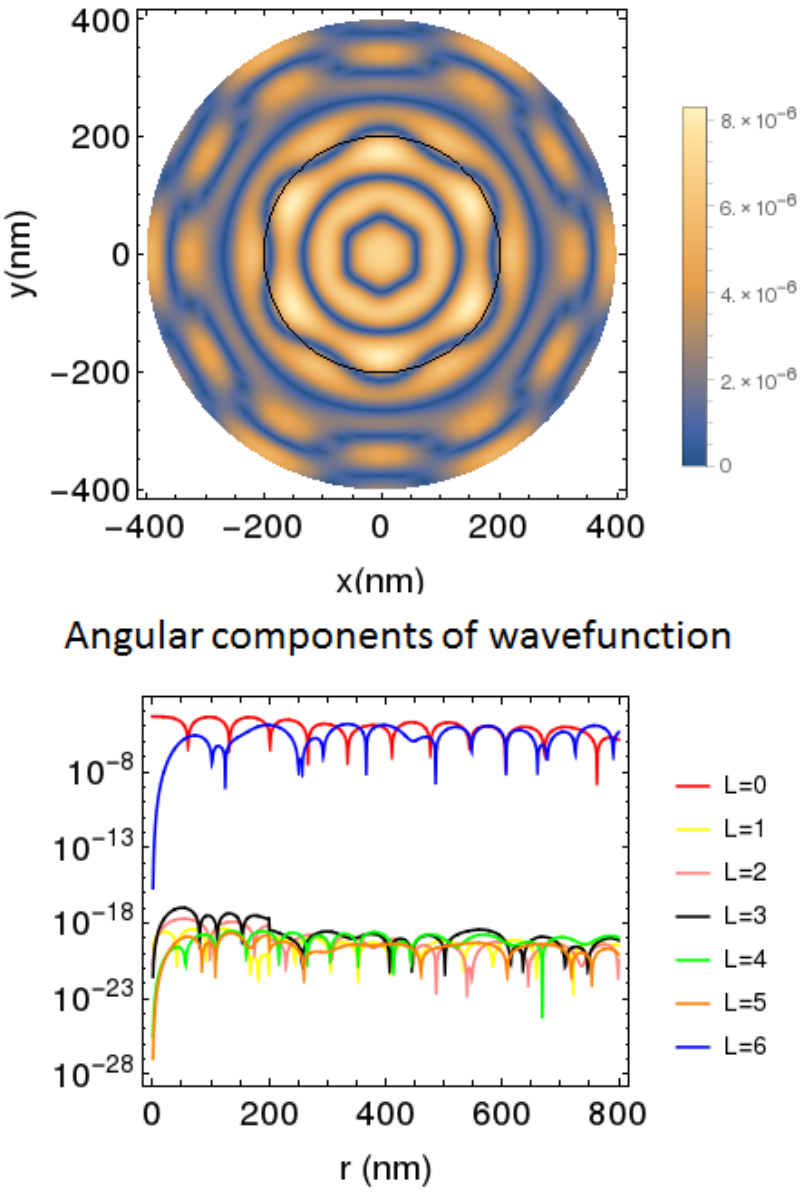

Figure 4.6: Top: Density plot of the plasmon wavefuction at the frequency of $\omega = 1669 cm^{-1}$. Bottom: Angular components of the wavefunctions as a function of the radial distance.

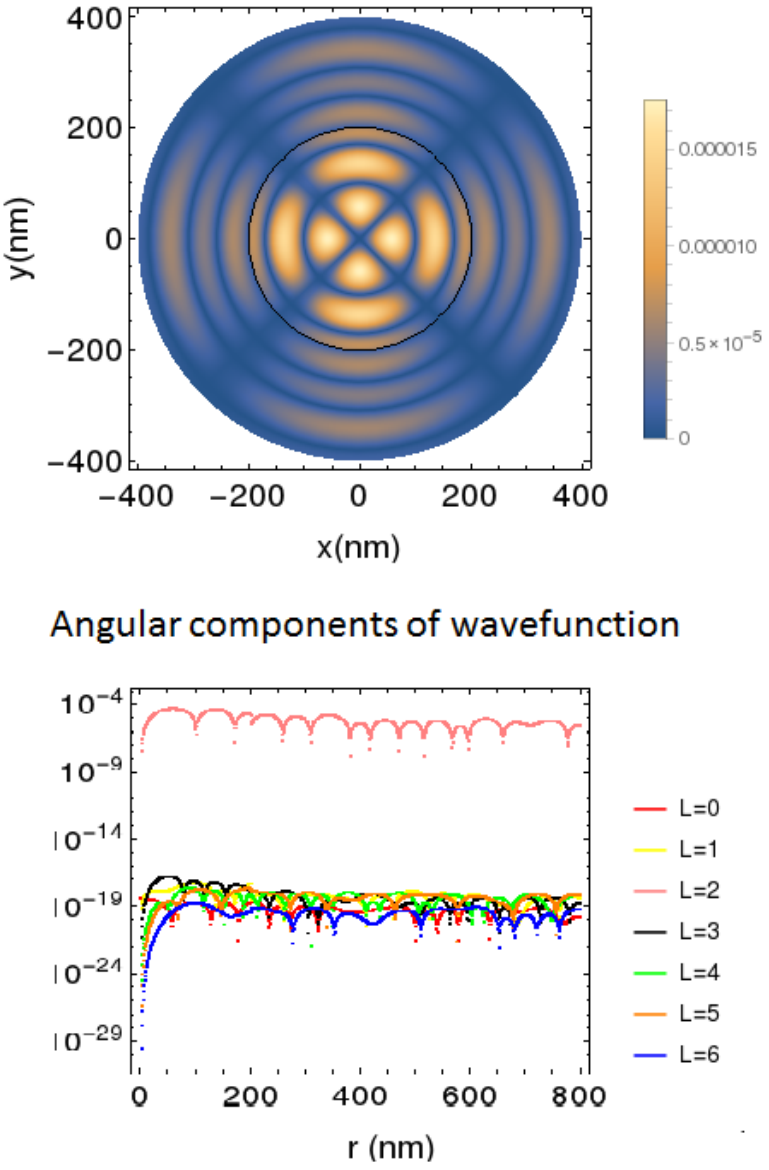

Figure 4.7: Top: Density plot of the plasmon wavefuction at the frequency of $\omega = 1621 cm^{-1}$. Bottom: Angular components of the wavefunctions as a function of the radial distance.

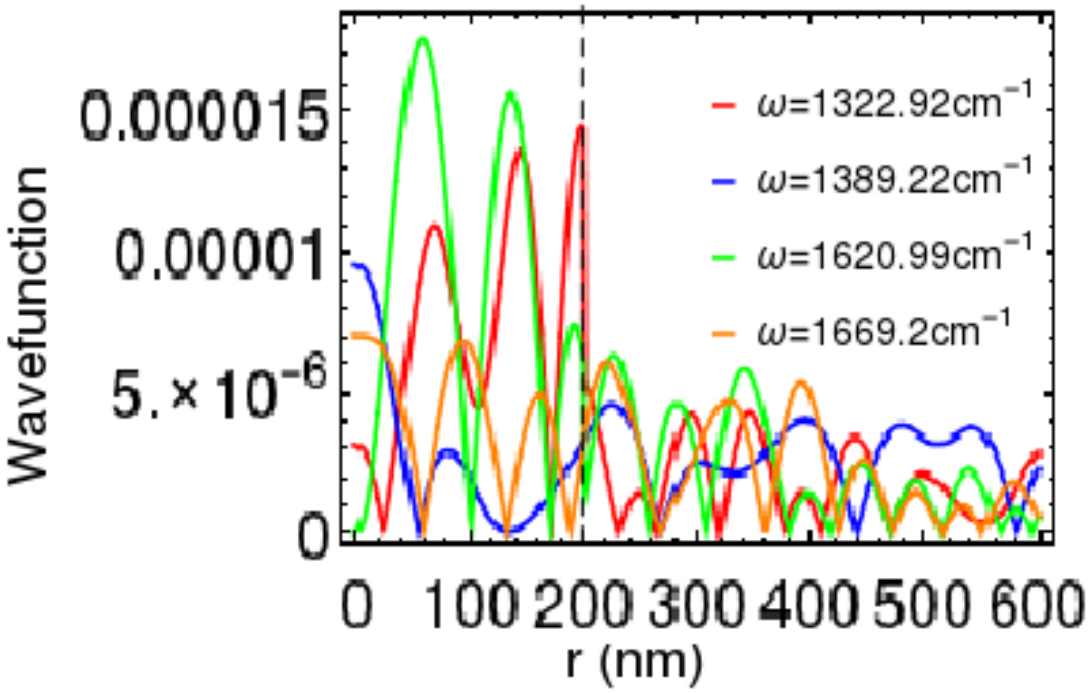

Figure 4.8: Absolute value of the plasmon wavefunction at $\theta = 0$ as a function of the radius distance. The dashed line indicates the position of the disk at $r = 200nm$.

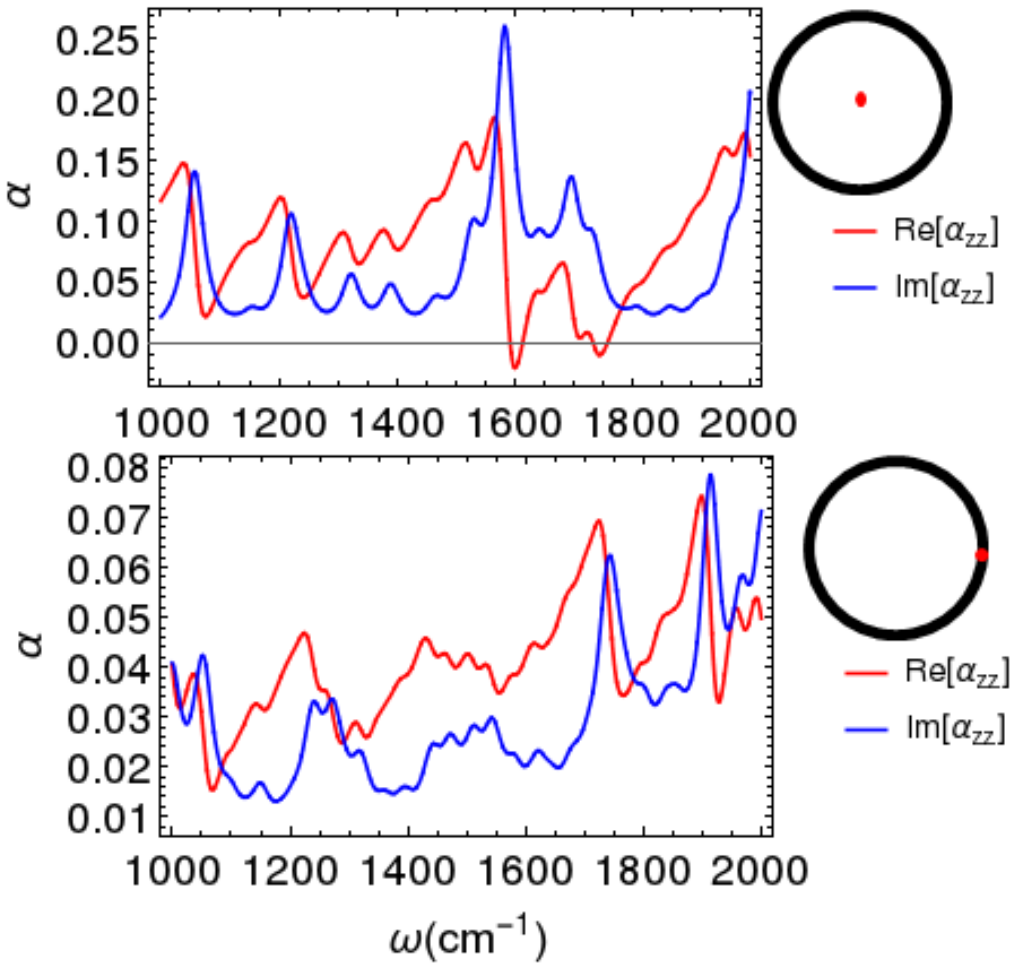

Figure 4.9: Frequency dependence of the real part and the imaginary part of the response function of the system to a z-oriented dipole placed at the center of the nanodisk (top) and at the edge of the nanodisk (bottom).

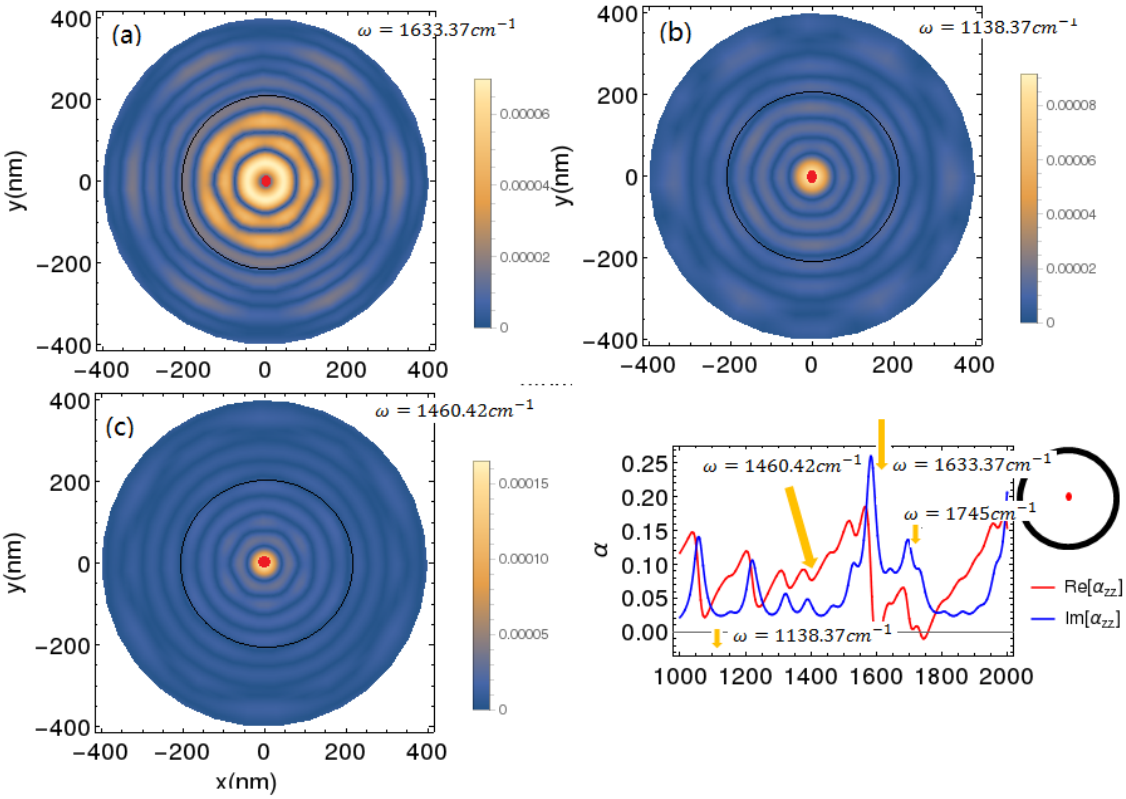

Figure 4.10: Density plot of the plasmon wavefunction in the presence of a z-oriented dipole placed at the center of the disk with the frequency, for (a)$\omega = 1633cm^{-1}$, (b)$\omega = 1138cm^{-1}$, (c)$\omega = 1460cm^{-1}$. The red dot at the center shows the position of the external dipole, and the dashed circle indicate the position of the disk.

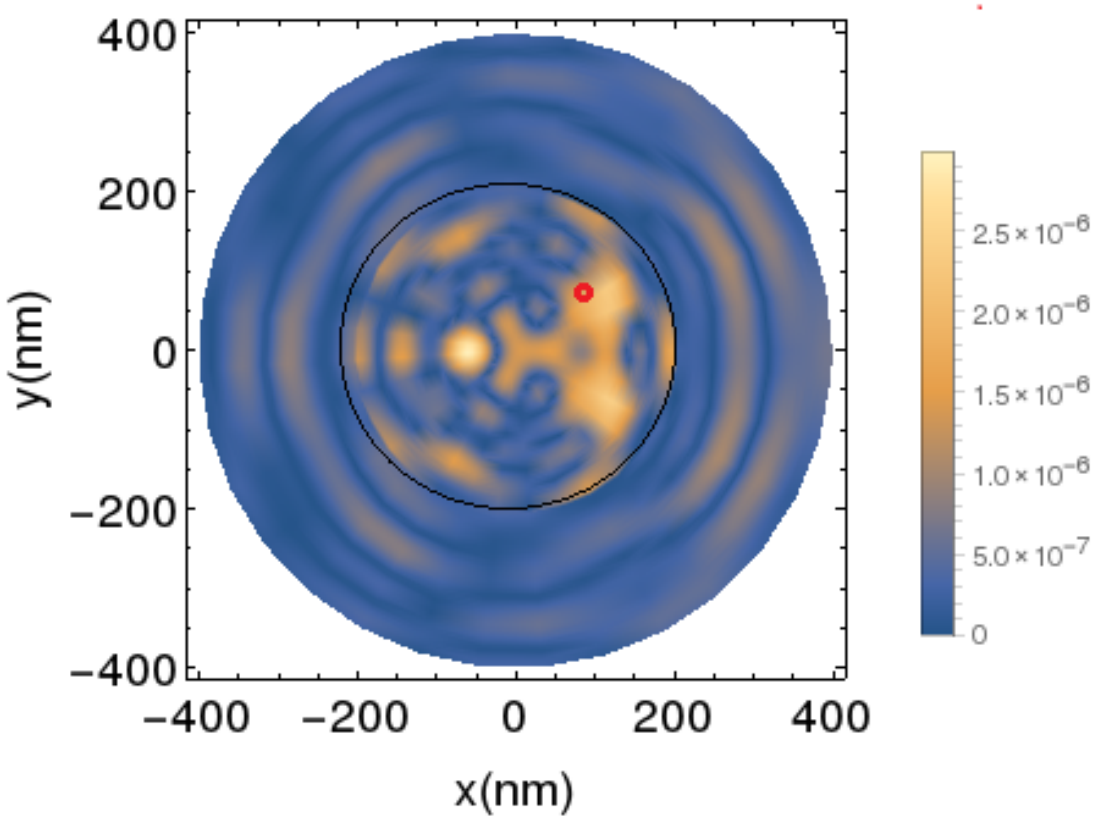

Figure 4.11: Density plot of the plasmon wavefunction in the presence of a z-oriented dipole placed at the $r = (100, 100, 30)$nm with the frequency of $\omega = 1700$. The red dot at the center shows the position of the external dipole, and the dashed circle indicate the position of the disk.

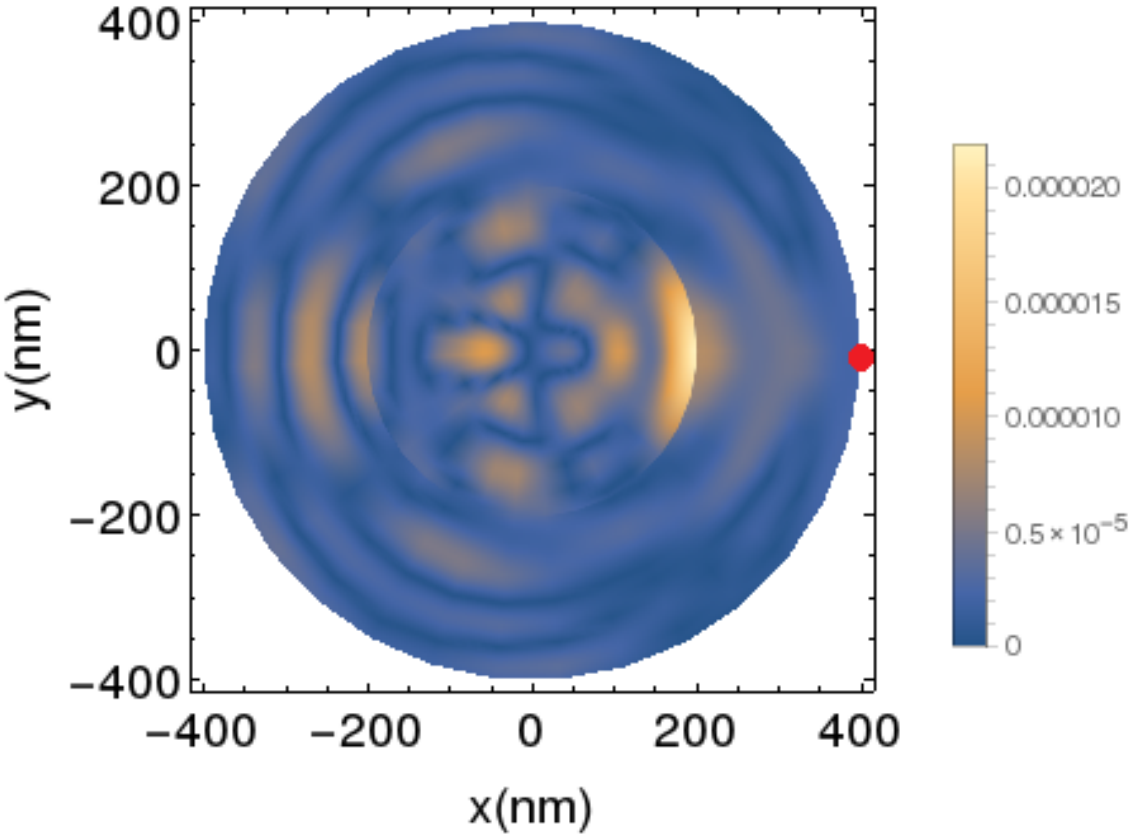

Figure 4.12: Density plot of the plasmon wavefunction in the presence of a z-oriented dipole placed at the $r = (100, 100, 30)$nm with the frequency of $\omega = 1323$. The red dot at the center shows the position of the external dipole and the dashed circle indicate the position of the disk.

Appendix A

Electron Self-Energy due to Optical Phonon in Graphene

The electron-phonon interaction can induce many body effect and hot electron relaxiation in graphene. The electron self-energy due to the electron-phonon interaction in graphene at a temperature T is [72],

$$\Sigma(\mathbf{k}, i\omega_n) = -k_B T \sum_{ss'\mathbf{q}} i\omega_m |\langle \mathbf{k}+\mathbf{q}, s'|g_{\mathbf{q}}|\mathbf{k}, s\rangle|^2 D(q, i\omega_m) G(\mathbf{k}+\mathbf{q}, i\omega_m + i\omega_n) \quad \text{(A.1)}$$

Here $\omega_m = 2\pi m k_B T$ is the Matsubara frequency with the integer m, $\langle \mathbf{k}+\mathbf{q}, s'|g_{\mathbf{q}}|\mathbf{k}, s\rangle$ is electron-optical phonon coupling matrix element.$|\mathbf{k}, s\rangle$, $|\mathbf{k}+\mathbf{q}, s'\rangle$ indicate Bloch eigenstates. $D(\mathbf{q}, i\omega_m)$ and $G(\mathbf{k}+\mathbf{q}, i\omega_m + i\omega_n)$ indicate phonon and electron Green Function, respectively, that can be expressed as:

$$D(\mathbf{q}, i\omega_m) = \frac{2\omega_{\mathbf{q}}}{(i\omega_m)^2 - \omega_{\mathbf{q}}^2} \quad \text{(A.2)}$$

$$G(\mathbf{k}+\mathbf{q}, i\omega_m + i\omega_n) = \frac{1}{i\omega_m + i\omega_n - E_{\mathbf{k}+\mathbf{q},s}} \quad \text{(A.3)}$$

where $\omega_{\mathbf{q}}$ stands for energy of optical phonon with wavevector $\mathbf{q}$ and $E_{\mathbf{k}+\mathbf{q},s}$ is an energy of electronic state with band indix s and wavevector $\mathbf{k}+\mathbf{q}$.

The sum can be taken over boson frequency, then $\Sigma_{i\omega_m}$ is calculated by a contour

integral. We then define a function

$$f(z) = D(\mathbf{q}, z)G(\mathbf{k}+\mathbf{q}, z+i\omega_n)n(z) \tag{A.4}$$

$n(z)$ is boson distribution function.

$$n(z) = \frac{1}{e^{\beta\hbar z}-1} \tag{A.5}$$

When $z \to i\omega_m$, we get

$$\lim_{z\to i\omega_m} f(z) = \frac{1}{\beta}D(\mathbf{q}, i\omega_m)G(\mathbf{k}+\mathbf{q}, i\omega_m+i\omega_n) \tag{A.6}$$

According to the method of Residues, sum over all residues is zero,

$$\mathrm{Res}(z\to i\omega_n)+\mathrm{Res}(z\to\omega_\mathbf{q})+\mathrm{Res}(z\to-\omega_\mathbf{q})+\mathrm{Res}(z\to i\omega_m+E_{\mathbf{k}+\mathbf{q}})=0 \tag{A.7}$$

here

$$\begin{aligned}
\mathrm{Res}(z\to\omega_\mathbf{q}) &= \frac{n(\omega_\mathbf{q})}{i\omega_n+\omega_\mathbf{q}-E_{\mathbf{k}+\mathbf{q}}} && \text{(A.8)}\\
\mathrm{Res}(z\to-\omega_\mathbf{q}) &= -\frac{n(-\omega_\mathbf{q})}{i\omega_n-\omega_\mathbf{q}-E_{\mathbf{k}+\mathbf{q}}} && \text{(A.9)}\\
\mathrm{Res}(z\to-i\omega_n+E_{\mathbf{k}+\mathbf{q}}) &= \frac{2\omega_\mathbf{q}n(-i\omega_n+E_{\mathbf{k}+\mathbf{q}})}{(i\omega_n-E_{\mathbf{k}+\mathbf{q}})^2-\omega_q^2} && \text{(A.10)}
\end{aligned}$$

substituting into Eq.A.6, we get

$$\begin{aligned}
&\frac{1}{\beta}D(\mathbf{q}, i\omega_m)G(\mathbf{k}+\mathbf{q}, i\omega_m+i\omega_n)\\
= &-\frac{n(\omega_\mathbf{q})}{i\omega_n+\omega_q-E_{\mathbf{k}+\mathbf{q}}}+\frac{n(-\omega_\mathbf{q})}{i\omega_n-\omega_q-E_{\mathbf{k}+\mathbf{q}}}-\frac{2\omega_\mathbf{q}n(-i\omega_n+E_{\mathbf{k}+\mathbf{q}})}{(i\omega_n-E_{\mathbf{k}+\mathbf{q}})^2-\omega_\mathbf{q}^2} \qquad \text{(A.11)}
\end{aligned}$$

and

$$\begin{aligned}
\frac{2\omega_\mathbf{q}}{(i\omega_n-E_{\mathbf{k}+\mathbf{q}})^2-\omega_\mathbf{q}^2} &= \frac{1}{i\omega_m-\omega_\mathbf{q}-E_{\mathbf{k}+\mathbf{q}}}-\frac{1}{i\omega_m+\omega_\mathbf{q}-E_{\mathbf{k}+\mathbf{q}}} && \text{(A.12)}\\
n(-\omega_\mathbf{q}) &= -(1+n(\omega_\mathbf{q})) && \text{(A.13)}\\
n(-i\omega_n+E_{\mathbf{k}+\mathbf{q}}) &= -f(E_{\mathbf{k}+\mathbf{q}}) && \text{(A.14)}
\end{aligned}$$

Then electron self energy due to interaction with optical phonon in graphene has the form:

$$\begin{aligned}
& \Sigma(k,\omega)^{ph} \\
= & \sum_{\mathbf{q},ss'} |<\mathbf{k}+\mathbf{q},s'|g_{\mathbf{q}}|\mathbf{k},s>|^2 \left[\frac{n(\omega_{\mathbf{q}})+1-f_{\mathbf{k+q}}}{\omega-E_{\mathbf{k+q}}-\omega_{\mathbf{q}}+i\delta}+\frac{n(\omega_{\mathbf{q}})+f_{\mathbf{k+q}}}{\omega-E_{\mathbf{k+q}}+\omega_{\mathbf{q}}+i\delta}\right] \\
= & \frac{g_0^2}{2}\sum_{\mathbf{q},ss'}(1\mp ss'\cos(\theta_{\mathbf{k+q}}+\theta_{\mathbf{k}}-2\theta_{\mathbf{q}}) \\
\times & \left[\frac{n(\omega_{\mathbf{q}})+1-f_{\mathbf{k+q}}}{\omega-E_{\mathbf{k+q}}-\omega_{\mathbf{q}}+i\delta}+\frac{n(\omega_{\mathbf{q}})+f_{\mathbf{k+q}}}{\omega-E_{\mathbf{k+q}}+\omega_{\mathbf{q}}+i\delta}\right] \\
= & \frac{g_0^2}{2}\int_0^{2\pi} d\theta_{\mathbf{kq}}\int qdq(1\mp ss'\cos(\theta_{\mathbf{q+k,q}}+\theta_{\mathbf{kq}})) \\
\times & \left[\frac{n(\omega_{\mathbf{q}})+1-f_{\mathbf{k+q}}}{\omega-E_{\mathbf{k+q}}-\omega_{\mathbf{q}}+i\delta}+\frac{n(\omega_{\mathbf{q}})+f_{\mathbf{k+q}}}{\omega-E_{\mathbf{k+q}}+\omega_{\mathbf{q}}+i\delta}\right]
\end{aligned} \tag{A.15}$$

where $\omega_q \approx 0.2eV$ is the graphene longitudinal/transverse optical phonons near Γ point. $n(\omega)$ ($f(\omega)$) is thermal distribution function of optical phonons (electrons) in graphene. $g_q = 0.0405eV^2$ [72] is electron-phonon interaction constant. $\cos(\theta_{\mathbf{q+k,q}}+\theta_{\mathbf{kq}}) = \cos(\theta_{\mathbf{k+q}}+\theta_{\mathbf{k}}-2\theta_{\mathbf{q}})$, $\theta_{\mathbf{qk}}$ is the minimal angle between two vectors $\mathbf{k}$,$\mathbf{q}$. Since $\theta_{\mathbf{q+k,q}} \approx 2\theta_{\mathbf{kq}} - \pi$ for small $\mathbf{k}$, and

$$\int \frac{d^2q}{(2\pi)^2}\delta(E-E_q) = \frac{|E|}{2\pi(\hbar v_f)^2}, \tag{A.16}$$

the imaginary part of $\Sigma(k,\omega)^{ph}$ can be expressed as

$$\begin{aligned}
& \mathrm{Im}[\Sigma(k,\omega)^{ph}] \\
= & \frac{g_0^2}{2}\int qdq \\
\times & \delta(\omega-\omega_0-E_{\mathbf{k+q}})\left[\frac{n(\omega_0)+1-f_{\mathbf{k+q}}}{\omega-E_{\mathbf{k+q}}-\omega_0+i\delta}\right] \\
+ & \delta(\omega+\omega_0-E_{\mathbf{k+q}})\left[\frac{n(\omega_{\mathbf{q}})+f_{\mathbf{k+q}}}{\omega-E_{\mathbf{k+q}}+\omega_{\mathbf{q}}+i\delta}\right] \\
= & \frac{g_0^2}{2}\left(\frac{|\omega-\omega_0|}{2\pi(\hbar v_f)^2}(n(\omega_0)-f(E_{\mathbf{k+q}}))+\frac{|\omega+\omega_0|}{2\pi(\hbar v_f)^2}(n(\omega_0)+f(E_{\mathbf{k+q}}))\right)
\end{aligned} \tag{A.17}$$

The real part of the electron self-energy can be obtained using the Kramer-Kronig relations,

$$\mathrm{Re}[\Sigma(k,\omega)^{ph}] = \frac{1}{\pi}\mathbf{P}\int_{-\infty}^{\infty}\frac{\mathrm{Im}[\Sigma(k,\omega')^{ph}]}{\omega'-\omega}d\omega' \tag{A.18}$$

The real part is related to the frequency shift of the electron due to scattering with optical phonons. The imaginary part tells about electron life time via

$$\tau = \hbar/2\mathrm{Im}[\Sigma(k,\omega)^{ph}]. \tag{A.19}$$

Bibliography

[1] Leilei Kang, Jiayu Chu, Hongtao Zhao, Ping Xu, and Mengtao Sun. Recent progress in the applications of graphene in surface-enhanced raman scattering and plasmon-induced catalytic reactions. *J. Mater. Chem. C*, 3:9024–9037, 2015.

[2] Jürgen Schiefele, Fernando Sols, and Francisco Guinea. Temperature dependence of the conductivity of graphene on boron nitride. *Phys. Rev. B*, 85:195420, May 2012.

[3] A. H. Castro Neto, F. Guinea, N. M. R. Peres, K. S. Novoselov, and A. K. Geim. The electronic properties of graphene. *Rev. Mod. Phys.*, 81:109–162, Jan 2009.

[4] Jia-An Yan, W. Y. Ruan, and M. Y. Chou. Phonon dispersions and vibrational properties of monolayer, bilayer, and trilayer graphene: Density-functional perturbation theory. *Phys. Rev. B*, 77:125401, Mar 2008.

[5] Eric Pop, Vikas Varshney, and Ajit K. Roy. Thermal properties of graphene: Fundamentals and applications. *MRS Bulletin*, 37:1273, 2012.

[6] A.A. Balandin. Thermal properties of graphene and nanostructured carbon materials. *Nature Materials*, 10:569, 2011.

[7] Yee Kan Koh, Myung-Ho Bae, David G. Cahill, and Eric Pop. Heat conduction across monolayer and few-layer graphenes. *Nano Letters*, 10:4346, 2010.

[8] Meryl D. Stoller, Sungjin Park, Yanwu Zhu, Jinho An, and Rodney S. Ruoff. Graphene-based ultracapacitors. *Nano Letters*, 8(10):3498–3502, 2008. PMID: 18788793.

[9] Phaedon Avouris. Graphene: Electronic and photonic properties and devices. *Nano Letters*, 10(11):4285–4294, 2010. PMID: 20879723.

[10] F. Bonaccorso, Z. Sun, T. Hasan, and A. C. Ferrari. Graphene photonics and optoelectronics. *Nature Photon*, 4:611, 2010.

[11] Seyoung Kim, Junghyo Nah, Insun Jo, Davood Shahrjerdi, Luigi Colombo, Zhen Yao, Emanuel Tutuc, and Sanjay K. Banerjee. Realization of a high mobility dual-gated graphene field-effect transistor with al2o3 dielectric. *Applied Physics Letters*, 94(6), 2009.

[12] Yu-Hsien Wu, Po-Yuan Tseng, Ping-Yen Hsieh, Hung-Tao Chou, and Nyan-Hwa Tai. High mobility of graphene-based flexible transparent field effect transistors doped with tio2 and nitrogen-doped tio2. *ACS Applied Materials & Interfaces*, 7(18):9453–9461, 2015. PMID: 25905566.

[13] Marinko Jablan, Hrvoje Buljan, and Marin Soljačić. Plasmonics in graphene at infrared frequencies. *Phys. Rev. B*, 80:245435, Dec 2009.

[14] Long Ju, Baisong Geng, Jason Horng, Caglar Girit, Michael Martin, Zhao Hao, Hans A. Bechtel, Xiaogan Liang, Alex Zettl, Y. Ron Shen, and Feng Wang. Graphene plasmonics for tunable terahertz metamaterials. *Nature Nanotechnology*, 6:630, 2009.

[15] S. Das Sarma, Shaffique Adam, E. H. Hwang, and Enrico Rossi. Electronic transport in two-dimensional graphene. *Rev. Mod. Phys.*, 83:407–470, May 2011.

[16] K. S. Novoselov, A. K. Geim, S. V. Morozov, D. Jiang, M. I. Katsnelson, I. V. Grigorieva, S. V. Dubonos, and A. A. Firsov. Two-dimensional gas of massless dirac fermions in graphene. *Nature*, 438:197–200, May 2005.

[17] L. A. Falkovsky and S. S. Pershoguba. Optical far-infrared properties of a graphene monolayer and multilayer. *Phys. Rev. B*, 76:153410, Oct 2007.

[18] F. Javier Garca de Abajo. Graphene plasmonics: Challenges and opportunities. *ACS Photonics*, 1(3):135–152, 2014.

[19] Chen Shi Fan. Controlling inelastic light scattering quantum pathways in graphene. *Nature*, 471:617, 2001.

[20] Johan Christensen and F. Javier García de Abajo. Anisotropic metamaterials for full control of acoustic waves. *Phys. Rev. Lett.*, 108:124301, Mar 2012.

[21] Bin Shi, Wei Cai, Xinzheng Zhang, Yinxiao Xiang, Yu Zhan, Juan Geng, and Mengxin Ren. Tunable band-stop filters for graphene plasmons based on periodically modulated graphene. *ACS Photonics*, 6:26796, 2016.

[22] Mohammad M. Jadidi, Andrei B. Sushkov, Rachael L. Myers-Ward, Anthony K. Boyd, Kevin M. Daniels, D. Kurt Gaskill, Michael S. Fuhrer, H. Dennis Drew, and Thomas E. Murphy. Tunable terahertz hybrid metalgraphene plasmons. *Nano Letters*, 15(10):7099–7104, 2015. PMID: 26397718.

[23] F. Guinea, A. H. Castro Neto, and N. M. R. Peres. Electronic states and landau levels in graphene stacks. *Phys. Rev. B*, 73:245426, Jun 2006.

[24] J. M. B. Lopes dos Santos, N. M. R. Peres, and A. H. Castro Neto. Graphene bilayer with a twist: Electronic structure. *Phys. Rev. Lett.*, 99:256802, Dec 2007.

[25] *Graphene Heterostructures with Hexagonal Crystals.* Springer Thesis, 2010.

[26] D. L. Nika, E. P. Pokatilov, A. S. Askerov, and A. A. Balandin. Phonon thermal conduction in graphene: Role of umklapp and edge roughness scattering. *Phys. Rev. B*, 79:155413, Apr 2009.

[27] Serap Yigen. *Electronic Thermal Condctivity Measurements in Graphene.* PhD thesis, Concordia University, 2015.

[28] S. Ghosh, I. Calizo, D. Teweldebrhan, E. P. Pokatilov, D. L. Nika, A. A. Balandin, W. Bao, F. Miao, and C. N. Lau. Extremely high thermal conductivity of graphene: Prospects for thermal management applications in nanoelectronic circuits. *Applied Physics Letters*, 92(15), 2008.

[29] Alxander L. Fetter and John Dirk Walecka. *Quantum Theory of Many Particle Systems*.

[30] Ahsan Nazir. *Lecture notes on open quantum systems*.

[31] I. Calizo, A. A. Balandin, W. Bao, F. Miao, and C. N. Lau. Temperature dependence of the raman spectra of graphene and graphene multilayers. *Nano Letters*, 7(9):2645, 2007.

[32] Clement Faugeras, Blaise Faugeras, Milan Orlita, M. Potemski, Rahul R. Nair, and A. K. Geim. Thermal conductivity of graphene in corbino membrane geometry. *ACS Nano*, 4:1889, 2010.

[33] S.S. Chen and el at. Raman measurements of thermal transport in suspended monolayer graphene of variable sizes in vacuum and gaseous environments. *Acs Nano*, 5:321, 2011.

[34] Zhun-Yong Ong and Eric Pop. Effect of substrate modes on thermal transport in supported graphene. *Phys. Rev. B*, 84:075471, Aug 2011.

[35] Zhiyong Wei, Zhonghua Ni, Kedong Bi, Minhua Chen, and Yunfei Chen. In-plane lattice thermal conductivities of multilayer graphene films. *Carbon*, 49(8):2653 – 2658, 2011.

[36] Ying Liu, Chongze Hu, Jingsong Huang, Bobby G. Sumpter, and Rui Qiao. Tuning interfacial thermal conductance of graphene embedded in soft materials by vacancy defects. *The Journal of Chemical Physics*, 142(24), 2015.

[37] Bo Peng, Hao Zhang, Hezhu Shao, Yuchen Xu, and Xiangchao Zhang. Low lattice thermal conductivity of stanene. *Scientific Reports*, page 20225, 2016.

[38] Alexander A. Balandin, Suchismita Ghosh, Wenzhong Bao, Irene Calizo, Desalegne Teweldebrhan, Feng Miao, and Chun Ning Lau. Superior thermal conductivity of single-layer graphene. *Nano Letters*, 8:902, 2008.

[39] Weiwei Cai, Arden L. Moore, Yanwu Zhu, Xuesong Li, Shanshan Chen, Li Shi, and Rodney S. Ruoff. Thermal transport in suspended and supported monolayer graphene grown by chemical vapor deposition. *Nano Letters*, 10(5):1645–1651, 2010. PMID: 20405895.

[40] Manuel E. Pumarol, Mark C. Rosamond, Peter Tovee, Michael C. Petty, Dagou A. Zeze, Vladimir Falko, and Oleg V. Kolosov. Direct nanoscale imaging of ballistic and diffusive thermal transport in graphene nanostructures. *Nano Letters*, 12(6):2906–2911, 2012. PMID: 22524441.

[41] Suchismita Ghosh, Wenzhong Bao, Denis L. Nika, Samia Subrina, Evghenii P. Pokatilov, Chun Ning Lau, and Alexander A. Balandin. Dimensional crossover of thermal transport in few-layer graphene. *Nature Materials*, 9:555, 2010.

[42] Jae Hun Seol, Insun Jo, Arden L. Moore, Lucas Lindsay, Zachary H. Aitken, Michael T. Pettes, Xuesong Li, Zhen Yao, Rui Huang, David Broido, Natalio Mingo, Rodney S. Ruoff, and Li Shi. Two-dimensional phonon transport in supported graphene. *Science*, 328(5975):213–216, 2010.

[43] E. T. Swartz and R. O. Pohl. Thermal boundary resistance. *Rev. Mod. Phys.*, 61:605–668, Jul 1989.

[44] Zhe Fei, Gregory O. Andreev, Wenzhong Bao, Lingfeng M. Zhang, Alexander S. McLeod, Chen Wang, Margaret K. Stewart, Zeng Zhao, Gerardo Dominguez, Mark Thiemens, Michael M. Fogler, Michael J. Tauber, Antonio H. Castro-Neto, Chun Ning Lau, Fritz Keilmann, and Dimitri N. Basov. Infrared nanoscopy of dirac plasmons at the graphene/sio2 interface. *Nano Letters*, 11:4701, 2011.

[45] A. N. et al. Grigorenko. Graphene plasmonics. *Nature Photonics*, 6:479, 2012.

[46] Hugen Yan, Tony Low, Wenjuan Zhu, Yanqing Wu, Marcus Freitag, Xuesong Li, Francisco Guinea andPhaedon Avouris, and Fengnian Xia. Damping pathways of mid-infrared plasmons in graphene nanostructures. *Nature Photonics*, 7:394, 2013.

[47] A. Vakil and N. Engheta. Transformation optics using graphene. *Science*, 332:1291, 2011.

[48] Rashid Zia, Jon A. Schuller, Anu Chandran, and Mark L. Brongersma. Plasmonics: the next chip-scale technology. *Materials Today*, 9(78):20 – 27, 2006.

[49] Hyun Chul Kim and Xing Cheng. Surface phonon polaritons on sic substrate for surface-enhanced infrared absorption spectroscopy. *J. Opt. Soc. Am. B*, 27(11):2393–2397, Nov 2010.

[50] Hyun Chul Kim and Xing Cheng. Surface phonon polaritons on sic substrate for surface-enhanced infrared absorption spectroscopy. *J. Opt. Soc. Am. B*, 27(11):2393–2397, Nov 2010.

[51] Peter B. Catrysse and Shanhui Fan. Near-complete transmission through subwavelength hole arrays in phonon-polaritonic thin films. *Phys. Rev. B*, 75:075422, Feb 2007.

[52] J Nkoma, R Loudon, and D R Tilley. Elementary properties of surface polaritons. *Journal of Physics C: Solid State Physics*, 7(19):3547, 1974.

[53] Andrew K. Hafeli, Eden Rephaeli, Shanhui Fan, David G. Cahill, and Thomas E. Tiwald. Temperature dependence of surface phonon polaritons from a quartz grating. *Journal of Applied Physics*, 110(4), 2011.

[54] Jiyang Fan and Chu. Paul K. *General Properties of Bulk SiC*. 2014.

[55] S. Q. Wang and G. D. Mahan. Electron scattering from surface excitations. *Phys. Rev. B*, 6:4517–4524, Dec 1972.

[56] H.P. Breuer and F. Petruccione. *The theory of open quantum system*. Oxford, 2002.

[57] H J Carmichael and D F Walls. Master equation for strongly interacting systems. *Journal of Physics A: Mathematical, Nuclear and General*, 6(10):1552, 1973.

[58] Haifeng Yin and Hong Zhang. Plasmons in graphene nanostructures. *Journal of Applied Physics*, 111(10), 2012.

[59] Weihua Wang, Peter Apell, and Jari Kinaret. Edge plasmons in graphene nanostructures. *Phys. Rev. B*, 84:085423, Aug 2011.

[60] E. G. Mishchenko, A. V. Shytov, and P. G. Silvestrov. Guided plasmons in graphene *p-n* junctions. *Phys. Rev. Lett.*, 104:156806, Apr 2010.

[61] Achim Woessner and et al. Highly confined low-loss plasmons in grapheneboron nitride heterostructures. *Nature Materials*, 14:421, 2015.

[62] V.W. Brar and et al. Hybrid surface-phonon-plasmon polariton modes in graphene/monolayer h-bn heterostructures. *Nano Letters*, 14:3876, 2014.

[63] Alexander L. Fetter. Magnetoplasmons in a two-dimensional electron fluid: Disk geometry. *Phys. Rev. B*, 33:5221–5227, 1986.

[64] Anshuman Kumar, Kin Hung Fung, M. T. Homer Reid, and Nicholas X. Fang. Photon emission rate engineering using graphene nanodisc cavities. *Opt. Express*, 22(6):6400–6415, 2014.

[65] Weihua Wang, Peter Apell, and Jari Kinaret. Edge plasmons in graphene nanostructures. *Phys. Rev. B*, 84:085423, Aug 2011.

[66] Weihua Wang, S. Peter Apell, and Jari M. Kinaret. Edge magnetoplasmons and the optical excitations in graphene disks. *Phys. Rev. B*, 86:125450, Sep 2012.

[67] Joel I. Gersten. Disk plasma oscillations. *The Journal of Chemical Physics*, 77(12):6285–6288, 1982.

[68] Arfken Weber. *Mathematical Methods for Physicists*. Elsevier Academic Press, 2005.

[69] J.D. Jackson. *Classical Eletrodynamics*. John Wiley Sons, 1999.

[70] Tobias Stauber. Plasmonics in dirac systems: from graphene to topological insulators. *Journal of Physics: Condensed Matter*, 26(12):123201, 2014.

[71] G. T. de Laissardire, D. Mayou, and L. Magaud. Localization of dirac electrons in rotated graphene bilayers. *Nano Letters*, 10:804, Nov 2010.

[72] Matteo Calandra and Francesco Mauri. Electron-phonon coupling and electron self-energy in electron-doped graphene: Calculation of angular-resolved photoemission spectra. *Phys. Rev. B*, 76:205411, Nov 2007.

Vita

Dan You received her Bachelor's degree in Physics at Nanjing Normal University in June 2007 , and received her Master's Degree in Physics at Nanjing University in June 2010. She enrolled in the Ph.D. program in the Physics Department at Lehigh University in 2011. She worked as a Teaching assistant in Introductory of Physics from August 2011 to May 2013. She began her Ph.D. research on Graphene plasmonics supervised by Professor Slava V. Rotkin since 2011 and earned a Ph.D. in Physics in May 2017.